ABSTRACT

Title of Document:	TRIBOLOGY OF MICROBALL BEARING MEMS
	Brendan Michael Hanrahan, Doctor of Philosophy, 2013
Directed By:	Professor Reza Ghodssi, Department of Electrical and Computer Engineering, Institute for Systems Research

This dissertation explores the fundamental tribology of microfabricated rolling bearings for future micro-machines. It is hypothesized that adhesion, rather than elastic hysteresis, dominates the rolling friction and wear for these systems, a feature that is unique to the micro-scale. To test this hypothesis, specific studies in contact area and surface energy have been performed. Silicon microturbines supported on thrust bearings packed with 285 µm and 500 µm diameter stainless steel balls have undergone spin-down friction testing over a load and speed range of 10-100mN and 500-10,000 rpm, respectively. A positive correlation between calculated contact area and measured friction torque was observed, supporting the adhesion-dominated hysteresis hypothesis. Vapor phase lubrication has been integrated within the microturbine testing scheme in a controlled and characterized manner. Vapor-phase molecules allowed for specifically addressing adhesive energy without changing other system properties. A 61% reduction of friction torque was observed with the utilization of 18% relative humidity water vapor lubrication. Additionally, the relationship between friction torque and normal load was shown to follow an adhesion-based trend,

highlighting the effect of adhesion and further confirming the adhesion-dominant hypothesis. The wear mechanisms have been studied for a microfabricated ball bearing platform that includes silicon and thin-film coated silicon raceway/steel ball materials systems. Adhesion of ball material, found to be the primary wear mechanism, is universally present in all tested materials systems. Volumetric adhesive wear rates are observed between 4×10^{-4} μm^3/mN•rev and 4×10^{-5} μm^3/mN•rev were determined by surface mapping techniques and suggest a self-limiting process. This work also demonstrates the utilization of an Off-The-Shelf (OTS) MEMS accelerometer to confirm a hypothesized ball bearing instability regime which encouraged the design of new bearing geometries, as well as to perform in situ diagnostics of a high-performance rotary MEMS device. Finally, the development of a 3D fabrication technique with the potential of significantly improving the performance of micro-scale rotary structures is described. The process was used to create uniform, smooth, curved surfaces. Micro-scale ball bearings are then able to be utilized in high-speed regimes where load can be accommodated both axially and radially, allowing for new, high-speed applications. A comprehensive exploration of the fundamental tribology of microball bearing MEMS has been performed, including specific experiments on friction, wear, lubrication, dynamics, and geometrical optimization. Future devices utilizing microball bearings will be engineered and optimized based on the results of this dissertation.

TRIBOLOGY OF MICROBALL BEARING MEMS

By

Brendan Michael Hanrahan

Dissertation submitted to the Faculty of the Graduate School of the

University of Maryland, College Park, in partial fulfillment

of the requirements for the degree of

Doctor of Philosophy

2013

Advisory Committee:
Professor Reza Ghodssi, Chair
Professor Ichiro Takeuchi
Professor Christopher Cadou
Professor Robert Briber
Professor Isabel Lloyd

Dedication

To my grandparents, Judy and Joe Hanrahan.
They were there for my first day of school.

Acknowledgements

First and foremost, I would like to acknowledge my academic advisor, Professor Reza Ghodssi. The road to completing this dissertation was not without speed-bumps, but in retrospect each bump was an important lesson, and I have ended up a better researcher and person because of it.

Dr. Mike Waits is the principal reason I had the opportunity to perform this work. His belief in me opened the door for the support at the Army Research Lab. As a mentor he was thorough, trusting, and patient. He progressed the microball bearing technology further than anyone previous and I only hope he sees this dissertation as progressing the science.

I had the opportunity to mentor a few students in my tenure as a Ph.D. student and I would like to acknowledge two in particular: Jeremy Feldman and Saswat Misra. Jeremy programmed much of the experimental control software for the work presented herein. I could not have finished with the quality of experiments I had without Jeremy's help. Saswat Misra began as my right-hand man with the vapor-phase lubrication experiments and became an expert in the field. He will go on to be successful wherever he lands.

I would like to thank Dr. Konstantinos Gerasapolous, and Dr. Mustafa Beyaz for the constructive criticism over the years. Mustafa and I worked on ball bearing projects and I think he is the person most familiar with this work. Mustafa, Kostas, and I all learned how to write, how to make a graph, and how to do research from my first mentor, Dr. Matt McCarthy.

Finally, I would like to acknowledge every member of the MEMS Sensors and Actuators Laboratory, past and present. Everyone participates in constructive discussions and all of our science is better because of it.

Table of Contents

List of Figures

List of Tables

1. Introduction

1.1 Motivation

Micro-ElectroMechanical Systems (MEMS) utilize semiconductor fabrication technologies to integrate mechanical components with electronics on a single chip. MEMS technology has progressed since the early 1980s from very simple mechanical systems with elementary electronics to fully integrated sensor platforms employed in car airbags and Nintendo Wii™ controllers. This work is focused on MEMS technology in the power and energy domain, specifically, but not exclusively, applicable to MEMS with rotating components. Contact bearings have been extensively studied on the macro-scale and are now common-place for all machinery that undergoes reciprocating motion. Bearing mechanisms on the micro-scale for reciprocating or rotary motion are not as well understood. *This dissertation studied the sources of micro-scale rolling friction within microfabricated thrust bearings. Specifically, the relationship between normal load, contact area, and the adhesive component of rolling friction and wear was addressed through experiments in scaling the bearing contact, vapor-phase lubrication, and alternative microfabricated bearing geometries.*

Rotary micromachines, the subject of this study, are attractive for power and energy applications, such as micropumps [1] and micromotors [2-4]. Accordingly, the microball bearing was adopted previously within a rotor/stator mechanism in the demonstration of an electrostatically actuated micromotor [4]. In [4], a rotor with rectangular groove trenches is placed atop spaced microballs within a stator trench, giving a constant, mechanically stable gap for capacitive actuation while providing low friction. Waits, *et al.,* pioneered the encapsulation of microball bearings to support an integrated rotary device [5]. It was found during testing of the encapsulated bearings that the stress concentrations from point contact

lead to significant bearing wear and an inability to maintain dimensional tolerances. Subsequent bearing designs altered the bearing to include completely planar contacts [6].

A majority of tribology studies within microfabricated systems are focused on sliding-regime, micro- and continuum length scales, with little focus on the unique realm of micro-scale *rolling* friction. Early MEMS tribology efforts focused on the effect of environment on the coefficient of friction [7]. Corwin *et al.* measured friction in zero-normal load conditions, attributing measured friction to adhesion and following the proportionality between friction and normal load established by Amonton's Law. Several studies utilized atomic force microscopy or friction force microscopy to characterize system level friction [8, 9]. In [8], Tambe *et al.* establishes a relationship between sliding friction force and velocity for micromachined silicon and coated surfaces. They show a reduction of friction force at greater velocities for silicon surfaces, and conclude that the reduced friction arises from a reduction in meniscus formation time. Other groups choose to micromachine structures specific to friction characterization [10-12]. The wobble micromotor fabricated in [13] utilizes a contact bearing with a bushing design that was operated over 100 million revolutions and measured a 20% change in the ratio of bearing radius to bearing clearance due to wear of the planar contacts.

Liquid phase lubrication does not have wide-spread use in the MEMS realm. Capillary forces created by confining liquids to small geometries can be on the same order of magnitude as actuation forces generated by micromachines, therefore solid or vapor-phase lubrication is typically used. Vapor-phase lubrication is achieved by saturating a surface with a molecule, typically with high vapor pressure. The organic molecule adsorbs on surfaces and assembles either chemically or physically, reducing the surface energy of the mating surfaces, therefore reducing the adhesion. This study will utilize vapor-phase lubrication to specifically target the adhesive component of micro-scale rolling friction. Different

molecular weight alcohol vapors will be employed to operate the air-turbine, simultaneously lubricating the bearing. The results help illuminate the contribution of adhesion to micro-scale rolling friction, increasing the understanding of micro-scale tribology.

Microfabrication technology, such as Deep Reactive Ion Etching (DRIE), is ideal for layered structures with rectangular cross sections. This process has been employed to fabricate the microball bearing systems demonstrated to-date where balls are held within flat-walled bearings. This configuration provides no support for the side-to-side motion of the ball during operation while also concentrating the contact pressure beneath the ball because of the non-conformality of the sphere contacting a plane. Experimental fabrication techniques will be employed within this work to make a bearing housing that more closely mimics the bearings seen on the macro-scale. This optimized bearing will be tested within a microturbine and performance will be evaluated.

1.2   Dissertation Contributions

Hypothesis: *Rolling friction in microfabricated systems is dominated by adhesion, rather than hysteresis as is the case with macro-scale rolling friction, therefore fundamental relationships between observed friction and normal load should differ significantly from widely accepted macro-scale relationships.*

To test this hypothesis,

1. I developed experiments specifically designed to address the influence of contact area by testing four microturbine variations. I found that friction scaled with contact area, e.g., the lowest contact area system had the lowest friction torque. This is opposite from what one would expect in macro-scale ball bearings, where the largest contact area would result in the lowest friction due to it having the lowest contact pressure.

2. I implemented a vapor-phase lubrication system to lower the adhesive energy of the system while keeping other properties static. I showed that devices operated with lubrication had lower adhesive energy, resulting in significantly lower friction and helping to confirm the adhesion hypothesis. Combined with the contact area experiments, this study provides a framework for reducing friction in future microball bearing systems.

3. I performed a set of accelerated wear experiments for a range of materials systems. These experiments determine the ideal operating regimes and materials for long-lived, high performance microball bearing systems.

4. I engineered new microfabricated bearing geometries and demonstrate operation to high speeds. This included a parametric study to optimize a new etching process with high uniformity and tight geometric tolerances. The engineered bearing geometry allows for never-before obtainable microball bearing geometries.

5. I implemented a vibration-based diagnostic technique for rotary MEMS. This tool was shown to repeatedly predict bearing instability, wobble, imbalances, and resonance for a microball bearing system. This system works for any rotary MEMS device and has applications in diagnostics and reliability.

1.3   Literature Review

1.3.1   Micro-scale bearings

Micro-scale bearings have been employed since the first MEMS devices had completely released, free moving structures. All bearings can be classified as contact or non-contact. Within the realm of solid contact bearings, one can have sliding (plain) bearings, or

rolling contact bearings. Non-contact bearings include methods of levitation either via gas, a balance of electric/magnetic fields, or the utilization of liquid interfaces. Table 1-1 below presents a qualitative comparison of each bearing type.

Table 1-1 Comparison of micro-scale bearings

property/bearing	Sliding	Liquid	Levitation	Rolling
Speed	low	low	very high (>1 Mrpm)	high (>50 krpm)
Friction and wear	poor	low wear/ high friction	very good	good
Stability	good	good	difficult	good
Fabrication	simple	moderate	complicated	moderate
Failure	gradual	gradual	catastrophic	gradual

Each bearing has certain benefits, which is why all bearing variations are employed in various macro-scale machines. This section will cover sliding, liquid, and levitated micro-scale bearings. Rolling contacts utilized on the micro-scale will be discussed in detail in the following section.

Sliding bearings were first examined in the MEMS realm for a variable capacitance micromotor by Mehregany *et al*. [14]. Mehregany employed a center-pin bushing and bearing to support the rotary micromotor. Long term wear studies (over 100 M rev.) found that wear on the center pin significantly altered the bearing gap, which in turn changed the gear ratio by almost 20% [12]. Beerschwinger *et al.* published a comparative study on various bearing materials and geometries [10]. Test specimens were fabricated to mimic the expected contact areas for a rotary micromotor sliding bearing. Diamond-like-carbon (DLC), silicon, aluminum, alumina, and silicon nitride surfaces were tested. A decrease in the coefficient of

static friction was found for higher loads, leading the authors to suggest that friction was dominated by an attractive mechanism around asperity contacts. Figure 1.1 shows the results of the static friction coefficient vs. normal load tests from this work.
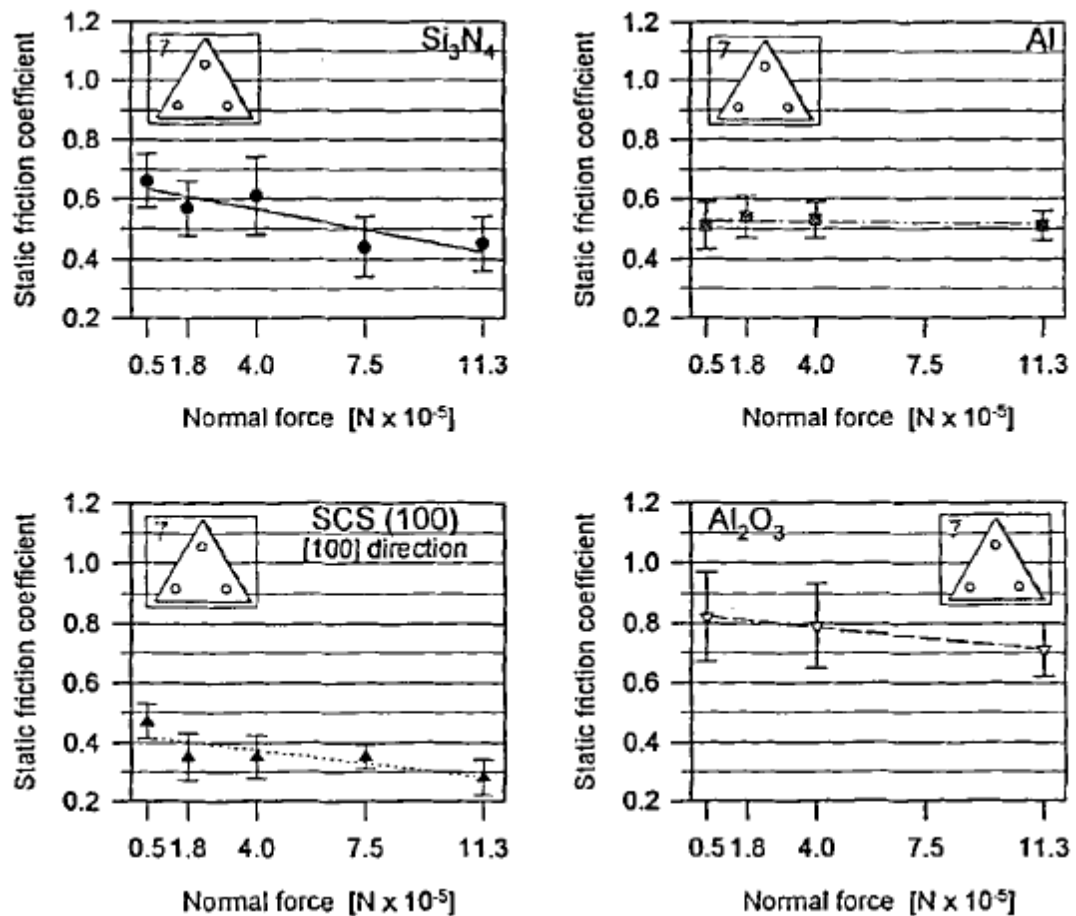
Figure 1.1. Comparison of static friction coefficients for Silicon Nitride, Aluminum, Single Crystalline Silicon (SCS), and Alumina. Each test was performed with a triangular test specimen shown inset. Figure taken from [10].

Beershwinger also seems to have coined the term "microball bearing" in this work. Micro-spheres made of silicon dioxide were used as an interlayer between sliding contacts and were shown to reduce friction by one order of magnitude, although the authors believed that integrating microballs into fabrication schemes seemed unlikely [10]. Sleeve bearings

for rotary micromachines have been fabricated from a combination of X-ray lithography and Ni electroplating with a final coating of hydrogen terminated tungsten carbide. The W:C-H coated sleeves transferred material to the steel counter bearing, accelerating wear, but reducing friction [15]. Studies have been performed on reducing sliding friction, rather than sliding friction bearings, through the use of coatings or geometries. A number of these studies are reviewed in the following sections of the *Introduction* which more closely relate to their application

Liquid bearings have recently been employed in rotary microsystems. It should be noted that these are bearings utilizing liquid rings or droplets isolated by engineering surface hydrophobicity rather than liquid-lubricated sliding bearings. The liquid bearings can be advantageous in that they are inherently low wear, and the low-stiffness liquid bearing has the capability of damping out vibration. Two types of liquid bearings are utilized: dielectric or conductive liquids. The magnetically actuated liquid bearing is shown in Figure 1.2.
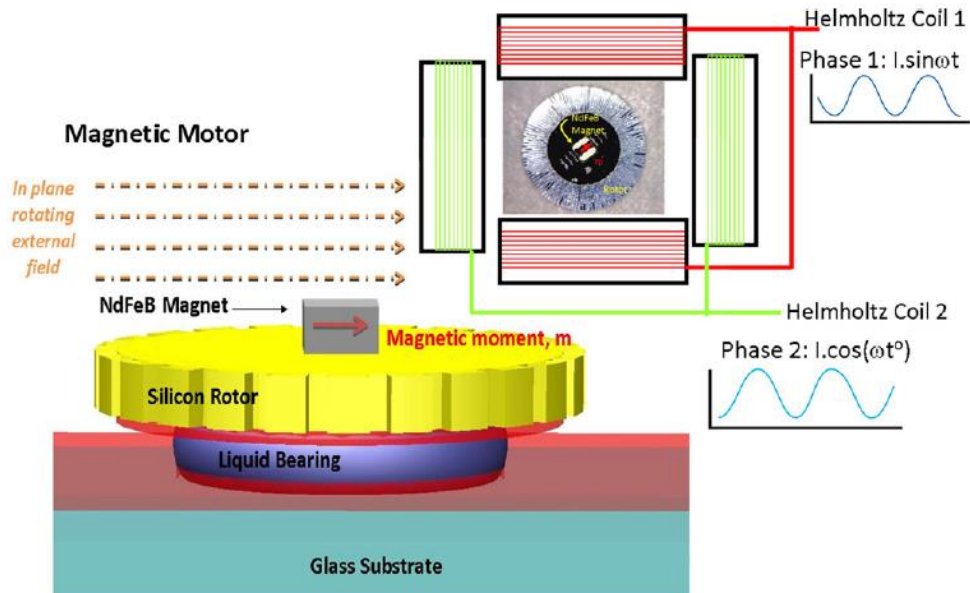
Figure 1.2. Schematic of the dielectric liquid bearing device along with the actuation scheme from

[16]

The liquid is isolated by using hydrophobic Cytop polymer to define the bearing area. The primary source of friction in such bearings is the viscosity of the fluid. In the case of the device pictured in Figure 1.2, water was used as the bearing, and friction torques of 1.2×10^{-3} $\mu N \cdot m/rpm$ were measured [16], which is an order of magnitude higher than those observed for the microball bearings [6]. In a similar work, liquid "balls" were employed and similar friction torques were observed of 0.94×10^{-3} $\mu N \cdot m/rpm$. The main difference with the previous work is that the utilization of liquid balls provided stability by increasing the axial stiffness [17]. An exploded schematic of the device is shown in Figure 1.3
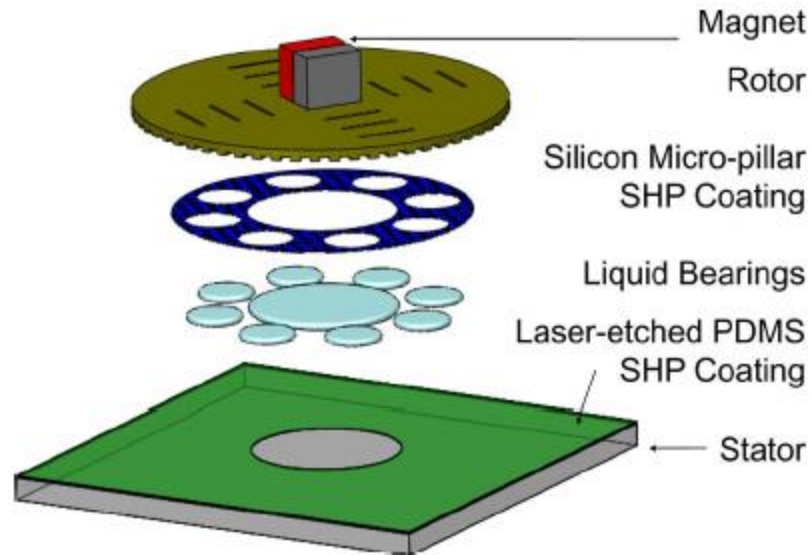
Figure 1.3. Exploded schematic of liquid bearing micromotor containing liquid "balls" for axial stiffness, from [17].

The liquid ball bearing stiffness, which provides a 5.4 µN·m/deg tilt resistance, arises from the liquid balls being discouraged from deforming on the super hydrophobic (SHP), stator [17].

A liquid bearing supported micromotor has also been presented utilizing an ionic liquid as the bearing [18]. The major advantage of this design is that the bearing can be simultaneously used for on-chip electrical communication as well as rotor support. Additionally, ionic fluids have low evaporation rates. The UCLA-developed device utilizes two rings of ionic fluid, confined by black silicon, and through-plated copper vias to make electrical connections to the rotor surface. The ionic fluid is inherently more viscous than water, which limits the speed of the device to 300 rpm because of limits in actuation torque.

The liquid bearings are fundamentally limited in a number of ways. First off, the bearing can evaporate over time, leading to device failure. The evaporation rate of the liquid bearing is related to temperature and therefore the device cannot be operated at high temperatures. The liquid is confined by surface tension forces between engineered surfaces.

At high speeds, centripetal loads will overcome surface tension forces and force liquid out of the confinement area, destroying the bearing. Efforts should be focused on tailoring surface tension to allow for better liquid confinement.

Non-contact, levitated bearings prevent solid-solid contact similar to the liquid bearings. The levitation method is employed to reduce drag versus liquid contacts, therefore tailoring levitated contacts to high-speed applications. An example of a levitated bearing is the hydrostatic air bearing presented in [19]. For this device the rotor was encased in a multi-layered, fusion bonded silicon stator. A cross-sectioned schematic and photograph of this device is presented in Figure 1.4.
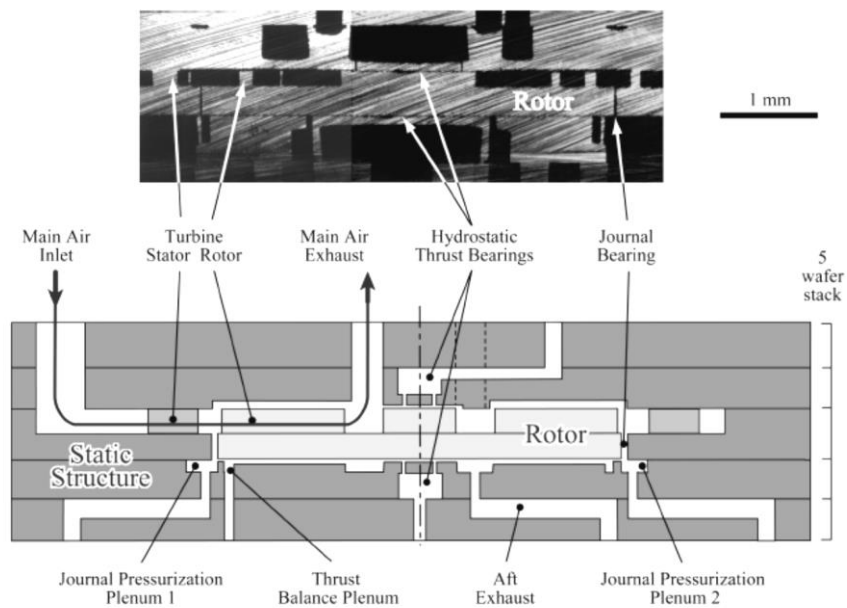
Figure 1.4. (top) photograph of diced wafer stack. (bottom) cross-section schematic of microturbine, showing operation control, from [19].

The rotor is held in the axial direction by pressurized thrust plenums (65-80 PSI), and in the radial direction through the action of the air-journal bearing, which has speed-dependent stiffness. The air-driven microturbine achieved speeds over 1.3 Mrpm but suffered

from two major challenges: journal bearing stiffness at low speeds, and high-speed catastrophic failure due to rotor resonances/imbalances imparted by fabrication defects [19].

Electrostatic and magnetic levitation have also been demonstrated in non-contact bearing schemes. Badilita *et al.* designed a micro-coil fabrication process based on a modified wire-bonding process. The authors then used these micro-coils to create an electromagnet, which subsequently was used to levitate a micro-rotor made of permanent magnets. This device suffered from a lack of radial stability and actuation scheme, the former of which was addressed through the utilization of concentric coils [20]. Diamagnetic (magnetic field repulsing) materials can also be used for magnetic bearings. Garmire *et al.* showed that accelerometers with pylrolitic graphite proof-masses, levitated with diamagnetic bearings, were stable at low frequencies [21-23].

Electrostatic bearings can also be achieved by balancing the electric fields around the rotor. A schematic of the electrostatically-levitated micromotor designed by Han *et al.* is shown in Figure 1.5 [24].
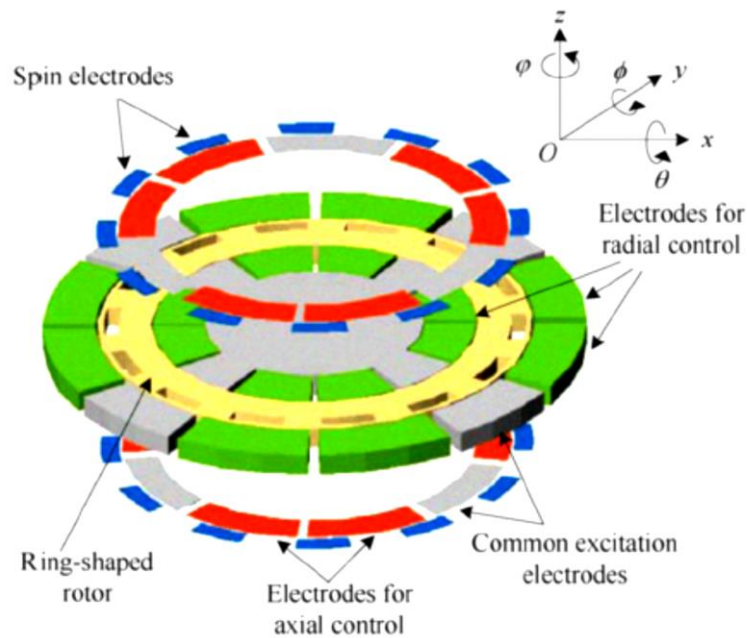
Figure 1.5. Schematic of electrostatically actuated and levitated micromotor, showing various electrode controls, from [24].

This device consists of two main sets of electrodes: the pie-shaped inner stator electrodes for suspension of the rotor, and the outer electrodes for the generation of torque. The cross-coupled nature of suspension and actuation, as well as the highly non-linear stiffness of these bearings makes actuation and control schemes very complex [25].

In summary, contact and non-contact bearings have been reviewed. Sliding contact was utilized in the first demonstration of MEMS bearings, and is continuously improved through the use of modified surfaces and geometries. Liquid bearings provide a new mechanism for non-contact bearings which are not in wide use on the macro-scale. The promise of electrical conduction and mechanical support make liquid bearings very attractive for future, low-speed, sensor applications. Non-contact bearings levitated on compressed gas or via electromagnetic forces provide the lowest possible friction and wear, but are very complex, and challenging to monitor/control. Rolling contact bearings, the subject of this dissertation, will be explored for a number of applications in the following section.

1.4   Microball Bearing Devices
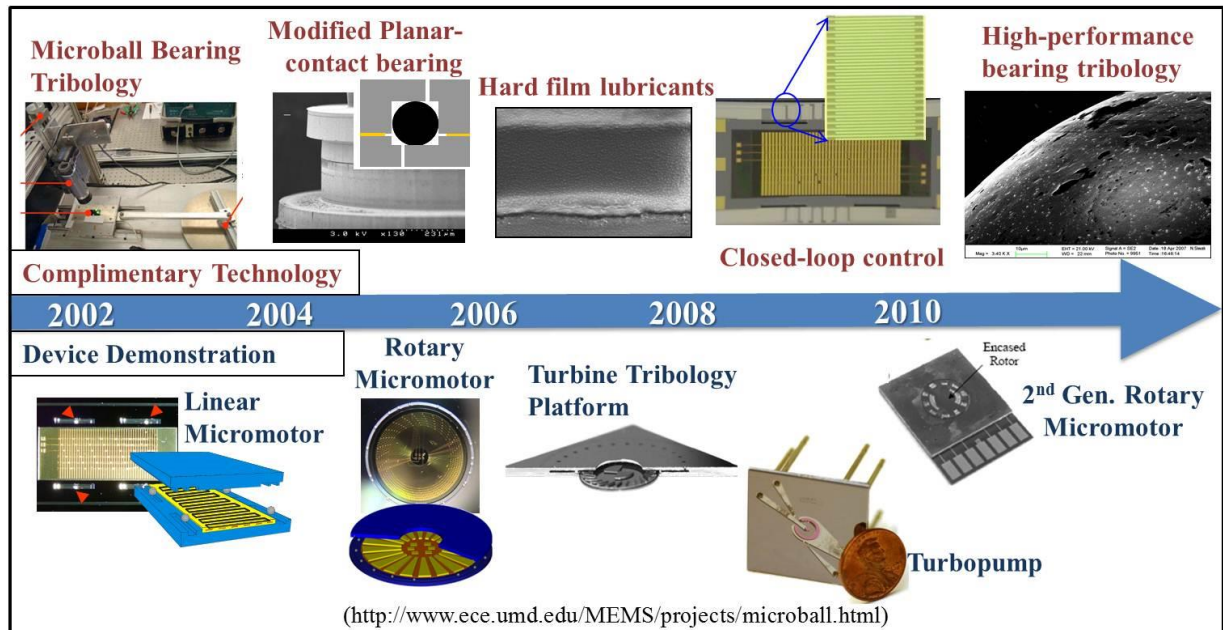
Figure 1.6. Timeline highlighting the parallel progress of microball bearing science and technology with device demonstrations.

The evolution of microball bearing technology has taken two parallel paths: demonstration of new technologies enabled by microball bearings and fundamental study of the tribological properties of rolling contacts within microsystems. The timeline of microball bearing technology is shown in Figure 1.6.

The application of microball bearings was first demonstrated in a linear micromotor by Modafe *et al.* in [26] and Ghalichechian *et al.* in [4]. The first generation of these devices utilized a six-phase, bottom drive, and variable capacitance actuation scheme with open-loop electrostatic excitation. The slider, a moveable component supported by ball bearings, was designed to follow the electrical signals applied on a silicon stator with discrete electrodes isolated and connected through a dielectric benzocyclobutene (BCB) layer. Dynamic

13

characterization of the devices showed a synchronous speed on the order of 7 mm/s over a 4 mm actuation range with occasional loss of synchronization caused by the slight irregularities in the ball raceway.

Correcting the erratic behavior and compensating for random disturbances are required for finely tuned control. Accordingly, a closed-loop actuation scheme was developed by Beyaz *et al.* in[27] as shown in Figure 1.7.
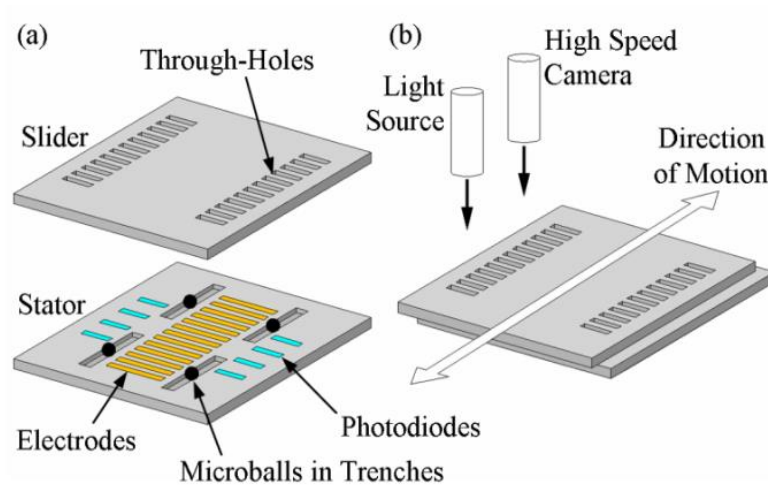
Figure 1.7. Schematic representations of (a) an exploded micropositioner showing through-holes and photodiode structures and (b) the assembled device's operating principle showing the light source and high speed camera for experimental characterization, from [27].

The updated micromotor design includes metal–semiconductor–metal photodiodes on the stator and etched through-holes on the slider to track its relative position. The photodiode outputs were used as a feedback signal in a closed-loop system with proportional control law. Applying the excitation based on this law, autonomous device operation, error compensation, and accurate positioning with speeds up to 20 mm/s were demonstrated. A good comparison between the two excitation schemes is shown in Figure 1.8.
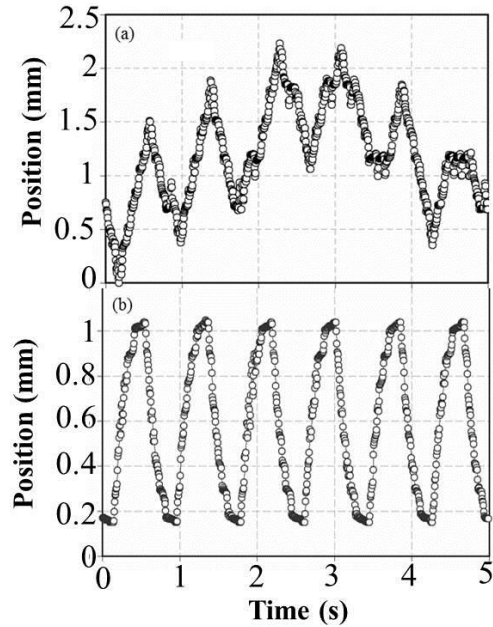
Figure 1.8. Position versus time graphs of the linear micromotor under (a) open-loop excitation, (b) closed-loop excitation from [27].

The linear actuation scheme was then translated into rotary structures for developing micro-scale actuators for a variety of applications. The first rotary micromotor on microball bearings (Figure 1.6) was demonstrated by Ghalichechian *et al.* and was based on the linear actuator presented in the previous section, with the exception that the discrete stator electrodes were arranged radially inside an area defined by the circular ball raceway [3]. After depositing a thin film of SiC on the rotor, a maximum speed of 517 rpm was achieved under an excitation frequency of 800 Hz. The produced torque and mechanical power were measured to be on the order of 5.6 μNm and 307 μW, respectively. Recently, Naruse, et al. demonstrated a low frequency vibrational energy harvester based on linear microball bearing. The constant gap and long travel enabled by the linear ball bearing allowed the device to produce 40 μW at 2 Hz and 0.4 times the acceleration of gravity [28]. These works demonstrate applications where long travel, minimal friction and wear, and good mechanical stability are all uniquely enabled by ball bearing supported MEMS.

While the microballs allowed for continuous rotary motion and stable operation, a key disadvantage of this device was the unrestrained nature of the rotor. The rotating element simply rested on the microballs and was held in place with electrostatic forces. Useful implementation of a microball bearing supported actuator requires direct mechanical attachment and/or interaction with the rotor. Accordingly, encapsulated microball bearings were developed, where the rotor is fully supported by microballs around its entire periphery. These bearings are then used in a rotary microactuator by McCarthy *et al.* in [2] with the same actuation principle as the previous rotary micromotor, but including pneumatic thrust actuation to minimize the normal force that is a direct result of electrostatic excitation. The performance of the encapsulated bearing utilizing micromotor is shown in Figure 1.9. By minimizing normal load, bearing friction is reduced, leading to increased speed and performance.
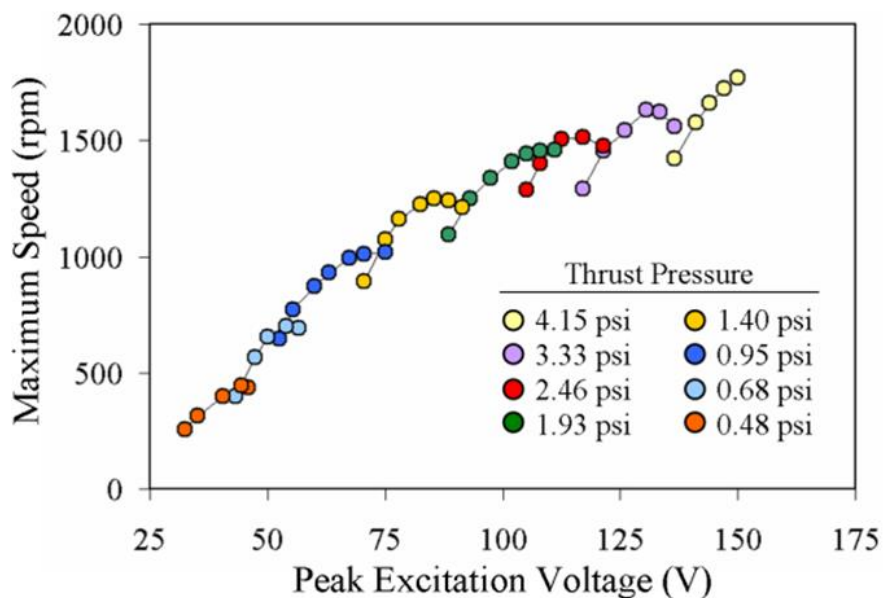
Figure 1.9. Maximum operating speed of the encapsulated electrostatic micromotor over a range of thrust pressures.

The fully supported rotating element was capable of continuous motion and repeatable operation at speeds of 5–2000 rpm, which shows a four-fold increase over the previous design. The failure mechanism at high speeds can be attributed not only to a lack of power available to overcome bearing friction, but also to a loss of synchronization due to perturbations from ideal rotary motion. As speed increases, random vibrations and disturbances associated with ball-to-ball and ball-to-housing collisions may affect the actuators ability to maintain synchronization, a similar case to that observed in the open-loop excited linear micromotor [26]. Additionally, a stator-to-rotor misalignment results in a net radial force that increases the total friction. The improvement on the speed and repeatable operation over the previously demonstrated rotary micromotor is a direct result of encapsulated ball bearings and pneumatic actuation to decrease the normal load. The results discussed here demonstrate the feasibility of microball bearing support mechanisms for use in next-generation rotary microsystems including micropumps and directional sensory systems with electrostatic actuation.

Separately, Waits *et* al. developed a microfabricated turbopump (shown in Figure 1.6) that is capable of delivering liquid fuel with flow rates and pressures required for portable power generators [1]. Consisting of a spiral-groove viscous pump driven by a pneumatically actuated microturbine supported on encapsulated microball bearings, this device achieved speeds up to 87krpm, showing negligible variations in performance over 6 hours and 3.8 million of revolution. During testing, water pumping was demonstrated at flow rates between 10-80 mL/h (Figure 1.10). This example highlights the reliability and high-speed characteristics of the microball bearings that are the main factors in the successful demonstration of a high-speed microturbopump capable of delivering liquids at the micro-scale.
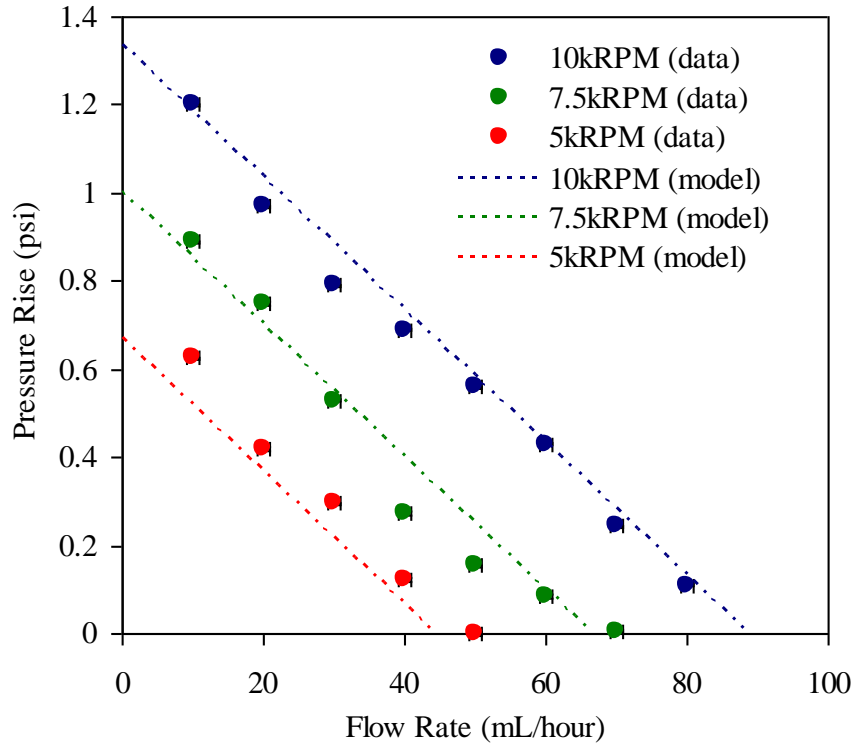
Figure 1.10. Performance curve of micro-turbopump, showing the flow rate versus speed and

pressure, from[1].

In the following sections literature on friction, wear, lubrication, and specialized fabrication techniques will be reviewed on the context of micro-scale systems, with focus on rolling contacts where ever possible.

1.4.1 Friction

Rolling elements have long been recognized by humanity as a low-friction alternative to sliding. Solid wheels were utilized by the Uruk peoples over 5000 years ago, until spoked wheels were invented by the Chinese over 1000 years later. The most famous historical example of ball bearings came from the floating palace on Lake Nemi, Italy, constructed around 44 AD. Brass thrust ball bearings were found in the archeological studies of the site and are often referred to as the first recorded ball bearings [29]. It was not until the Renaissance period before the first theories on the sources of rolling friction were formulated.

The nature of rolling friction was first studied by Leonardo da Vinci in 1490. Leonardo commented on a ball pivot bearing in the Codex Madrid I, noting:

Three balls under the spindle are better than four, because three balls are by necessity certainly always touched, while using four there would be a danger that one of them is left untouched.

Robert Hooke, of "Hooke's Law" fame, made an important observation on the sources of rolling friction in his 1685 discourse on carriages,

The first and chiefest (source of rolling friction)*, is the yielding, or opening of the floor, by the weight of the wheel so rolling and pressing; and the second, is the sticking and adhering of the parts of it to the wheel.*

where he successfully determines deformation and adhesion are two of the primary sources of rolling friction [29]. Rolling friction theory was expanded by Coulomb, determining rolling resistance was proportional to load and inversely proportional to rolling element diameter. A more thorough treatment of rolling friction was performed by Osborne Reynolds (of fluid mechanics fame) where he rolled an iron cylinder over a rubber substrate, noting the travel was significantly less than expected for rigid bodies, and therefore hypothesized that rolling friction came from micro-slip[30]. Slip-derived rolling friction theory was expanded upon by Heathcote [31], for ball bearings in a groove, where he showed that only two regions within the ball contact could undergo pure rolling, and the rest of the contact area was sliding.

In 1954 Tabor [32, 33] argued that interfacial slip could not possibly account for the observed rolling friction, but rather, the friction mechanism is energy dissipated by elastic or plastic deformation. In part I of Tabor's two part study on rolling friction, he concluded that upon initial rolling, friction was dominated by plastic deformation, and once this mechanism

reaches equilibrium, the elastic mechanisms take over. For the elastic case, Tabor first derived the work needed to indent a sphere into a flat plane in incremental distance, and then translate that along a length (rolling) much greater than the contact radius [34]. For the friction experiments, Tabor was able to eliminate interfacial slip by using spheres of the exact same material and geometry and measured a resistance to rolling friction which he determined to be arising from a volumetric hysteresis within the material. A practical approach was taken by Palmgren [35], establishing experimental relationships for various roller bearing systems representative of the manufacturing capabilities of his time.

The adhesive component of rolling friction was first explored by Kendall in [36]. In this work, Kendall described rolling friction as two cracks, or adhesive joints, one continually closing in front of the rolling element, and one continually opening behind the rolling element. Friction arises from hysteresis between the closing and opening forces. The existence of this hysteresis helps to explain the existence of "static" rolling friction and the effectiveness of lubricants. It should be noted that Tabor, when making the case for elastic hysteresis dominated rolling friction, stated lubricants were ineffective reducers of rolling friction, owing to the hysteresis mechanism, but this is only valid for cases where adhesion does not dominate [32]. Kendall found that at higher speeds, the energy to create the contact decreases, while the energy to break contacts increases, thereby increasing the differences between the two mechanisms (coined "adhesive hysteresis"), increasing the value of friction. A separate study on rolling friction found that adhesion dominates at very small displacements (less than the contact radius), the study was unable to differentiate between adhesion and elastic hysteresis at larger displacements [37]. Butt *et al.* found that the rolling friction of microspheres was 0.01 times that of the perpendicular pull-off force, which is an order of magnitude higher than was expected [38]. Ando found that at very low load regimes (nN), chemical bonding did not occur between the contact surfaces, and therefore had a very

small component to adhesion force. The adhesion force increased with the introduction of relative humidity, which resulted in van der Waals forces between the contacting surfaces [39]. Finally, a formulation using Leonard-Jones potentials, relating the deformation and surface energy to the distance which adhesion forces act was completed in [40].

To date, rolling friction is understood to be the complex combination of plastic deformation, elastic hysteresis, differential slip, surface adhesion, and many other minor components. The extent of the contribution of each individual component is strongly dependent on the materials and geometries in question. This work serves in the same capacity as previous studies, to explore the fundamentals of rolling contact in microfabricated rolling bearings for future micro-machines.

The tribological phenomena present in MEMS differ significantly from macro-scale counterparts. This is due to: 1) the increased surface-to-volume ratio obtained from scaling features to shorter length scales and 2) the specific materials systems utilized in integrated circuit microfabrication techniques, which are often times non-ideal for mechanical/tribological applications. Early MEMS tribology efforts focused on the effect of ambient environment on the coefficient of friction (COF) [7]. Several studies utilized atomic force microscopy or friction force microscopy to characterize system level friction [8, 9]. Other studies choose to micromachine structures specific to friction characterization [10, 11]. Regardless, a majority of these studies focused on sliding-regime friction, on micro and continuum length scales, with little focus on the unique realm of micro-scale *rolling* friction.

Ghodssi, *et. al*, first characterized the static friction in a microball bearing supported linear actuator [41]. This work studied the interaction between stainless steel microballs and different micromachined materials systems. From here, the research of Lin, et. al, [42] and Tan et. al [43] modeled the friction of various configurations of a microball supported linear actuator, with special attention paid to the effects of speed and load. Lin et al. found COF

values between 0.007 and 0.015 if there is no ball-on-ball contact in a free sliding linear bearing. Tan et al. expanded on the work in [26] and created a viscous model for a steel ball rolling on a silicon plane and predicted COF of 0.007 for speeds $\pm$ 0.2 m/s.

McCarthy et al. [6] performed a thorough characterization of a microturbine supported on microball bearings, deriving a power law relationship between friction torque and normal load, which lacked physical relation to contact mechanics. This work provided the original version of the device (microturbine), and testing methodology (spin-down), which were modified and used throughout this dissertation.

1.4.2 Micro-scale wear

The wear mechanisms present in microfabricated systems differ significantly from macro-scale counterparts and therefore need to be specifically addressed. This difference is due to: 1) the increased surface-to-volume ratio obtained from scaling features to shorter length scales, enhancing the influence adhesion and 2) the specific materials systems utilized in integrated circuit microfabrication techniques, which are often times non-ideal for mechanical/tribological applications. Wear studies within the MEMS domain are typically split into two experimental categories[44]: *in situ* testing [45, 46] in which wear is qualitatively described by observation or characterized by a number of cycles or device lifetime [6], or tribometer-based studies [47-49] where contact is initiated in a pin-on-disc methodology utilizing MEMS materials of interest. A classic example of *in situ* wear testing of micromachined silicon structures was performed by Mehregany *et al.,* where the authors fabricated a side-drive polysilicon wobble motor [13]. The motor rotational speed is a function of the gap between the rotor and stator which changes gradually with the wear of the contact bearing. The authors determined that there were three primary regimes of operation for such a device: the burn-in period where large asperities on the bearing from the reactive

ion etching are smoothed, the break-in period where the speed of the motor gradually increases from smoothing of the surface roughness, and the rotor slip region where the rotor speed departs from the exciting voltage due to slip. Tambe *et al.* published a study that highlighted the scale and material dependence of tribological phenomena using a micro-tribometer for the micro-scale portion and a modified atomic force microscope (AFM) for the nano-scale study[8]. In this study, the adhesive force between contacting materials showed a strong dependence on residence time, humidity and temperature, which can be related to water vapor-derived meniscus forces developed between the contact point and substrate. Additionally, a velocity dependence on friction force was discovered for multiple material systems, further strengthening the argument that tribological phenomena are strongly scale dependent. Ku *et al.* bridged the gap between *in situ* testing and a tribometer by fabricating silicon thrust contact bearing geometries to act as the pin of the pin-on-disc methodology [50]. The authors found a significant dependence on surface state of the measured coefficient of friction and wear rates. This result was deduced from a comparison of samples tested immediately after oxygen plasma cleaning and samples left out in "room air" for a period of 15 hrs. A majority of these studies are focused on sliding regime wear mechanisms on micro-to-nano length scales, with little focus on the unique realm of micro-scale *rolling* contact.

Thin film coatings are capable of greatly affecting the tribological properties of a system owing to the fact that friction and wear phenomena generally initiate at the surface or near-surface of contacting bodies. Two regimes exist for the use of solid thin films in a tribological system: those that act as lubrication and wear in a manner that reduces friction, *e.g.*, graphite [51] or molybdenum disulfide [52]; and those that remain intact and provide a reduction of chemical affinity for the contacting surfaces or enhance the mechanical properties of the surfaces. Solid film lubricants are typically used in situations where it is difficult to maintain a fluid film boundary layer, such as high load or high speed operation.

Hard thin films are used in applications where debris generation is not tolerable. In the current demonstration of microball bearings, hard film coatings are employed to alter the surface mechanical and chemical properties in an attempt to enhance the tribology of the overall system. Bandorf *et al.* utilized a number of carbon-based thin films to minimize wear and friction coefficient. This work found that the influence of the mechanical properties of the substrate played a significant role in reducing wear depth in tape-abrasive testing, increasing the tape length (lifetime) to obtain a given wear depth by almost an order of magnitude by using a polymer substrate versus silicon [53]. It was also found that increasing film hardness improved the tribological properties of the system. In summary, a majority of the micro-scale wear studies described above have highlighted the importance of both substrate and thin film materials properties regarding wear.

1.4.3   Micro-scale lubrication

The principal interest in studying adhesion in MEMS is to mitigate a phenomenon called stiction (the etymology comes from "sticking" + "friction" [54]). Stiction, which is the adhesion of compliant microstructures initiated via capillary forces during release processes or during an event where a compliant structure is brought into intimate contact with a mating surface. Often times the adhesion cannot be reversed resulting in ultimate failure of the device. Stiction was a primary sub-field of MEMS in the mid-1990s with many studies focusing on chemically altering surfaces, applying micro-scale features to minimize contact area, or developing advanced fabrication/control methods to prevent it from occurring [55-57]. The issue of catastrophic stiction can now be confidently avoided, so current adhesion studies are not focused on the aspect as much as reducing the remaining adhesion in the system to improve reliability.

A significant barrier to the realization of long-term reliable MEMS is the reduction of friction and wear between surfaces [58]. One possible solution is the integration of lubrication between contacting surfaces, a technique which is widely adopted on the macro-scale. MEMS level lubrication must be conformal, continuously replenishing/low wear, and low viscosity to prevent power dissipation from viscous drag and capillary forces. Two lubrication options arise: hard thin-film coating or vapor-phase lubrication (VPL). Hard-film coatings in the form of diamond or diamond-like carbon [59], carbides [60, 61], and nitrides [49, 62] have been extensively studied. It is difficult to obtain conformal coatings using conventional microfabrication techniques due to increasingly more complex device geometries. Additionally, once deposited these coatings cannot be replenished in the inevitable case of wear. Vapor-phase lubricants provide conformal, replenishing lubrication without the viscous drag and capillary forces (arising from a minimization of surface energy) associated with liquid-phase lubrication.

Adhesion can be specifically addressed with vapor-phase lubrication by using the adsorbed molecules to lower surface energy. In VPL, molecules leave the vapor-phase and conformally assemble on surfaces, dependent on the adsorption isotherm. The lubricating molecules can reach spaces as small as the mean-free-path of the gas, which depends strongly on the composition and pressure. Surfaces are constantly replenished by lubricating molecules exiting the gas phase in order to maintain thermodynamic equilibrium. This constant replenishment takes place on the order of 10^{-9} seconds (derived in chapter 5), and can therefore be applied to most MEMS with reciprocating motion.

VPL is present whenever a device is operated outside of the controlled lab environment in the form of adsorbed water (assuming some humidity in the lab). The thickness and morphology of the adsorbed water layer has been shown to vary with the partial pressure of water (humidity) in air at room temperature [63]. Multiple studies have

shown the potential benefits of adsorbed water as a lubricating layer in various MEMS, reducing friction and wear [64-66]. Although convenient, water is not the ideal candidate for adsorbed lubricants due to its high surface tension.

Alcohols are employed in VPL schemes because they meet the compatibility requirements of high vapor-pressure at room temperature and low surface tension. Strawhecker *et al.* designed a bubbler system to deliver *n*-pentanol to an atomic force microscope [67]. This set-up was used to establish a relationship between pull-off force (adhesion) and relative saturation of the alcohol vapor, which was reduced to below 50% of the value of dry air for a 50% saturated vapor [63]. In a similar work, Asay *et al.* microfabricated test structures to determine the performance of 1-pentanol VPL on the mm to nm size scale. Through the introduction of 8% saturated (relative to dry nitrogen), the millimeter and micrometer structures showed a reduction in friction coefficient by a factor of 3, and virtually zero wear over the time scale measured (Figure 1.11) [45]. Additionally, the authors showed a 4 orders of magnitude increase in device lifetime for devices operated under VPL versus devices operated in dry air, attributed to a reduction of adhesion. Barnette *et al.* studied a similar system and determined that a tribo-polymerization of the VPL molecules was taking place near the area of contact in the system, although it did not have a significant effect on the tribological properties [68].

There is no existing literature on VPL for micro-scale rolling contact. This work on the friction of micro-scale rolling contacts within a MEMS microturbine hypothesized an adhesion-dominated friction mechanism, which was supported by experiments on increasing contact area (chapter 3). On the macro-scale, VPL for rolling contact has been studied in primarily high-temperature environments, above the boiling point of many organic liquids. Macro-scale rolling friction differs in nature from the micro-scale, placing a greater emphasis

on volumetric properties, specifically elastic hysteresis. Therefore, VPL is not expected to be as effective in macro-scale systems as it is on the micro-scale.
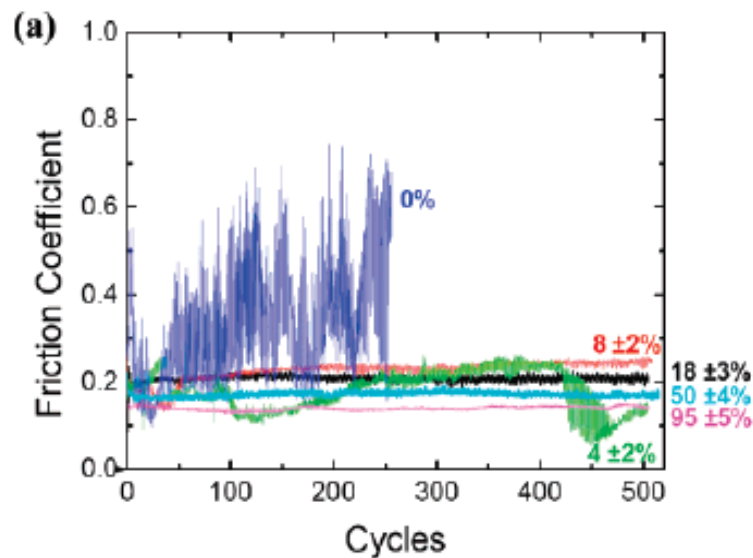
Figure 1.11. Friction coefficient measured with a ball-on-disc tribometer under various levels of pentanol saturated environments from [45].

1.4.4   Advanced fabrication technology for new bearing geometries

The geometry of the silicon micro-bearings is dictated by the microfabrication techniques used to etch the bearings. Steel macro-bearing raceways are machined to near-net shape, heat treated and then lapped to achieve a mirror finish. The radius of the steel raceway is altered depending on the expected radial and thrust loads, that dictate the contact angle of the ball to with respect to the raceway. Microfabricated bearings are machined in silicon. Silicon micromachining takes place either by dry or wet etching, isotropically or anisotropically. Anisotropic etching techniques have a preferential direction, dictated either by the crystal structure of silicon as in the case of potassium hydroxide solution etching, or by exploiting passivation layer techniques for anisotropy, as in the case of deep reactive ion etching (DRIE). The DRIE process uses alternating etching and deposition steps to etch and

27

passivate silicon surfaces, respectively. Silicon sidewall passivation is more resistant to etching due to the ion directionality imparted on the plasma, therefore etching through the depth takes place significantly faster than etching laterally and rectangular cross sections are obtained. A thorough review of DRIE can be found in [69]. The DRIE method is used to fabricate the rectangular cross-sectioned bearings used in the current microturbine device. The rectangular cross section provides a nominally flat, non-wavy surface for the balls to contact, simplifying contact mechanics calculations.

3D fabrication techniques allow a range of structures that would otherwise be unobtainable through traditional, planar microfabrication methodologies. Successful demonstration of 3D fabrication has been performed in the lithography, deposition, and etching domains. Grey-scale lithography utilizes variable transparency to obtain sloped profiles in photoresist. The sloped profiles can then be etched into the substrate material to obtain 3D structures such as micro-compressors [70] or optical fiber alignment [71] devices. The challenges of this technique include obtaining a consistent photoresist process and the significant difference in selectivity between substrate and photoresist in most etching schemes, which magnifies photoresist defects. Other 3D lithography techniques include "two-photon" lithography where a stereo light source is focused on a single spot within a photo-active material. The coincident point of the two light beams contains enough energy to alter the material, whereas each single light source does not. Until recently the technique was extremely slow, therefore unreasonable for multi-device fabrication [72], recently however the speed has been increased by orders of magnitude [73]. 3D deposition techniques typically involve localized energy sources in reactive environments such as localized electrochemical deposition [74] and focused ion beam deposition [75]. Both of these techniques are extremely slow compared to processes taking place on the wafer scale and are therefore not in common use.

Isotropic etching techniques have been employed since before widespread adoption of silicon-based transistors. The original isotropic silicon etch was based on hydrofluoric, nitric, and acetic acid (HNA) chemistry, described in the seminal series by Schwartz. *et al.* determining the etch rates, roughness, and uniformity of the HNA etch based on the composition of the acid [76]. The HNA etching chemistry is not completely independent of crystal structure which limits its use as a nearly-perfect isotropic etch to shallow etch depth before the anisotropy is realized. A wet etch process requires very careful process control of temperature and agitation, making it difficult to establish wafer-to-wafer uniformity [77].

Dry, plasma-based, etching techniques are most relevant to this work. Utilization of ICP etching techniques for isotropic profiles in silicon was first simulated by Marcos, *et al.* in [78]. Modification of the power profiles of etching and deposition steps within a DRIE process allowed for the realization of controlled cross-section thickness through the height of a column [79]. Gantz, *et al.* modeled and demonstrated an RIE-lag based method for 3D etching. In this work, masks were created using variable feature sizes and pitches to control the exposed area of reactants, and thus control the final etch profile [80]. The work by Larsen, *et al.* utilized a multi-step plasma process to create micro-lens molds. The authors performed a thorough study on etching parameters and the evolution of etch geometry [81]. The micro-lens study was a significant influence towards the development of the isotropically etched ball bearing raceways which are the focus of this study.

1.5   Dissertation outline and structure

This dissertation deals with a wide range of topics within the realm of tribology, pertaining to micro-scale ball bearings. The introduction provided a background for this research and touched upon relevant research in the sub-fields of tribology. Chapter 2 is a general introduction to the microball bearing design, fabrication, and mechanics. The three main chapters correspond to the three primary sub-disciplines within tribology: 3. Friction, 4. Wear, and 5. Lubrication all are intimately linked. Following these sections, two engineering studies are presented. Chapter 6 presents a new fabrication method based on isotropic etching to create groove-shaped raceways, justified by calculations made in chapter 2. The next chapter (7) presents the utilization of a MEMS accelerometer to perform diagnostics on a rotary MEMS device. Chapter 8 summarizes this work, enumerates a list of contributions, and presents new ideas and directions for future, related research.

2. Microball bearings

2.1 General design and fabrication

A microball bearing consists of deep-etched silicon raceways containing off-the-shelf stainless steel microballs, shown in Figure 2.1. The ball diameters range from 285-500 μm in all subsequent studies.
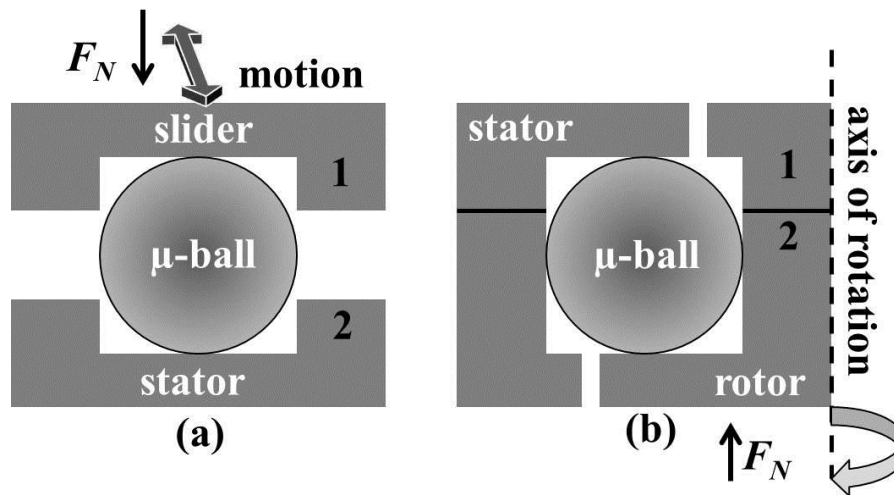
Figure 2.1. Schematic cross-sections of two microball bearing configurations. (a) Microball bearing is placed between two unbonded wafers 1&2, and (b) encapsulated bearing with microballs placed in etched silicon trenches between bonded wafers 1&2. Designed direction of normal load is shown (F_N).

Each of these configurations provides low friction and wear by harnessing the strength of the contacting materials and utilizing rolling contact instead of sliding. The tribology of microball bearings diverges from macro-scale bearings due to the unique materials systems and geometries used, and therefore needs special consideration.

Devices designed to utilize microball bearing support mechanisms in concert with sensing and actuation payloads need to take into account the loads and speeds encountered during operation. Considering MEMS fabrication is planar in nature, a majority of devices

will have active components on the top or bottom surfaces of the moving part (slider/rotor), e.g., actuation electrodes on the bottom of an electrostatically actuated micromotor. This results in normal loads that transverse through the thickness of the device. The resulting axial loading is best accommodated by thrust-orientation microball bearings, which have been exclusively considered to-date.

.

2.2   Load and speed considerations

The following discussion will be focused on the rotary bearings, but similar principles apply in the case of the linear bearings.

Rotor normal load needs to be taken into consideration when determining the global microsystem geometry. Ideally, the microball should contact a flat silicon surface, rather than an etched sidewall feature, such as the bond interface in the encapsulated bearing configuration (Fig. 1b). Additionally, the contacting materials need to be considered when determining the loads expected within the engineered microsystem.

The contact pressures beneath each microball can be on the order of MPa-GPa for rotor normal loads in the mN range due to the minute radii of microball bearings, calculated from Hertzian contact mechanics [46]. The expected normal load will determine the diameter and number of balls needed to ensure the contact pressure is well below the fracture strength of the contacting materials. The diameter and number of balls will subsequently determine the radius of the rotating structure needed to accommodate the microballs.

Future microball bearing systems will need to operate at high speeds (>50 krpm) for a number of applications. The centripetal force acting on the rotating balls scales with *velocity*^{2}, therefore the radial forces on the ball bearing will eventually overcome the static coefficient of friction between the ball and raceway and encourage the ball to ride against the

32

sidewall. Figure 2.2 graphically illustrates the operation regime for various rotor normal loads for a rotor supported on 100 stainless steel microballs (Ø=285 μm).
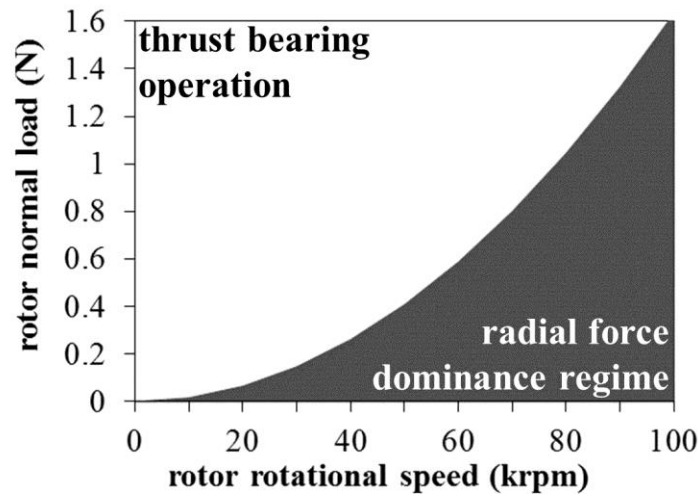
Figure 2.2. Guideline to ensure proper ball orientation during operation within microfabricated thrust bearings.

Figure 2.2 implies that if high-speed operation is desired, high rotor normal loads must be imparted in order to maintain the thrust-oriented rotation of the balls, at the expense of potential accelerated wear rates at higher loads. Within the radial force dominance regime, the balls preferentially roll on the sidewall, decreasing the axial stability of the system. Static friction, scaling with rotor normal load, is the only force resisting the radial movement.

2.3   Fabrication

Future microball bearing-enabled microsystems are expected to be rotary in nature due to the wide range of possible applications. Rotary microball bearing-based devices are fabricated by placing microballs within two bonded deep reactive ion-etched (DRIE) raceways in silicon. Currently, the raceway is designed to be 10 μm wider than the width of the microball, chosen to mitigate ball jamming while allowing for reasonable alignment tolerances. The bearing exhibits no play in the thrust direction due to the normal force on the

rotor/slider keeping the balls in contact with the thrust surfaces. In the encapsulated bearing (Fig. 1b), the bearing raceway depths are asymmetrically etched such that one bearing is designed to be 60% of the ball diameter deep and the other 40%. The purpose of the offset etch depths is to prevent the ball from contacting the bond interface during operation. A generalized fabrication flow for an encapsulated microball bearing supported microsystem is shown in Figure 2.3.
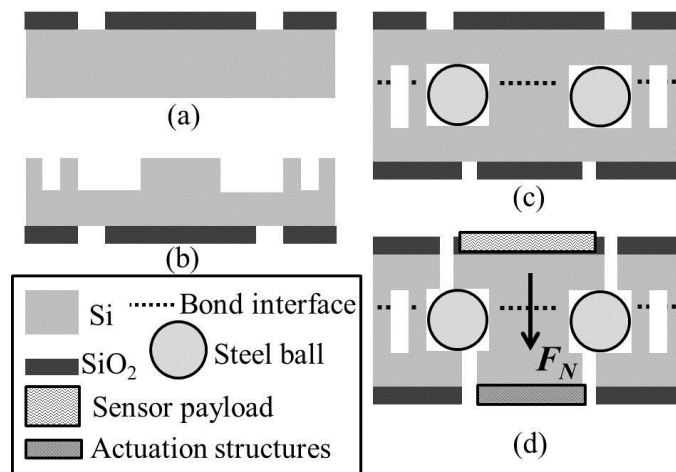
Figure 2.3. Generalized fabrication flow for a microball bearing supported microsystem. (a) Pattern release structures in the SiO_2 hard mask for future processing. (b) Etch offset raceways and alignment structures in two silicon wafers using nested DRIE techniques. (c) Place microballs in a raceway half, and bond to matching raceway. Pattern sensor/actuator payloads. Finally, (d) etch release structures to transfer support to microballs and allow rotor movement. F_N is normal load.

The rotor release etches (Figure 2.3d) disconnect the rotor from the stator. This etch takes place offset from the center of the microballs, therefore an asymmetry is created in the microfabricated thrust bearing. The rotor normal load needs to be in the intended direction (Figure 2.1b) to ensure the ball rolls on flat silicon surfaces, as opposed to etched silicon corners. A example fabrication schematic of an encapsulated bearing, used in a silicon microturbine can be found in [1] as well as in the following sections.

2.3.1 Linear Device fabrication

Silicon microchips with linear raceways were used for initial friction and wear testing. These devices closely resembled the linear micromotors presented in [27] without the electronic components. These devices were fabricated in a simple process, using either KOH-based wet etching, or DRIE based dry etching to obtain angled or rectangular raceway cross-sections, respectively. The fabrication scheme for both devices is presented in below.
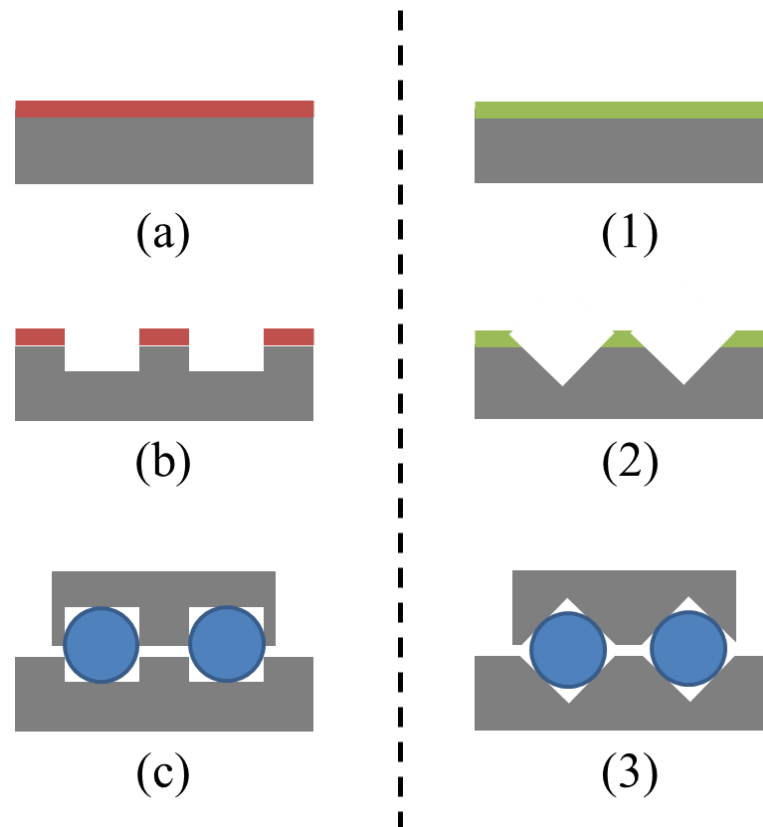
Figure 2.4. Linear testing device fabrication scheme. (a) spin photoresist, (b) pattern photoresist and DRIE raceways, and (c) assemble matching stator and slider. (1) LPCVD Silicon Nitride, (2) pattern nitride and KOH wet etch raceways, and (c) assemble matching stator and slider.

Friction testing was performed on both the rectangular and angled (DRIE and KOH etched, respectively) raceways. The wear testing and all thin-film coated linear device testing was performed on the rectangular, DRIE raceways to mimic the rotary devices.

2.3.2   Rotary microturbine

The microturbine rotor is comprised of two silicon wafers, one containing a shallow-etched race and the second containing a deep-etched race to form an offset bearing interface. A third wafer acts as a plumbing layer to direct the internal flows. An offset bearing interface is necessary to prevent ball contact on the corners of the bonded wafers, shown in previous work to be a significant source of wear [6]. Mechanical ball alignment structures are incorporated on each layer to provide the accurate alignment. To obtain offset interfaces and ball-radius-deep alignment pits simultaneously, an asymmetrical etching scheme is employed. The fabrication flow is shown in Figure 2.5. A 2 µm silicon dioxide hard mask is patterned containing the ball alignment pits and raceways on both device wafers.
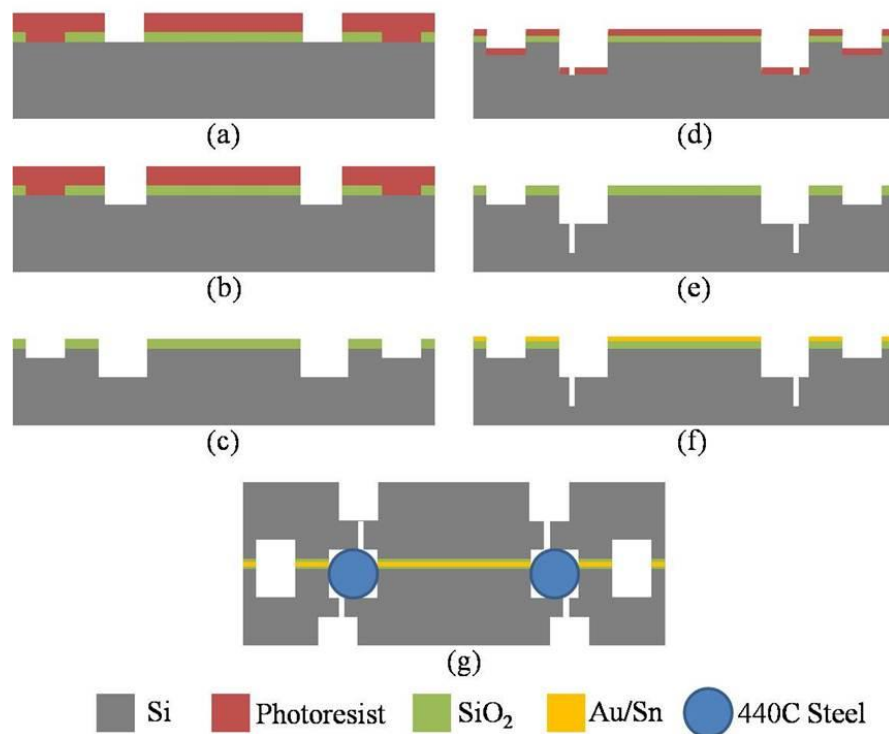
Figure 2.5. Simplified fabrication flow for microfabricated micro-tribology device. (a) pattern resist to define races. (b) DRIE etch raceway only. (c) strip resist and etch raceways and alignment pits. Shallow-etched raceway wafer follows opposite lithography steps ,i.e., pre-etching of alignment pits, strip resist, then etch to define shallow raceways. (d) spray-coat photoresist to pattern journal etch.

(e)DRIE of journals bearings. (f) Evaporate gold bonding layer. (g) Wafers are bonded and device is etched from top and bottom to release rotor. Balls are omitted from the alignment pits for clarity.

Photolithography is then used to select features to be exposed to the first DRIE raceways for the deep-race wafer (Figure 2.5a, b) and alignment pits for the shallow-race wafer. The photoresist is then stripped off both wafers with O_2 plasma, exposing all features. The deep-race wafer is then etched to a depth of 50% of ball diameter (Figure 2.5-c), resulting in 60% ball diameter raceways and 50% ball diameter alignment pits. Similarly, the shallow-race wafer is etched a depth of 40% ball diameter, resulting in 50% alignment pits. Rotor release trenches are etched into the bottom of each raceway using spray-coat lithography and DRIE (Figure 2.5d, e). The non-race-side of each wafer is patterned with either a radial in-flow turbine structure with tracking marks on the shallow-race wafers, or a release structure on the deep-race wafers. Separately, a shadow mask is created by through-etching features into a silicon wafer. A eutectic composition gold/tin bonding layer is then evaporated onto the shadow-masked shallow and deep raceway wafers (Figure 2.5,f). The wafers are mechanically aligned with microballs in matching etch pits and then eutectically bonded in an H_2N_2 atmosphere at $330^{o}C$ and 1kN force. The binary phase diagram for the Au-Sn system is shown in Figure 2.6 from [82]. The turbine and release structures are etched to meet with the inset journal bearings, releasing the rotor from the bonded wafer stack (Figure 2.5,g). The dimensions of a completed bearing are presented in Figure 2.7.
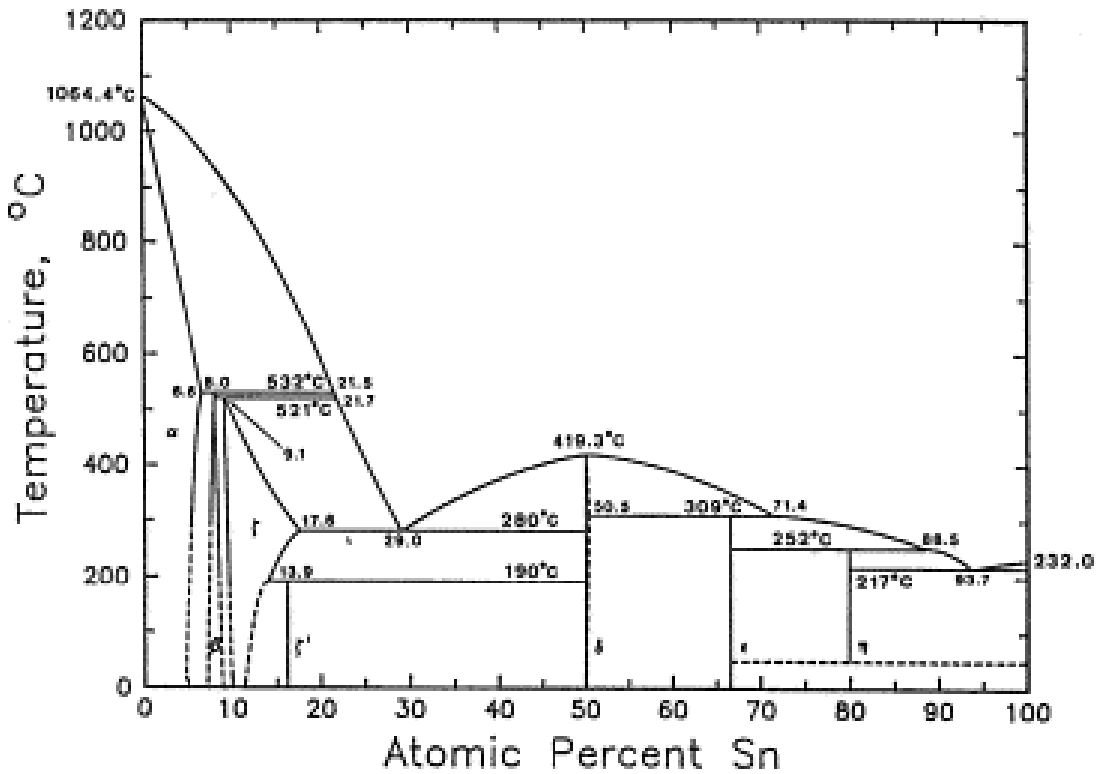
Figure 2.6. Binary phase diagram of Au-Sn system from [82].

Eutectic bonding was chosen for the method of encapsulating the bearings because of the relatively forgiving nature of surface quality, low temperature requirements, and compatibility other aspects of the fabrication process. The phase diagram relates the equilibrium states of a material system given composition and temperature. Compositionally, the left and right axis represent pure concentrations of the elements in the system. The x-axis is a linear variation of composition, expressed in terms of atom % or wt%. Areas in contact with the liquid phase of the diagram represent a combined liquid + solid mixture, whose combination can be determined by the lever rule. The most significant feature of this phase diagram is the composition which contains no liquid + solid intermediary phase, but rather a direct and complete transition from liquid to solid phase. This composition is called the eutectic composition of a binary system and is the composition desired for minimum melting point. The melting point of the eutectic composition (the eutectic point) is often significantly

lower temperature than one or both of the individual components which is taken advantage of in microfabrication processes.
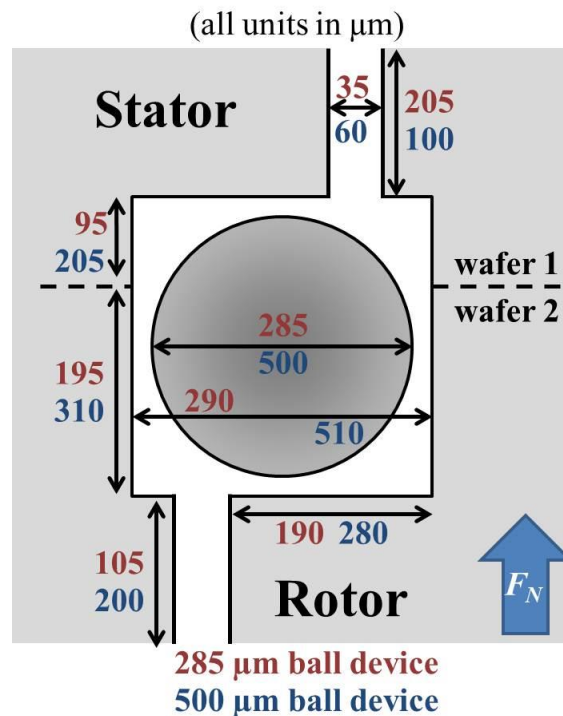
Figure 2.7. Schematic of two tested ball bearing geometries in etched silicon housing.

The bearing surfaces are characterized with optical profilometry to ensure consistent surface properties amongst different devices. Devices with significant roughness are discarded. The roughness of the deep raceway is root mean square 5 nm, with the roughness of the shallow etched raceway being slightly less. There is a slight curvature to the bottom of the raceways, a typical product of the etch process. For first approximations of contact mechanics, the raceway is assumed to be flat. While the sidewall roughness isn't characterized, it is known to be a function of the ratio of etching to deposition time in the DRIE process. Ideally, the balls will not contact the sidewall because the frictional force opposing radial sliding should be greater than the centripetal force acting on the balls radially. The yield of the devices was around 85% with one of the seven potential devices on a wafer having a significant raceway defect.

The current iteration of air-driven MTD has a number of minor modifications compared to the device described in [6]. These include:

(1) The utilization of 500 μm balls, which required the scaling of raceways and journal bearings

(2) Turbine blade height increase from 100 μm to 200 μm, reducing the resistance to flow through the turbine structure, thus reducing the pressure required for high-speed operation,

(3) Decreasing the race width tolerance from 3.5% to 2% ball diameter to reduce radial play and thus the force of sidewall contact,

(4) Utilization of various ball packing numbers in the race from 90% complement originally to 99% or 75% full complement, to address the effects of varied ball contact area.

2.4   Microturbine Platform and packaging

The rotary friction study is focused on exploring the fundamental tribology of the microfabricated encapsulated ball bearing within the platform of a microturbine. Four different variations of the microturbine have been tested: two raceways designed to accommodate 285 μm or 500 μm diameter balls each tested at 75% and 99% ball packing, with the goal of specifically addressing contact area (referred to herein as *285, low*; *285, high*; *500, low*; and *500, high*). Microturbine performance is monitored throughout the lifetime of the device, which in turn is related to the wear mechanisms within the microfabricated ball bearing system. The friction torque is evaluated using the turbine operation curves and spin-down deceleration testing. From this test, the effect of load and speed on friction torque can be deduced.

The microturbine described in [6] has been modified to accommodate either 285 µm or 500 µm diameter balls while maintaining the same rotor diameter and turbine blade geometry.

Table 2-1 lists the parameters for the four variations of tested devices. A schematic of the microtribology device (MTD) with 440C Stainless steel balls is shown in Figure 2.8.

Table 2-1 Pertinent microturbine geometry parameters

Ball Diameter	Rotor Diameter	# of Balls	Reference name
285 µm	10 mm	75	*285, low*
285 µm	10 mm	100	*285, high*
500 µm	10 mm	45	*500, low*
500 µm	10 mm	60	*500, high*
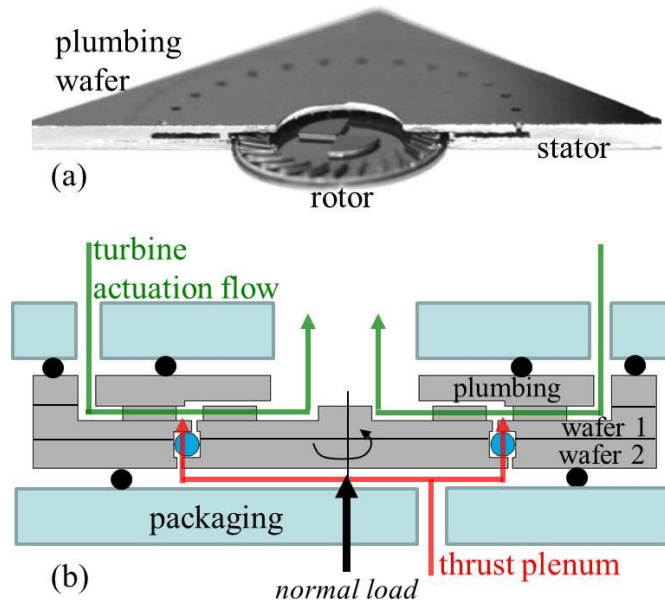
Figure 2.8. (a) Photograph of cross-sectioned MTD stator with rotor inserted. (b) Cross-section schematic of packaged device showing the bonded wafers comprising the rotor and stator, as well as actuation flows and the direction of normal load.

This device was selected because of the ability to perform normal load resolved spin-down testing, high fabrication yield and consistent surface quality within the races. As shown in [2], the encapsulated bearings can be integrated into integrated circuit (IC) fabrication flows to create future motors, generators and sensors.

The MTD package (Figure 2.8(b)) allows for thrust load and turbine actuation to be controlled by two separate flow paths. The MTD is actuated via the turbine flow routed through the package, into an array of holes around the periphery of the plumbing wafer (Figure 2.8(a)), through the turbine structures and out the center of the rotor. The thrust plenum is used to apply normal load on the rotor during testing. Thrust plenum flow leaks through the bearings and out the center of the rotor. There is a pressure drop across the rotor from the measured input pressure to atmosphere at the center of the device. The thrust pressure is static across the rotor, therefore the device package ensures that the net force on the rotor will be in the intended direction.

2.5   Thin Film Coating

TiN, SiC, and ultra-nanocrystalline diamond (UNCD) thin films were chosen to coat the raceways because of their high hardness and their compatibility with microfabrication techniques. SiC and TiN films were sputtered onto a bare silicon substrate after successive O_2 plasma and Ar plasma cleaning steps. The SiC films were sputtered in an *AJA ATV 1800-V* sputtering tool to a thickness of 250 nm from a SiC target in an Argon atmosphere. The chamber pressure is held at 2.5 mTorr and the DC sputtering source is operated at 1 kW without any external substrate heating. It is assumed that these conditions produce an amorphous film, supported in [61].

TiN films were deposited in a reactive sputtering process in a *CVC 610* sputtering tool. First, a thin Ti adhesion layer was deposited at 5 mTorr, and 1 kW, in an Argon environment. Next, TiN was sputtered from a Ti target in an N_2 plasma at 2-5 mTorr and 1 kW after a 30 min pre-sputter that forms a nitride layer on the surface of the target. Reactively sputtered TiN is typically stoichiometric and has a columnar grain structure [83]. The total film thickness of the Ti/TiN stack is 250 nm. The mechanical properties of these films have been explored by nanoindentation methods and are summarized in Table 4-3

The precise methodology for creating UNCD films involves consecutive seeding and film growth steps using microwave plasma chemical vapor deposition (MPCVD) methods. Initial studies done on UNCD films deposited onto specially fabricated silicon wafers by our collaborator at the Center for Nanoscale Materials (CNM) at Argonne National Lab have shown very encouraging results after friction and wear testing.

2.6   Bearing contact mechanics

Contact mechanics define the stress and strain of bodies in contact. Contact mechanics is relied heavily upon by tribology studies where understanding the interface between materials is critical, using concepts from the mechanics of materials. In 1882 Heinrich Hertz began the field of contact mechanics with the publication of "On the Contact of Elastic Solids", which was actually focused on trying to understand the optical properties of lenses when they are stacked atop one another [84]. It was not until 1982 that Johnson, Kendall, and Roberts (JKR) updated Hertzian contact theory [85].

Hertzian contact mechanics is useful to make an approximation of contact pressure, contact area, and deformation. Hertzian contact makes a number of assumptions, including: elastic strain below the strain limit of the contacting bodies, friction-less contact, surfaces are continuous and non-conforming, and the areas of contact are significantly smaller than the characteristic lengths of the body. Hertz showed that radius of contact for a sphere on a plane was as follows,

$$a = \left(\frac{3LR}{4E^*}\right)^{\frac{1}{3}} \tag{2.1}$$

Where a is the contact radius, L is the normal load, R is the equivalent contact radius of the sphere, and E^* is the composite modulus, given as,

$$\frac{1}{E^*} = \left(\frac{1-v_1^2}{E_1}\right) + \left(\frac{1-v_2^2}{E_2}\right) \tag{2.2}$$

where v is the poisons ratio of the material, and E is the elastic modulus. Using the equation for contact radius, contact area is simply,

$$a = \pi \left(\frac{3LR}{4E^*}\right)^{\frac{2}{3}} \tag{2.3}$$

The mean and maximum contact pressures are,

$$\bar{P} = \frac{L}{\pi a^2} \tag{2.4}$$

$$P_{max} = \frac{3}{2}\bar{P} \tag{2.5}$$

Hertz did not include any adhesive forces in the original model for elastic contact, therefore it required modification to represent a more realistic system. This modification did not happen until almost 100 years after Hertz's original publication.

Adhesion is caused by capillary, electrostatic, van der Waals forces or other "chemical" forces [86]. The Dupre' adhesion equation presents a simple energy balance, where work of adhesion (W_a) is the difference between the sum of the two individual surface energies and the interface energy,

$$W_a = \gamma_1 + \gamma_2 - \gamma_{12} \tag{2.6}$$

Negative values of the work balance show that the energy of the interface was greater than the sum of the two surfaces, therefore it takes work to separate the surfaces (adhesion).

Numerous theories have been developed for calculating the pull-off force of two contacting spheres. In 1932 Bradley showed that for rigid spheres, the pull-off force followed the equation [87],

$$P_c = 2\pi R W_a \tag{2.7}$$

Where P_c is the pull-off force of the contact and R is the equivalent radius of the contact. This theory was modified by Johnson, Kendall, and Roberts to account for significant adhesion [85].The JKR theory states,

$$P_c = \frac{3}{2}\pi R W_a \qquad (2.8)$$

To reconcile these theories, Tabor created a parameter (the tabor parameter) that took into account the mechanical properties of contacting bodies, and suggested ranges of the *tabor parameter* for which each theory was valid [88]. The Bradley model describes very rigid, low adhesion bodies, whereas the JKR theory is more representative of soft, strongly adhering bodies, such as rubber on rubber. The contacting solids with mechanical properties in between the Bradley and JKR regimes are described by DMT [89], and Maguis [90] theories from more to less rigid, respectively. The DMT theory assumes there are no attractive forces outside of the contact, but assumes both bodies are elastic and follow Hertzian contact mechanics, which is where it differs from the Bradley model. For both DMT and Bradley, the pull off force is the same. In Figure 2.9, reproduced from [91], the different contact regimes are shown related to normalized adhesion force and normalized adhesion parameter.
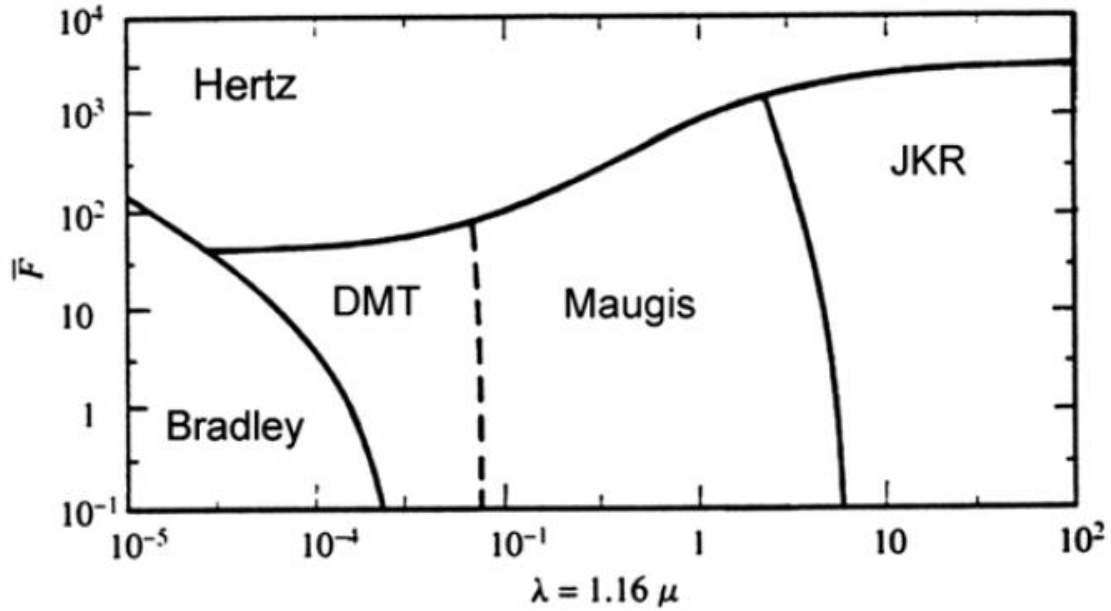
Figure 2.9. Map of the applicable adhesion theories given the normalized adhesion force ($\bar{F}$) versus

adhesion parameter (λ), reproduced from [91].

There is a significant difference between apparent and actual contact areas due to surface roughness. On the micro-scale, feature sizes and roughness can be of similar dimension and will therefore dictate the amount of area available for adhesion. The roughness ratio (Ξ) is used to describe a contact,

$$X = \frac{\sigma}{L} \tag{2.9}$$

Where σ is a dimension characteristic of the roughness and L is the dimension of the micro-scale feature, which in this case would be the radius of the microball bearing. The roughness ratio can then be utilized in determining the adhesion parameter,

$$\theta = \frac{E^* \sigma}{W_a} X^{\frac{1}{2}} \tag{2.10}$$

with lower values of θ meaning higher adhesion [92].

The calculations of contact area, pressure, and adhesive force are the primary mechanisms to connect observed tribological properties with fundamental calculations. The

47

relationship between observed friction torque and pressure/area is the most fundamental assumption of this work. Throughout the following chapters, the areas, loads, and contributions of adhesion are derived from the equations presented above.

2.7   Thermal Considerations

Temperature effects are often of importance when discussing friction, wear, and lubrication. Sliding action creates thermal energy (phonons) originating at the contact interface. The phenomenon of elastic hysteresis originates from mechanical energy lost to phonon generation within the solids in contact, also called internal friction. For the most part, ball and roller bearings are not subject to significant thermal issues due to low energy input in the system (light loads and low speeds) and the numerous thermal conduction paths available to take heat away from the contact interface [35]. For lubricated, macro-scale bearings, the temperature limit is determined by the breakdown of the lubrication either chemically or a reduction of effectiveness from a significant decrease in viscosity. The micro-scale bearings have not had an intense thermal analysis performed, although a number of factors point towards a minimal thermal effect on the bearing.

To accurately determine how much energy could be available to generate heat, a power balance of the system needs to be created. The equation below describes a simplified power balance for the microball bearing supported microturbines.

$$W_{in} = W_{out} + W_{loss} \tag{2.11}$$

Where W_{in} is the power provided by the turbine actuation flow,

$$W_{in} = \Delta P \dot{m} \tag{2.12}$$

ΔP is the pressure drop across the turbine and $\dot{m}$ is the mass flow rate. W_{out} is the mechanical power transferred to the rotor as,

$$W_{out} = \tau\omega \qquad (2.13)$$

With τ being the torque of the rotor and ω being the rotational speed. This leaves W_{loss} available for heat generation. In the interest of simplicity, W_{loss} will be assumed to be completely used to generate heat, which is a significant overestimate. Using performance data and friction torque relationship for a microturbine presented in [93], the power balance can be calculated (Figure 2.10).
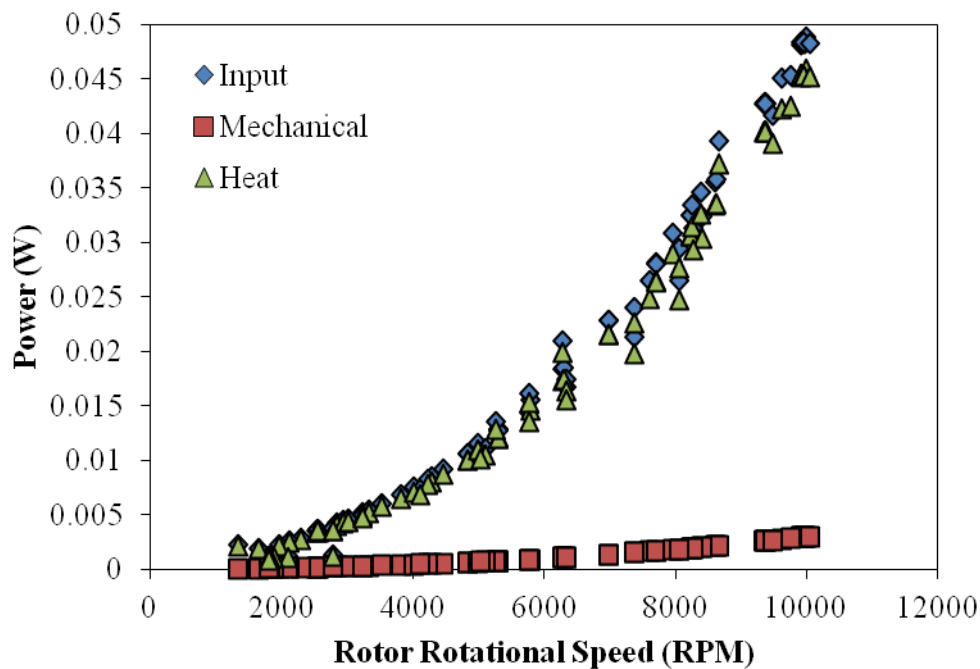
Figure 2.10. Power balance for microturbine supported on 285 µm diameter microball bearings. Power calculated from values presented in [46].

This shows that there is 45 mW available for heat generation at rotor rotational speeds of 10 krpm. There were 100 balls in this microturbine, therefore there were ideally 200 points of contact, leaving 225 µW per contact. The contact area between the ball and raceway for a turbine operating at 10 krpm is calculated from (2.3) to be 5.22 x10^{-12} m^2, giving a heat flux

49

of 480 MW/m^2. The ball resides within a single contact for approximately 100 μs, meaning 42.7 nJ are delivered during the time of contact.

The temperature change at the surface of the contact can be calculated once the input power and thermal resistances are known. The calculation of input power has been shown above. The transient nature of the system: rolling balls, air flow, etc… make for a very complicated thermal problem beyond the scope of this dissertation, therefore a number of assumptions are made to create a reasonable picture of the thermal effects within the bearing. The assumptions for this model include:

1. Contact resistance between the ball and raceway is neglected, making the ball the temperature of the contact

2. The balls provide continuous power to a given contact area

3. Heat travels the shortest path only (does not significantly heat up the rotor/stator)

4. Convective cooling exists, with film coefficients (h) of 25-200 W/m^{2}K (range for forced gas flow)

5. Heat conducted through the raceway can spread

Most of the assumptions err on the side of overestimating the temperature rise, therefore the results will give a maximum temperature at the contact. A schematic of the thermal model presented within the microball bearing raceway is presented in Figure 2.11.
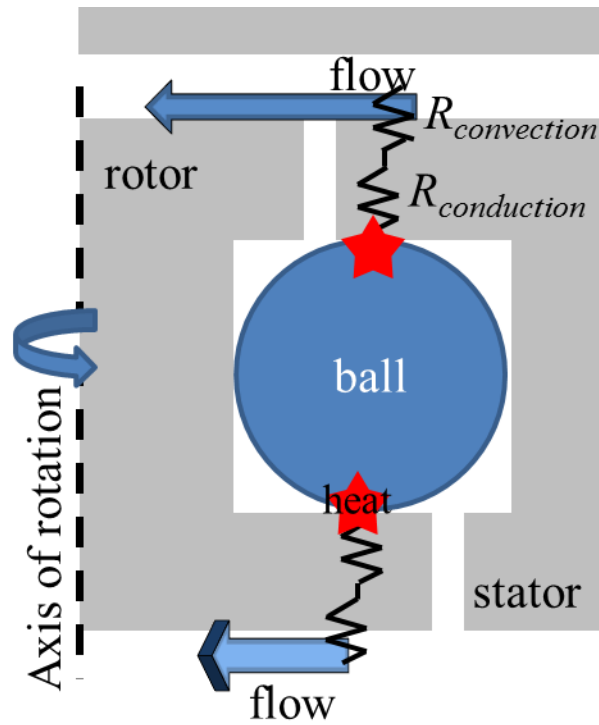
Figure 2.11. Schematic of the microball bearing system, showing heat source and pertinent resistances.

A model was found in literature that closely fit the assumptions presented above. The *isotropic disc with convective cooling* model was derived by Yovanovich was utilized to model the two heat flow paths in the microball bearing system [94]. Figure 2.12 shows the geometry used for the model.
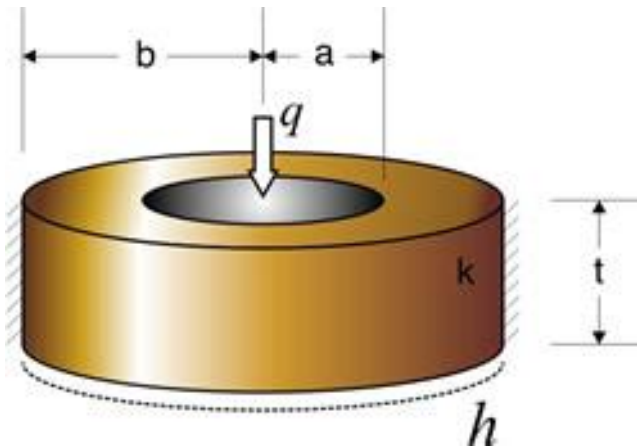
Figure 2.12. Isotropic disc with convective cooling from [94].

q was the input heat, calculated to be 225 µW in Figure 2.10, a is the contact radius of the ball, b was chosen to be 0.5 mm, and t is the approximate thickness of the wafer below the contact, 0.3 mm. Using the parameters above, the relationship between the film coefficient and the contact temperature was modeled in Figure 2.13
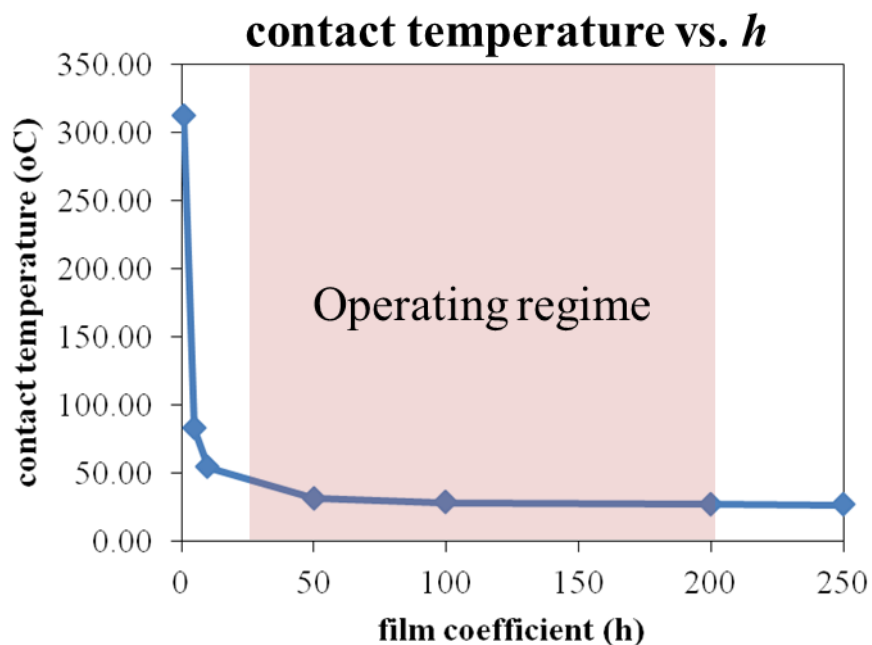
Figure 2.13. calculating the contact temperature over a range film coefficients

The contact temperature is significantly influenced by the quality of convection as shown in Figure 2.13. Forced convection ranges from $25<h<200$[95]. All devices tested within are air-

driven microturbines, therefore increased input power will always also increase the quality of convective cooling. This model shows that for the experiments performed within this dissertation, there is no significant temperature rise within the bearing, and therefore there is expected to be minimal thermal effects on the performance.

2.8   Conclusion

In this chapter a broad-reaching, general introduction to the microball bearing systems has been presented. The chapter therefore should serve as a reference to all following chapters regarding questions on design, fabrication, contact mechanics, and thermal issues. The factors dictating the design of the microball bearing systems, including fabrication limitations, load, and speed considerations have been discussed. Additionally, a detailed fabrication flow has been provided for the linear and rotary test devices, used in all sections but chapter 6. The contact mechanics of the system have been discussed, with a special treatment on the influence of adhesion. Finally, thermal issues have been considered for the microball bearing and were found to be minimal in the case of the air-driven, and therefore convectively-cooled, microturbine systems.

3. Friction

The focus of this chapter is on determining the sources of rolling friction within microfabricated systems. The relationship between friction and normal load has been studied for both linear and rotary devices using different methodologies. For the rotary devices, contact area was varied through the use of different ball bearing diameters as well as packing of balls in the raceway. The positive relationship found between contact area and observed friction support an adhesion-based friction hypothesis, which is further explored in the *Wear* and *Lubrication* sections.

3.1   Linear Device Experiments

The initial friction characterization was performed within linear raceways, utilizing microball bearings to provide a stable gap between a stator and slider undergoing reciprocating motion. This characterization was done as a stepping-stone towards the significantly more challenging rotary devices in both set-up and experimentation. The friction measured in this system would be analogous to a linear actuator, while the rotary system has more broad, high-performance applications. Friction in the microball bearings can be characterized with this set-up with different raceway geometries and low normal loads/speeds. A schematic of the experiment is shown in Figure 3.1
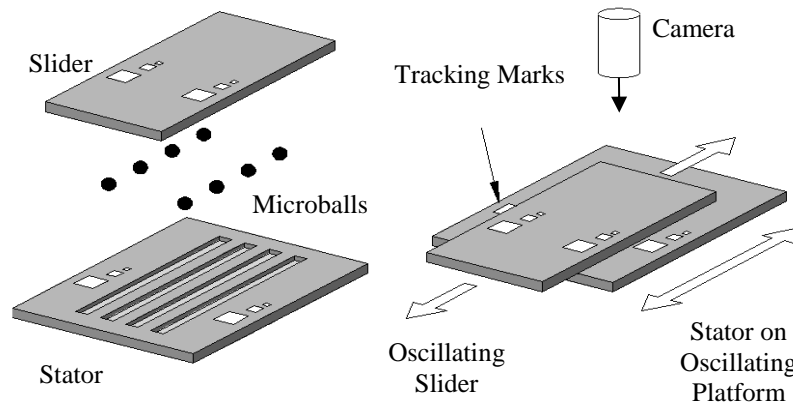
Figure 3.1. (left) assembly of linear tribology set-up. (right) schematic of experiment.

Silicon sliders and stators have been fabricated with deep etched rectangular trenches containing 285μm diameter steel microballs. The RMS roughness of the trenches and microballs are measured using optical profilometry to be less than 200nm and 25nm respectively. Figure 2.4 shows the cross-section of the device. The stator is rigidly attached to a linearly oscillating platform and friction forces are transmitted to the slider through the bearings. A non-contact vision-based data acquisition scheme is used to track the motion of the stator and slider individually. Figure 3.1 shows a stator/slider assembly along with a schematic of the vision-based testing approach. Eight microballs are housed in the trenches between the stator and slider. The stator is fixed to an oscillating platform driven by a computer controlled motor. The slider rests on top of the microballs with various weights placed on top to provide a normal force (not shown). The stator oscillates a traveling distance of 4mm at a motor speed of 150rpm. The slider and stator motions are captured with a camera at 120 frames per second. Position tracking software is used to monitor the displacement of etched tracking marks in both the stator and slider. The data is (a) smoothed to eliminate high frequency noise and (b) numerically differentiated to obtain velocity and acceleration profiles. The frictional force transmitted through the bearings is the product of the slider acceleration and load mass.

Figure 3.2 shows relative stator and slider position data acquired from the motion tracking software. The periodicity of position comes from the reciprocating motion of the stator, and the reduced amplitude of the slider is due to weak transmission of force from low friction from stator to slider. A frictionless slider would be motionless above the moving stator. These trajectories are numerically differentiated and the frictional force acting on the slider is calculated. Figure 3.3 shows the velocity dependent dynamic friction force acting on the slider under a 23.5mN normal force for bare silicon trenches. The steady state frictional force is calculated to be 47.1±3.4 μN for this loading.
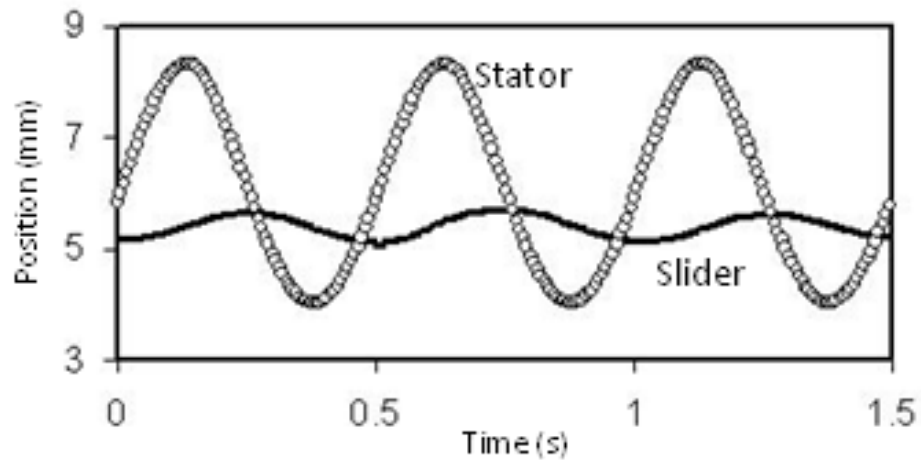
Figure 3.2. Stator and slider position date vs. time, from [96].
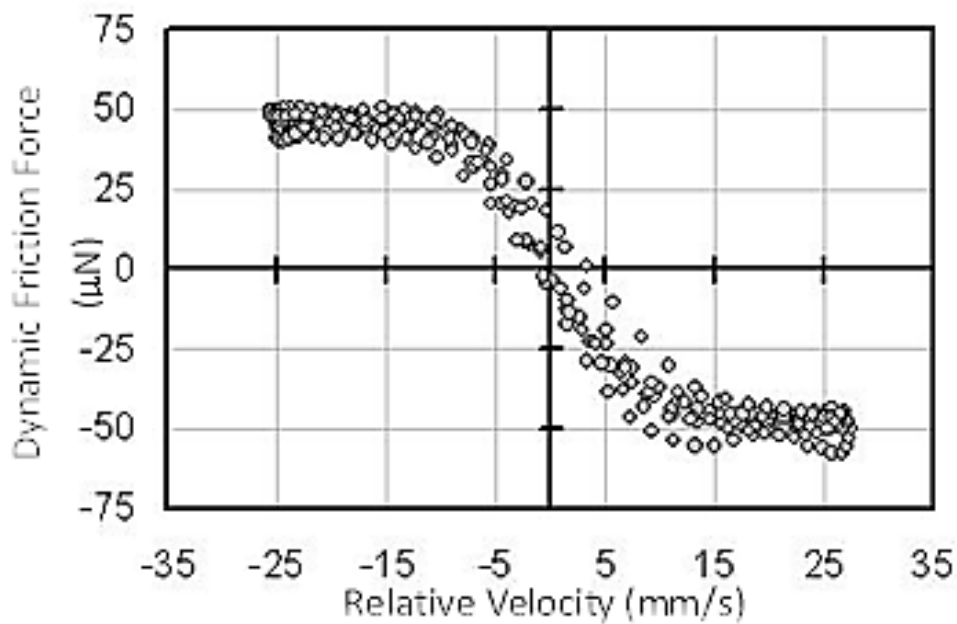
Figure 3.3. Friction force calculated from the second derivative of position, plotted versus relative

velocity, from [96]

3.1.1 Effect of Loading

The relationship between friction and normal load elucidates the fundamental

properties of the tribo-system. At large relative velocities the frictional force levels off

and remains fairly constant, as can be seen in Figure 3.3. This steady state frictional

force was measured for five loadings between 3 and 43 mN. Figure 3.4 shows the

empirically-derived dependence of rolling friction on normal force. This was the first time frictional force was suggested to increase as the normal force to the two-thirds power, similar to Hertzs' calculation for a sphere on a flat surface [84]; making the connection between friction and contact area. The authors (myself included) concluded that the main force of friction in these systems was interfacial slip, rather than adhesion because there was no significant wear on the raceways.
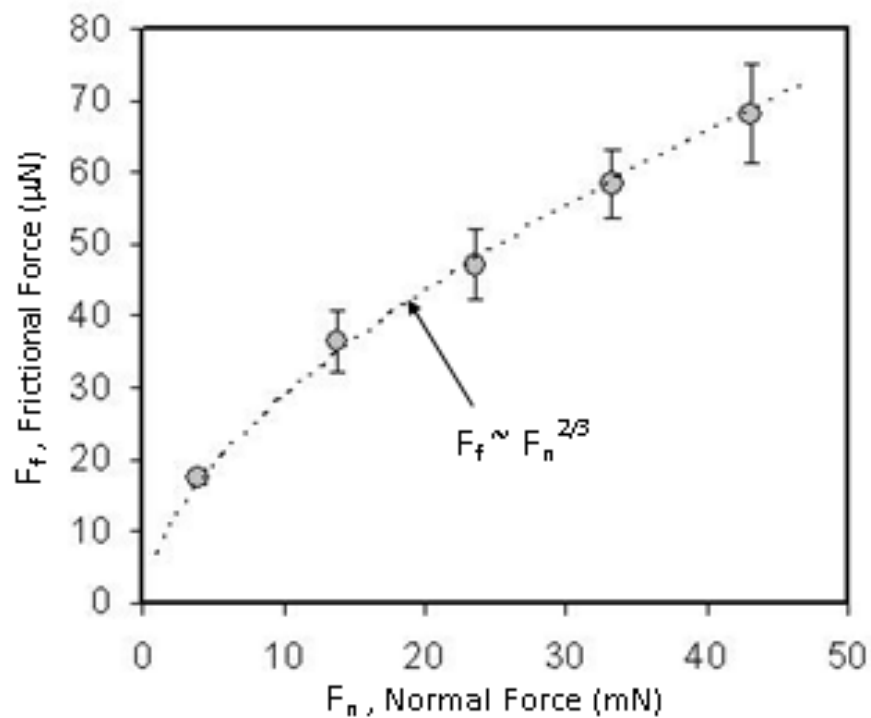
Figure 3.4. Friction force compared to rotor normal force, showing a $F_N^{2/3}$ dependence, suggesting a surface phenomenon, from [96].

To better understand the friction-load relationship, a parametric study was performed in KOH-etched linear devices (shown in Figure 2.4), where both the number of balls and load were varied, providing five unique ball loadings over nine experiments. The results of this study are shown in Figure 3.5. It can be seen that the lightest loading conditions (10mN:32balls) gave the least stable, or most velocity-dependent coefficient of friction, whereas the highest loaded sample (40mN:8 balls) had a speed-independent coefficient of

friction. This is expected to be due to the ratio of sliding to rolling motion, in which is load dependent. At high loads, rolling contact increases, and the coefficients of friction reach a consistent value of 0.004. These results were the first demonstrations of a linear speed dependence of friction torque, which was confirmed in the following rotary experiments.
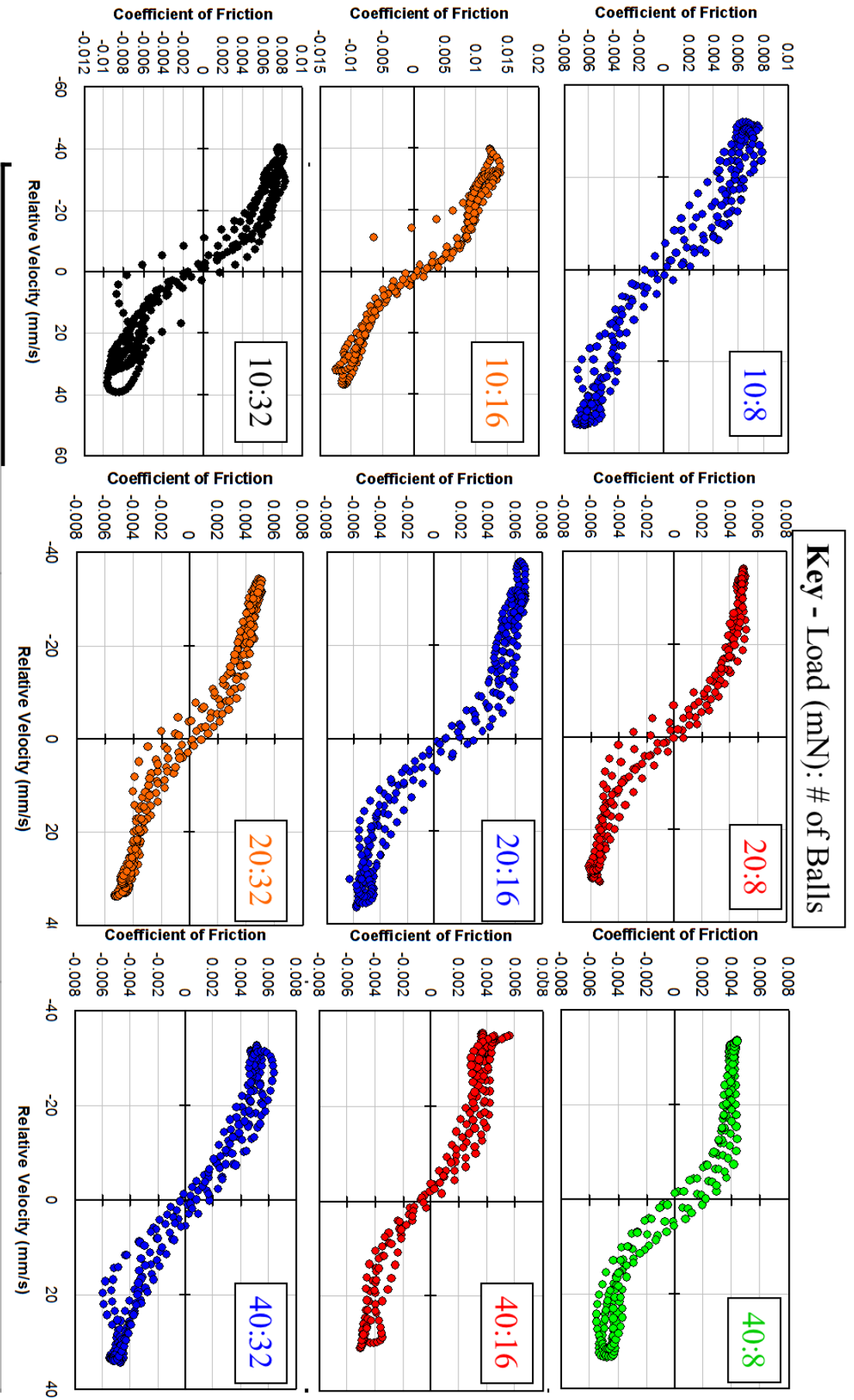
Figure 3.5. Parametric study of linear friction test devices. The normal load and number of balls used is shown inset each graph. Also, the color-coding signifies similar load/ball conditions. For example, 20 mN spread over 8 balls gives the same load/ball as 40 mN spread amongst 16 balls, assuming all balls are in contact.

60

3.2   Rotary Friction Experiments

Packaging of the MTD device allows for independent turbine and thrust flow while simultaneously measuring the speed via an optical displacement sensor (ODS) on equiradial tracking marks, turbine input pressure and flow rate, and thrust plenum pressure. The thrust plenum, created by an O-ring sealed cavity between the device and packaging, allows for variable normal loads to be acted on the rotor independent of speed. A photograph of the packaged device can be seen in Figure 3.6.
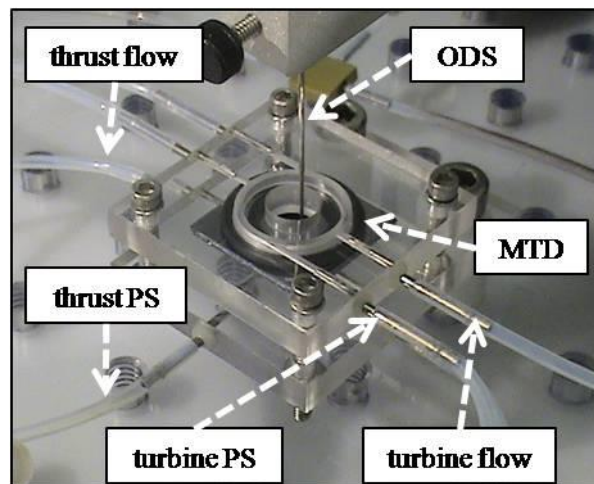
Figure 3.6. Photograph of packaged MTD under test. Turbine package layer includes turbine inlet flow ports, turbine pressure sensor ports (PS) and turbine exhaust port with inserted optical displacement sensor (ODS) for rotation speed measurement. Thrust-side packaging includes thrust flow ports and a thrust PS.

Spin-down deceleration tests are performed at normal loads from 5-100 mN. The upper-limit of normal load is due to the influence of normal load-inducing thrust flow, which is discussed in 3.2.1. Angular position during spin-down is measured via the optical displacement sensor. The angular position data is then fit to an exponential equation, with second derivative describing angular acceleration. The friction torque is then calculated by

the product of the angular acceleration and moment of inertia of the rotor, known from geometry.

To perform the test the thrust plenum pressure is set to provide normal load to the bearings, which will be a pre-set pressure during the actual spin-down. The independent turbine flow is then used to actuate the turbine impeller. Because of leakage through the journals and bearing races, the normal force on the bearing is increased during operation and is the sum of the thrust pressure and actuation pressure at the journal. After the turbine impeller has equilibrated to a steady rotational speed, the actuation flow is interrupted and the turbine is left to decelerate under only the load imparted by the thrust plenum flow.

Friction torque over the speed range of 500-10,000 rpm, which is termed dynamic friction torque (DFT), is obtained from the second derivative of a power law fit to the position data from the spin-down. The spin-down position data is first fit to the equation,

$$\theta = A(1 - e^{-Bt}) \tag{3.1}$$

Where θ is angular position, t is time, and A and B are fitting coefficients. Therefore angular acceleration ($\ddot{\theta}$) and velocity ($\dot{\theta}$) are related as,

$$\ddot{\theta} = -B\dot{\theta} \tag{3.2}$$

And torque is,

$$\tau = I\ddot{\theta} \tag{3.3}$$

where I is the mass moment of inertia for the rotor-ball system which for calculations is assumed to be a silicon disc with a torus of the same mass of the balls, and τ is friction torque. Therefore DFT is given as,

$$DFT = \frac{\tau}{\dot{\theta}} = I \cdot B \tag{3.4}$$

With the B value coming from the original curve fit.

3.2.1 Spin-Down Measurement Error

The error in the spin-down data primarily comes from three places: 1) the pressure transducer used to measure the backside pressure from which the normal load is calculated, 2) the position data obtained from the optical displacement sensor, and 3) the quality of the curve fit to the position data. The PX26-001DV pressure transducer from *Omega Engineering* used to measure the thrust pressure of the thrust cavity, from which normal force was calculated had a range of ±1psi, and is reported to have ±0.3% full scale repeatability. This equates to an error in calculated normal force of 1 mN. The optical displacement sensor operates at 20 kHz, so at 10,000 rpm with 12 etched tracking marks, five measurements are taken in each peak and valley. This equates to a maximum error of 5 milliradians in locating the tracking mark interface. Considering the device spins down through hundreds of radians, this error is negligible. The change from peak-to-valley sensing improves drastically as the device decelerates. This method assumes a constant deceleration between measurements of the edge of tracking marks. Additional error comes from the quality of the curve fit of the position data. The position data is fit to a power-law where the second derivative of the position data equals a constant times the first derivative, therefore implying a linear relationship between speed and friction, as observed in the linear test devices. This allows for speed to be taken into account in the value of friction torque. Curve fit qualities are $r^2 > 0.98$.

Additional error in the DFT measurements comes from the influence of the thrust plenum flow, used to impart normal load on the rotor. Thrust flow leaks through the bearings and exits through the rotor blades, imparting some torque opposing friction. An estimate of the added torque using conservation of momentum shows that at during the initial stages of the spin-down test, the thrust flow leak contributes 5% at 10,000 rpm and quickly drops off to 0.0001% at 1,000 rpm.

Finally, there is uncertainty from unintended variation amongst the geometries of the

microturbines. These variations include minor changes to raceway waviness, differences in surface roughness caused by micro-masking during the raceway etch steps, and variation in the raceway sidewall quality. To establish the uncertainty from geometrical differences, three microturbines of the *285, high* variation were tested at a set normal load and the standard deviation amongst observed friction was established. It was found that this variation is about 1×10^{-10} N·m/rpm.

3.3   Results and discussion

3.3.1   Turbine Performance

Turbine performance was measured for each of the MTD variations. For these tests, rotation speed was evaluated as a function of input power, the product of measured volumetric turbine flow and pressure at the turbine inlet. All MTDs are tested after a brief (<100,000 revolution) run-in wear period. The run-in period for the turbine is necessary for consistent operation of the device, as it provides some smoothing to the race surface asperities created in the DRIE etch and clears out any poorly released material from the journals. Figure 3.7 demonstrates the measured performance difference amongst the four tested turbine variations.
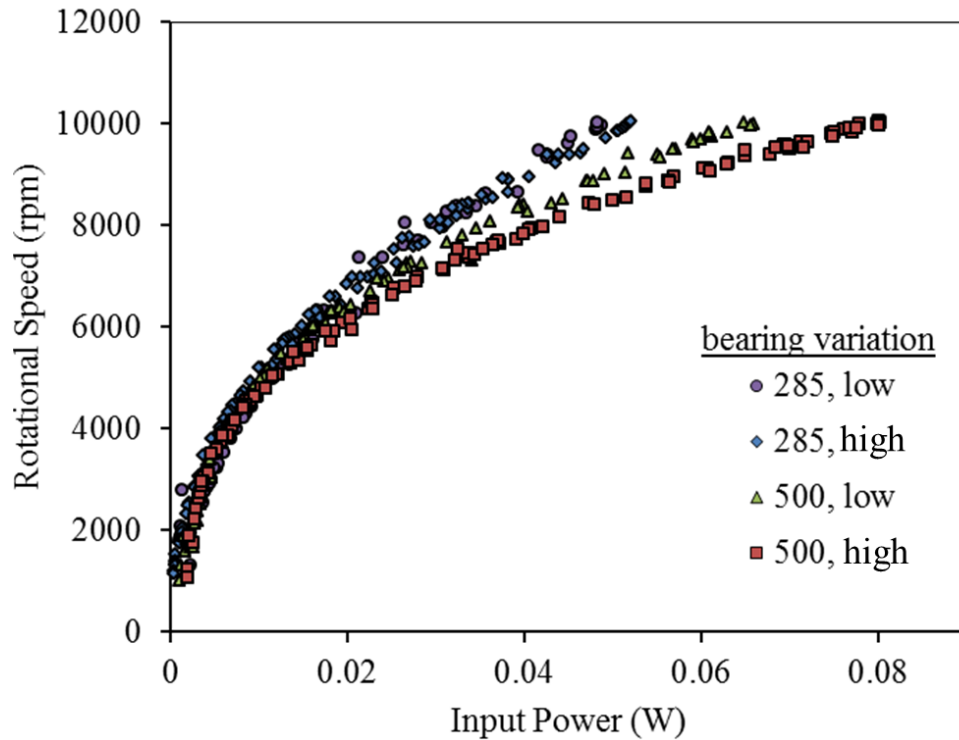
Figure 3.7. Turbine performance testing results of four tested bearing variations

The MTD performance is shown to improve from *500, high* to *low* ball loading, and then from *285 high* to *low* ball loading. The turbine blade geometry and packaging are identical amongst all devices; therefore the observed variation in performance is due to one or a combination of a number of factors. The number of ball-to-ball contacts could be a dominating source of friction, with *285, high* variation having the most. Contact pressure per ball is calculated from the geometry and measured load of each system, which would be the dominant factor in elastic hysteresis dominated systems. Additionally, each variation has a different rotational mass due to the size and number of balls. Finally, the total contact area can be calculated based on the load and geometry. The ranking of the previously mentioned factors can be found in Table 3-1.

Table 3-1 Analysis of bearing-based contributions to MTD performance

	285, low	285, high	500, low	500, high
Contact area/ball (μm²)	0.30	0.25	0.62	0.51
Total area (μm²)	22.9	25.1	28.0	30.8
Pressure/ball (MPa) @ 10mN	234	213	191	175
Ball-to-ball contact	75	100	45	60
Inertia (kg·m²)X10⁻¹⁰	1.8	2.4	5.8	7.7
Input Power@ 10krpm (W)	.048	.051	.065	.080

The measured differences in microturbine performance are likely due to a dependence on inertia or contact area. The system inertia and total contact area of the balls are the only contributions that scale similarly with the measured turbine performance. The hypothesis of ball-to-ball contact (summarized simply as the number of balls) dominating performance can be disproved because trend of most to least number of contacting elements has no correlation with measured friction, i.e., the *500, low* variation would be expected to require the lowest input power at 10 krpm with only 45 balls. A contact pressure dominant condition is also very unlikely because increasing contact pressures result in the increasing performance.

3.3.2 Dynamic Friction Torque

The relationship between DFT and normal load illuminates the fundamental processes responsible for rolling friction within the microfabricated ball bearing system. The DFT is the measure of friction torque in the system, obtained from spin-down friction testing, normalized by the range of spin-down speeds. This empirical model has evolved from a power-law [14] to a two component system [18], accounting for both load dependent and independent contributions to friction torque, and in this work, physical significance is given to the load-dependent contribution.

In previous work, a power-law relationship between DFT and normal load was

presented for a silicon high-speed microball bearing supported microturbine [6]. This power-law model assumes a linear relationship of rolling friction to rotational speed by normalizing the friction torque by the rotational velocity, a feature also observed in macro-scale bearing systems. Therefore the value of friction torque at 10 mN varied from 0.01125 N·m at 500 rpm to 0.1125 N·m at 5,000 rpm.

The power-law relationship has two major issues: it assumes friction goes to zero at zero normal load and there are no load-independent contributions to friction. A more complete description of the friction torque must include load dependent and independent contributions to DFT. To account for the load independent contributions to friction torque, we previously presented in [97] a linear relationship between DFT and normal load of the form,

$$DFT = aL + b \qquad (3.5)$$

where a is a constant representing a linear dependence of DFT on normal load, containing materials and geometric properties, L is the normal load and b is the load-independent component of DFT.

The value b is significant because it represents the theoretical minimum friction torque in an encapsulated microball bearing turbine for a load-balanced system. The load-independent contributions include viscous drag in the journal bearings (dimensioned in fig. 3), gyroscopic forces acting on the balls and centripetal acceleration, encouraging the balls to contact the raceway sidewalls as well as other minor contributions.

The viscous drag component of the friction torque follows eq. 3.6, Petroff's equation describing a viscous torque in a journal bearing,

$$M_{vis} = \frac{\eta A v r}{d} \qquad (3.6)$$

where η is the kinetic viscosity of the fluid, in this case nitrogen gas, A is the surface area of

concentric cylinders, r is the radius of the rotating element and d is the journal bearing gap. The friction torque M_{vis} arising from viscous drag for the 285 μm ball MTD design is calculated to be 1.27×10^{-7} N·m given a 35 μm gap, 310 μm total journal height and a 5 mm rotor radius at rotating 10,000 rpm. In addition to viscous drag within the journal, drag exists between the impeller blades and plumbing manifold, as well as inertial effects of the mass of air contained and spun between the blades. These effects have been numerically modeled and contribute about 1% to the measured friction torque due to the low relative velocities and areas, and larger gaps between parallel areas.

The second contribution to the speed dependence on DFT is the torque necessary to change the axis of rotation of the balls about the axis of rotation of the rotor. Torque due to this gyroscopic effect is calculated from equation 3 to be 5.7×10^{-10} N·m for the *285, high* MTD rotating at 10,000 rpm.

$$M_{gyroscopic} = I\omega_{rotor}\omega_{ball} \qquad (3.7)$$

where I is the moment of inertia of the ball, $\boldsymbol{\omega_{rotor}}$ is the angular velocity of the rotor, and $\boldsymbol{\omega_{ball}}$ is the angular velocity of the ball.

A measured b value of around 1×10^{-6} N·m is obtained from spin-down testing for 10,000 rpm all devices. The calculated contributions of viscous drag and gyroscopic torque account for a maximum of 19% of the measured torque at this speed. The remaining measured friction torque is comprised of sliding friction due to the centripetal forces acting on the balls and other velocity dependent torques. The contribution to friction torque from centripetal forces is assumed to have a large contribution to the b value, but cannot be addressed within the current experiment and will be the focus of subsequent studies. Possible future studies with tailored sidewall roughness could help elucidate this effect.

Multiple rounds of spin-down testing was performed from 5 to100 mN for all bearing variations on new devices, after an initial 100 krev. run-in. Normal loads were tested high-to-

low and low-to-high to eliminate any artifacts arising from the testing procedure. Figure 3.8

presents a series of spin-down tests for the tested bearing variations.
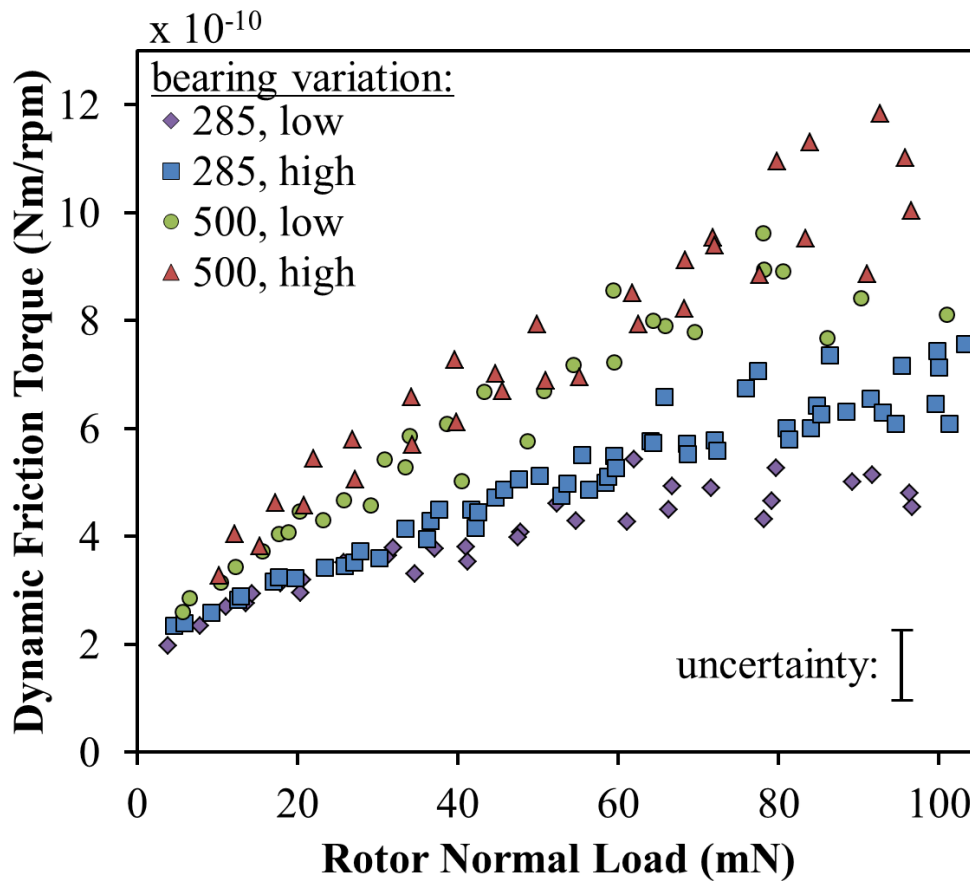
Figure 3.8. The results of spin-down friction testing of four bearing variations.

The relationship between DFT and normal load alludes to the major contributions to

friction. There are two primary friction/normal load relationships described in literature for

rolling friction and a third proposed herein. The first and most common relationship is

referred to as Amonton's law and simply states that friction is linear with normal load. The

second relationship between friction and normal load is derived from the elastic hysteresis of

a sphere contacting an elastic half space was described by Tabor, *et al.* and follows the

relationship $Load^{4/3}$ [32]. The hysteresis dominated rolling friction is widely accepted for

macro-scale ball bearing systems [35]. The final relationship is based on adhesion between

the ball and the raceway, and is therefore dictated by the contact area. The third, surface

adhesion dominated, relationship is from Hertz's derived $Load^{2/3}$ geometrical dependence on

contact area of a sphere contacting a flat plane.

A curve fit analysis is performed for the experimental dynamic friction torque data for the four bearing variations. Three equations are used for the fitting, based on the previously described friction/normal load relationships and including the load-independent constant described above. The equations are,

Linear:
$$DFT = aL + b \tag{3.8}$$

Surface:
$$DFT = aL^{\frac{2}{3}} + b \tag{3.9}$$

Volume:
$$DFT = aL^{\frac{4}{3}} + b \tag{3.10}$$

Curve fits of empirical data in figure 6 based on equations (3.8) are described in Table 3-2.

Table 3-2 Regression analysis of experimental DFT data

285 μm Diameter Balls   500 μm Diameter Balls

	a	b	r^2	a	b	r^2	curve fit
Low Loading	0.29	2.54	0.83	0.07	2.86	0.89	linear
	0.16	1.96	0.87	0.37	1.54	0.91	surface
	0.01	2.84	0.77	0.01	3.56	0.84	volume
High Loading	0.05	2.41	0.92	0.08	3.11	0.91	linear
	0.26	1.43	0.93	0.45	1.38	0.92	surface
	0.01	2.94	0.90	0.02	4.00	0.90	volume

The quality of the fit is used to determine the most likely influence on friction torque, whether it is surface-based, volumetric-based, or a combination of multiple parameters averaging to a linear relationship, as is the case with macro-scale sliding. In all cases the

Hertzian contact (surface) based fit has the highest r^2 value.

Given the empirically derived proportionality of load to contact area and the measured relationship between normal load and friction torque, it can be then inferred that friction torque scales linearly with contact area. This contrast to macro-scale bearings can be explained by the increased surface-to-volume ratio of micro-scale components. The factors contributing to the specific constant "*a*" are not well understood, but it is assumed that properties described by *a* are affected by run-in smoothing of the raceway features and the level of wear within the raceways. The values of *b* from the surface fit range from 0.70-1.96 X 10^{-10} N·m/rpm, representing the minimum possible friction torque within the turbine and an order of magnitude higher than the air-only bearing measured in [98]

The total contact area of each bearing variation over the range of tested normal loads is presented in Figure 3.9.
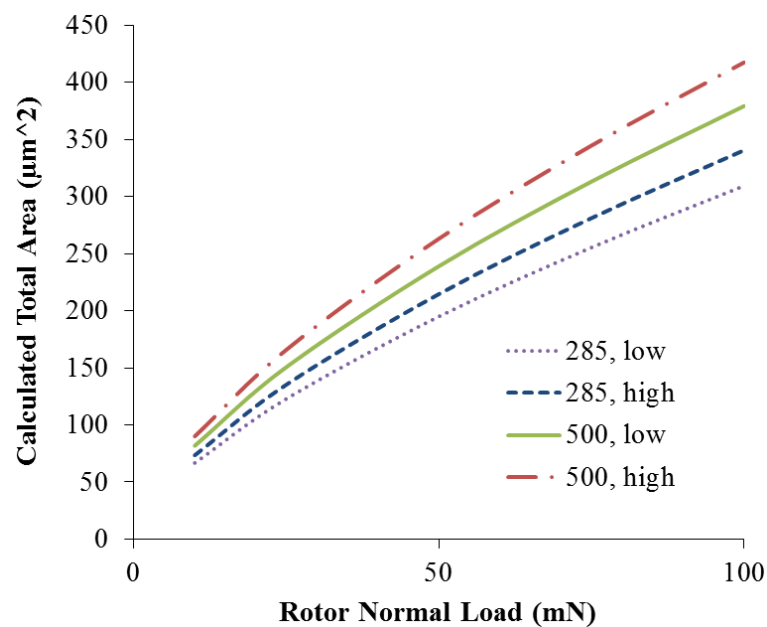
Figure 3.9. Contact area of bearing variations based on Hertzian contact mechanics and fabricated geometries.

The spin-down testing closely resembles the contact area relationship, as expected, which can

be explained by the friction torque dependence on adhesion, and the adhesion dependence on contact area. The contact area calculation assumes perfectly planar raceways, although in actuality there is a measured ±1 μm deviation in raceway depth for all bearing variations. The implication of the raceway waviness is that the not all of the balls are supporting load or providing contact for the surface adhesion dominated wear mechanism. A better understanding of the surface energy in each adhesive contact would allude to the number of balls contributing to friction for a given load range. In this work it is assumed that the variation in depth causes a similar percentage of balls to be in contact for all tested bearing variations.

Additionally, the spin-down friction measurements mimic the trend observed in the turbine performance testing in Figure 3.7, with the larger diameter and more numerous microballs exhibiting higher friction. The performance testing presented in Figure 3.7 was unable to determine whether the inertia or contact area was more significant regarding performance. Spin-down deceleration tests (Figure 3.8), in contrast, normalize each spin-down measurement by the inertia of the bearing variation, and is therefore independent of inertial effects. This result suggests that the total contact area has a significant contribution to system friction.

The final contribution to DFT is the sliding friction resulting from ball contact with the raceway sidewalls due to the centripetal forces arising from the rotating elements and is the least understood. The magnitude of the centripetal force is given,

$$F_c = m_{ball} r_m \omega^2 \tag{3.11}$$

Where F_c is the centripetal force acting per ball, m_{ball} is the mass of a single ball, and ω is the angular velocity of the system. At 10,000 rpm the centripetal force is calculated to be 130 μN/ball. It should be noted that while the magnitude of the centripetal force can be

calculated, it is difficult to estimate the effect on system friction. If centripetally induced forces dominated friction, then the observed friction torque would not have a linear speed dependence, from eq. (3.7). Because this force acts orthogonally to the direction of motion, it could interrupt rolling motion by forcing the ball to make temporary sliding contact with the sidewall. In the realistic bearing, as previously discussed, geometric discrepancies in the raceway depth cause the rotor normal load to be distributed only to the highest contact balls, leaving unloaded balls free to contact the sidewalls. At high rotational speeds and low normal loads, the centripetal force will exceed the friction force imparted by the normal load and the balls will preferentially roll along the outer sidewall as opposed to the thrust surfaces. All of the testing performed herein is below the critical thrust-to-radial shift speed to minimize the factors influencing friction. The thrust-to-radial force transition for the *285, high* variation is graphically presented in Figure 3.10, providing an operating guideline to assure the MTD is operating as a thrust bearing.
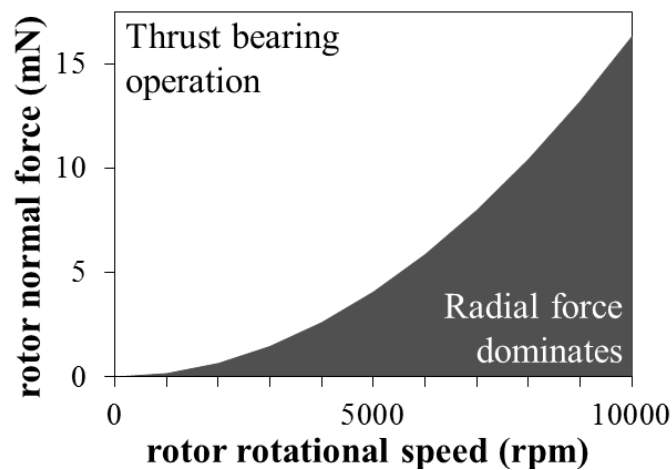
Figure 3.10. Operation regimes for a range of speeds and normal loads of the tested MTD, designed for thrust bearing operation.

The transition towards increased sidewall contact from centripetal load has been verified experimentally through on-chip vibration-based diagnostic testing presented in

chapter 7. In the ideal case this effect disappears above 15 mN normal loads and its relationship to load and speed is not well understood. Etching grooved raceways similar to macro-scale bearings will remove this effect, but the technology is not currently available to obtain uniform, low roughness, deep groove raceways in microfabrication schemes.

3.3.3 Coated Raceways

Microturbine raceways were coated initially as a mechanism to reduce the deformation of the raceway by increasing the hardness. Spin-down friction testing was used in conjunction with the turbine performance testing to compare the TiN and bare-Si raceway friction. The spin-down test procedure is described in [6]. TiN raceways were tested to the same rotor load/revolution metric as a bare silicon turbine (10 mN/2M rev.). The initial values of dynamic friction torque (DFT) were similar for TiN and Si raceways, as seen in Figure 3.11a.
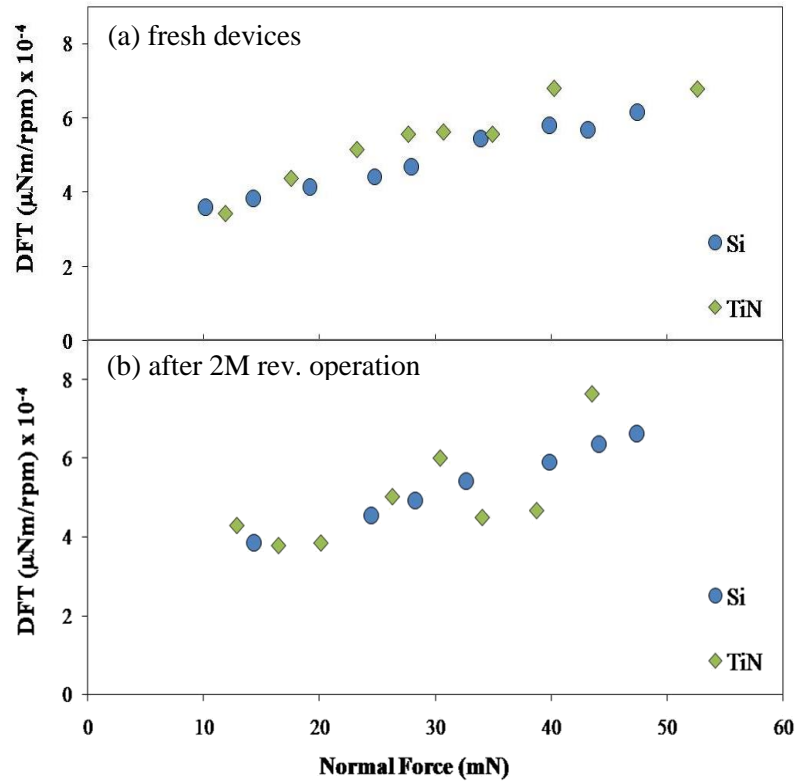
Figure 3.11. (a) DFT values for bare Si and TiN coated systems. Both systems follow the linear relationship between DFT and normal load. (b) DFT values for raceways after 2M revolutions of run-in. Si raceways remain consistent, while the TiN coated systems begin to exhibit erratic behavior. Figure reproduced from [97].

Despite having a higher hardness using TiN, there was no observed reduction in friction in the initial test. This result further suggests the enhanced influence of surface properties over volumetric properties.

Following the initial test, the TiN coated and Si MTD were run at 10mN rotor normal loads for 1M revolutions and then re-tested. This process was repeated twice. Figure 3.11b compares the DFT values of the Si and TiN coated raceways after 2M revolutions wear. DFT testing was not performed beyond 2M revolutions so that the raceways could be inspected, a destructive process for the microturbine. It was observed that the Si raceway maintains consistent performance while the TiN coated raceway becomes increasingly more erratic.

3.4   Conclusion

This work determines the influence of surface effects on the tribological phenomena of microfabricated ball bearing systems. Four microturbines were fabricated and tested to specifically address the effect of contact area between the balls and the raceway as a mechanism to determine the influence of adhesion. A new model for dynamic friction torque was presented that coincides with the relationship between load and contact area as described by Hertzian contact mechanics. The relationship between contact area and friction proposed herein is unique to micro-scale rolling contact and will be supported by observed wear mechanisms in the following chapter. Load independent contributions to friction were explored and a minimum DFT value of 2.55×10^{-10} N·m /rpm is hypothesized for a zero normal load (thrust-balanced) microturbine. Through modifications of bearing fabrication methods and geometries, the performance of a silicon raceway/steel ball system has allowed for the discovery of the Hertzian contact area based friction/load relationship and the exploration of adhesive ball wear. This advancement in understanding of the mechanism of micro-scale friction and wear will lay the groundwork for future high performance rotary systems.

The contact-area based friction relationship has implications for future micro-ball bearing systems. Conventional ball bearing knowledge suggests that using larger ball diameters will result in lower values of friction, whereas these findings argue the opposite result. Smaller balls should be used to lower friction because of their reduced contact area with the raceway. The lower limit on ball diameter will be determined by two factors: contact pressure and manufacturability. As the ball diameter reduces, so does contact area, which means there is an increase in contact pressure for a given normal load. If this contact pressure exceeds the strength of the raceway, it will fracture. There is also a lower limit of

manufacturability currently with ball bearings. Grade 10 balls can only be made with diameters of around 200 μm minimum. The upcoming chapter on lubrication (chapter 6) will discuss the alternative approach to reducing contact area, which is reducing contact energy.

4. Wear

This chapter is focused on exploring the wear mechanisms dictating the performance of the microfabricated ball bearing systems. Worn raceways are dissected and the wear mechanisms are studied using Raman Spectroscopy and Electron Dispersive X-ray spectroscopy (EDS) in conjunction with Scanning Electron Microscopy (SEM), and optical profilometry. These tests and analysis methods were carried out on bare silicon raceways, as well as raceways coated with SiC, UNCD, and TiN hard-thin films. Certain load and material combinations will result in a specific wear mechanism. An understanding the different wear mechanisms will allow for engineering systems designed for minimum wear and maximum lifetimes.

4.1   Linear Wear Studies

A silicon stator-slider combination with deep reactive ion-etched raceways and stainless steel microballs was used for accelerated wear testing (described in chapter 2). The silicon stators and sliders were tested bare and coated with silicon carbide and ultrananocrystalline diamond. Accelerated wear testing was performed to determine the wear regimes amongst the various coatings and load ranges.

4.1.1   Experiment

Accelerated wear experiments took place through reciprocating the slider beneath the stator under load. The slider chip was affixed to a reciprocating stage, supported on pillow block bearings, actuated via a linkage with an electrostatically-driven fly wheel. Microball bearings (diameter =285 µm) are place in the etched slider raceways, and then the stator is placed atop the bearings. The stator chip is held static under load while the slider is actuated

to 4 mm travel at speeds up to 6.7 mm/s. Loads of 5 mN, 20 mN and 50 mN were tested. An

image of the test setup is shown below in Figure 4.1.
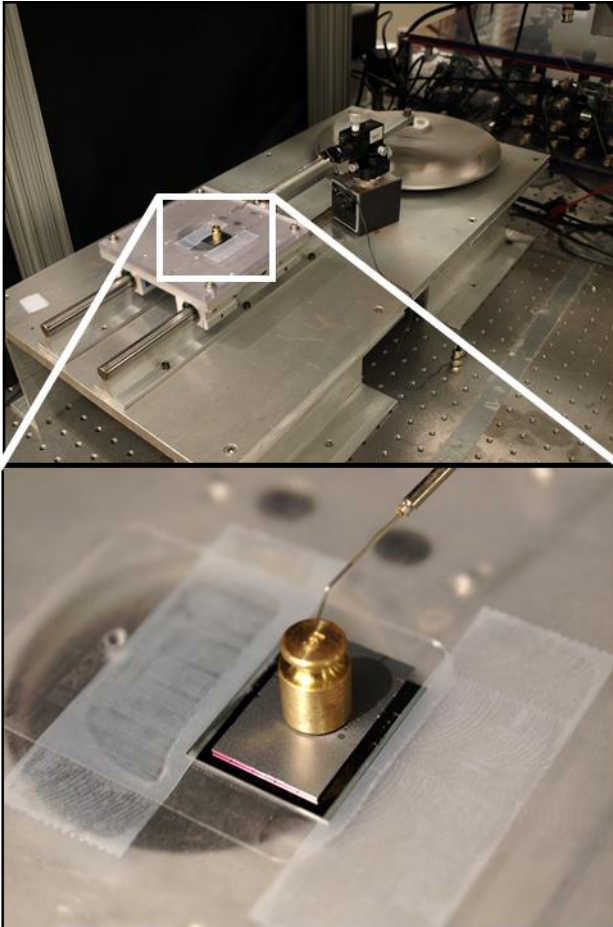
Figure 4.1. experimental set-up for the accelerated linear wear testing. (Top) image of electrostatically

actuated reciprocating motion table. (bottom) zoom in of device, under 5g load held in place with a

probe.

Testing was performed incrementally in 10k cycle steps. After each step, the device

was disassembled, and the stator and slider raceway topography was measured using optical

profilometry (*Veeco WYKO NT 1100*). Measurements were taken along the length of the

worn areas, and the average increase in surface area was obtained by integrating the

measured pixel height over the area of the ball contact path.

4.1.2 Results

The effects of load and the performance of hard-film coated devices were explored. Load testing was performed on bare silicon samples only. The increase in surface area for a range of loads and cycles on bare silicon is presented in Figure 4.2 .
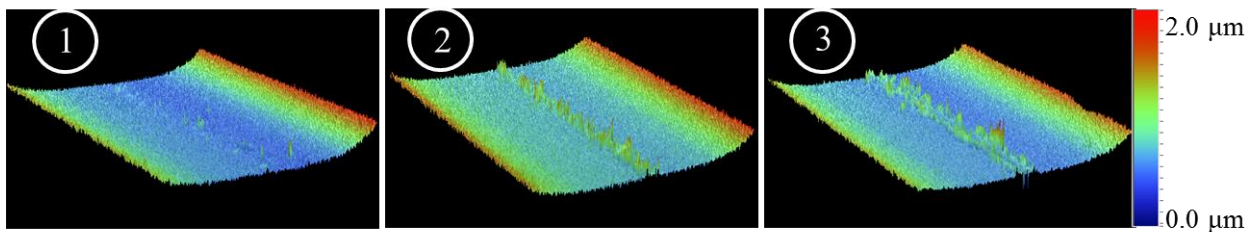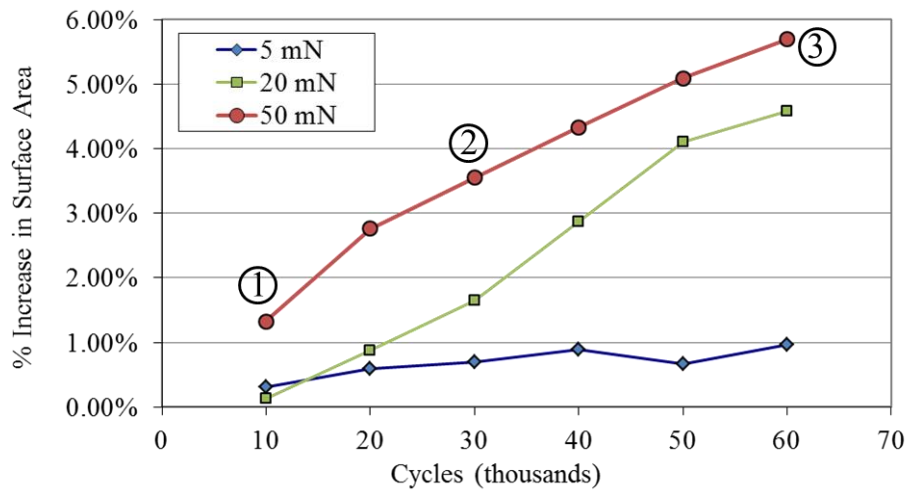
Figure 4.2. Percent increase in surface area of three devices operated at different loads, through 60k cycles. (*1-3*) optical profiles of selected data points.

The adhesion of material to the raceway was the observed wear mechanism in the bare silicon test device. A stabilization of the wear rate was not observed for the higher load systems, suggesting the adhesive mechanism has load dependence. The enhanced rate due to load is due to two aspects: the increased area of contact that is imposed by higher loads and the increased energy provided for adhesion from increased contact pressure.

In the long term, the adhesive wear rate is expected to reach a virtual equilibrium. At equilibrium, the contact path in the raceway has been coated with ball material. The wear,

however, does not arrest, it takes place via a ball material transfer. The ball adheres to ball material on the raceway, and fractures in three mechanisms: through the newly formed contact, through the ball (depositing on the raceway), or through the adhered wear track (depositing on the ball). The three mechanisms are equally probable, resulting in a net-zero *observed* wear rate.

Linear accelerated wear tests were also performed on thin film coated devices. UNCD and a-SiC films were deposited to a thickness of 500 nm on the etched substrate. The two films were chosen because they have significantly different mechanical properties, with UNCD being significantly harder and stiffer than the Si substrate, and a-SiC being softer and more elastic. Their mechanical properties compared to silicon are presented in Table 4-1 below.

Table 4-1 mechanical properties of linear wear study materials

	Si	a-SiC	UNCD
Elastic Modulus (GPa)	175	96-161	967
Hardness (GPa)	12.5	10-20	97

The devices were placed under 20 mN normal load and reciprocated as described above. Figure 4.3 shows the percent increase in surface area amongst the three tested surfaces.
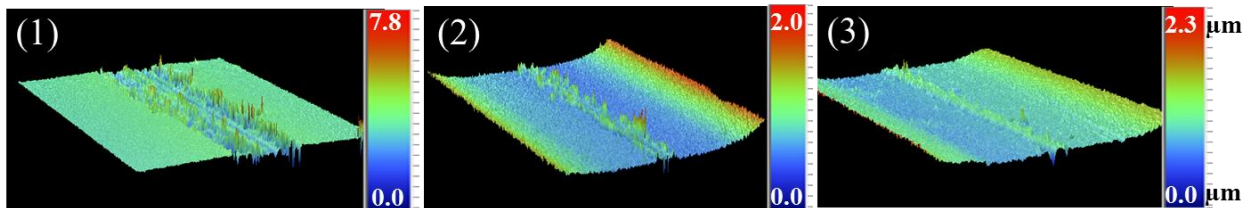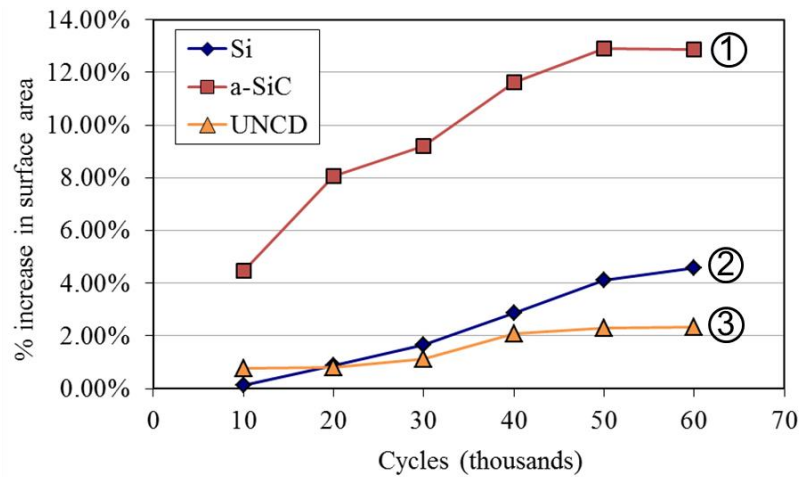
Figure 4.3. Percent increase in surface area of three devices operated with different surfaces, through 60k cycles. (*1-3*) optical profiles of selected data points from graph.

a-SiC showed the most significant wear amongst the tested surfaces. The film was fractured in two parallel paths along the length of the contact path, which correlate with the areas of maximum shear stress induced by the ball contact (Figure 4.4(top)). Eventually this fracture mechanism propagated beneath the contact zone and completely delaminated the film (Figure 4.4(bottom)). It is assumed that once the contact zone was completely free of a-SiC film, then it would behave like the bare silicon sample. UNCD films remained intact for the duration of testing, with the adhesion of ball material being the only observed wear regime. The adhesion was slightly less than for silicon, which is expected to be a product of having reduced contact area from the stiffer films.
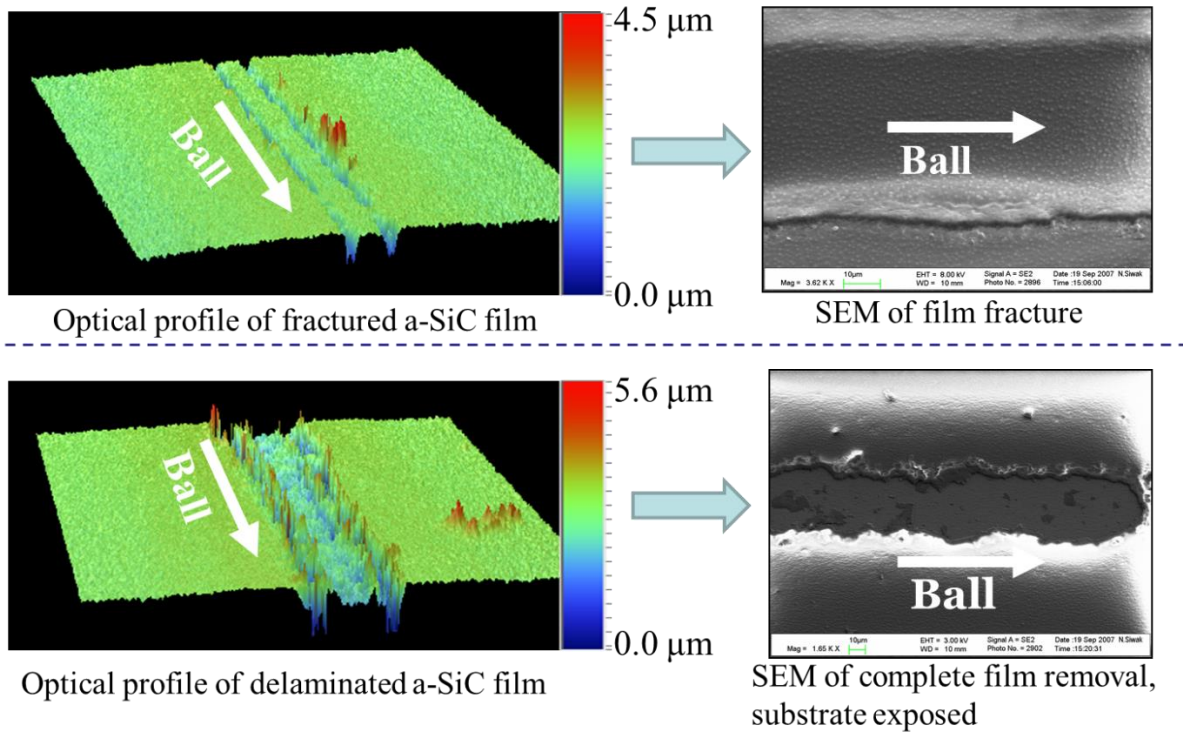
Figure 4.4. (top) optical profile and SEM image of film fracture, (bottom) optical profile and SEM image of completely removed film, exposing the substrate.

4.2   Rotary device design and fabrication

Seven microturbines were used to determine the wear mechanisms within the microfabricated ball bearing systems. Five turbines with bare silicon raceways; two turbines used hard film coatings. The testing conditions and ultimate failure mechanisms are summarized in Table 4-2

Table 4-2 Summary of experimental conditions of accelerated wear test silicon

raceways

Device	Rotor Load	Testing Lifetime	Stress/ball (MPa)	Coating	Failure Mechanism
D1	10 mN	2 Mrev.	142	n/a	inspection
D2	10 mN	2 Mrev.	140	TiN	spalling
D3	10 mN	2 Krev.	129	SiC	Coating fracture
D4	50 mN	3 Mrev.	242	n/a	Fabrication Defect
D5	100 mN	205 Mrev.	306	n/a	n/a
D6	200 mN	20 Mrev.	385	n/a	inspection
D7	400 mN	400 Krev.	485	n/a	Raceway fracture

Wear of the silicon raceway was induced through a series of accelerated wear tests. To perform these tests, the compressed gas is used to impart 10 to 400 mN normal loads on the rotor while the device is actuated at speeds of 6,000-12,000 rpm by gas flow through turbine actuation structures. These speeds are chosen for wear testing to minimize the effect of centripetal acceleration of the balls, addressing the effect of load dependence on the wear rate of the turbines ideally operating as thrust bearings (ball axis of rotation perpendicular to rotor axis of rotation). After successive operation cycles, the microturbine performance is evaluated by plotting speed vs. input power, as described in the section below (Figure 4.5). Devices were disassembled at different intervals and the wear was measured geometrically with optical profilometry and visually with SEM and optical microscopy.

4.3 Microturbine Performance

Microturbine performance is used as a way to measure the general efficiency of the turbine which is directly related to the condition of the raceways. Etched silicon races, coated with TiN or SiC thin films and raceways left uncoated were evaluated. UNCD films were omitted from this study due to difficulty obtaining well adhered films. The two mechanical properties of interest, hardness and stiffness, of the tested films was tested using nanoindentation and is reported in Table 4-3.

Table 4-3 Mechanical Properties of Thin-film/Si systems probed via nanoindentation.

	Bare Si	250nm TiN	250nm SiC
Stiffness (GPa)	169	155.9	127.1
Hardness (GPa)	13.4	15.7	17.7

Reduced mechanical deformation from increased hardness could reduce friction and wear by two mechanisms: reducing the amount of energy lost to plastic deformation and reducing area of contact between the ball and raceway. Initial characterization of the coated raceways within a MTD was done using the speed versus input power performance testing method described above. During this test, the rotor is imparted a normal force of up to 12mN from the pressurization of the thrust cavity due to turbine pressure leaking through the bearings. This relatively low-load proved enough to start rapidly wearing the SiC film while the TiN coated and bare Si raceways performed nearly identically. The results from the initial performance characterization, including the wearing of the SiC thin film, can be indirectly observed in Figure 4.5 by the low speeds obtained at high input power. The accelerated wear of the silicon carbide film will be discussed in the following section.
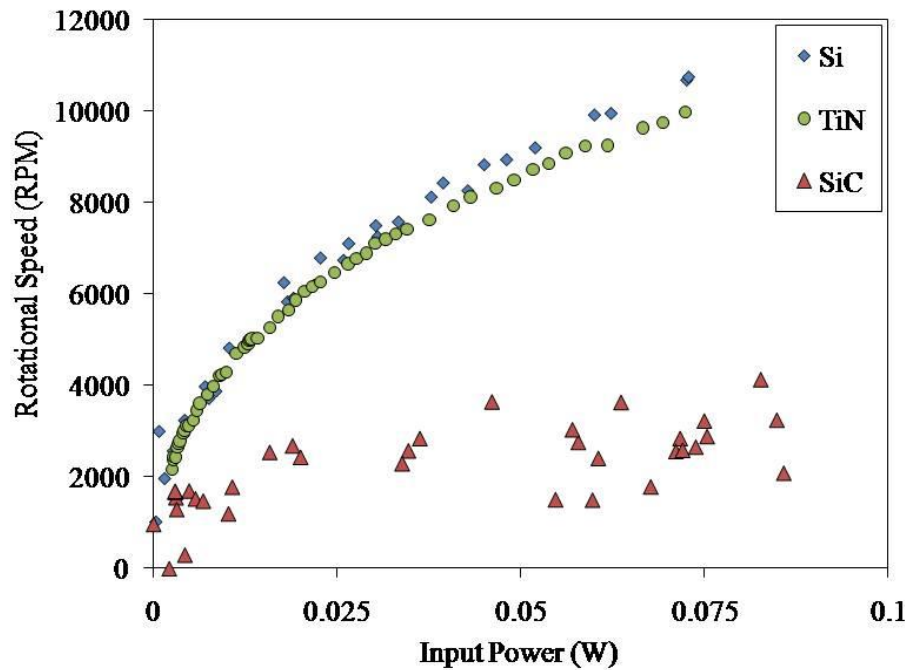
Figure 4.5. Performance curves taken from virgin raceways coated with SiC, TiN thin-films or left bare. SiC films erratic behavior is due to significant wear.

The wearing of the SiC thin films is also apparent in a time-resolved plot of turbine performance (Figure 4.6). Input pressure is set to an initial value of 0.12 PSIG, which should result in a constant speed for the device. The SiC coated sample shows a bi-stable behavior, operating at either 2,000 rpm or 6,000 rpm, with a back-and-forth, gradual transition between the two. The rotor stabilizes at 6,000 rpm once the raceway has been completely worn, although this level does not represent a bare silicon turbine, which has a pressure drop of about 0.06 PSI at 6,000 rpm.
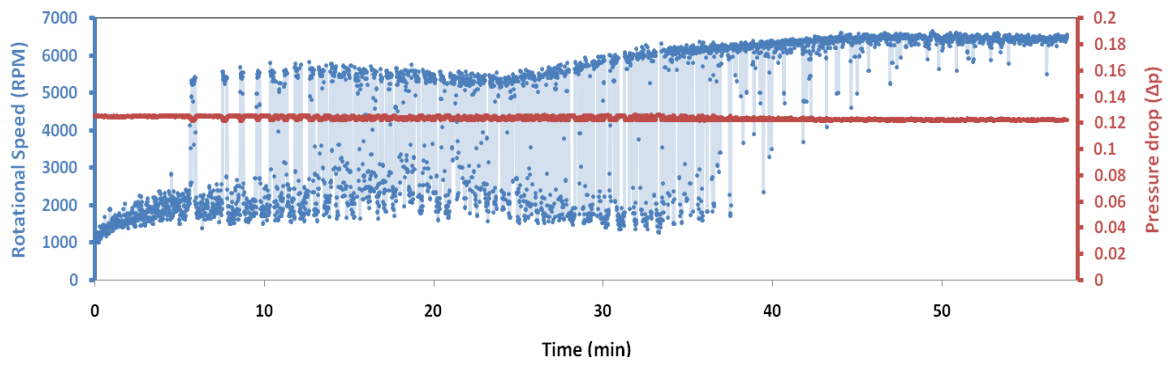
Figure 4.6. SiC coated microturbine performance over 1 hour of testing at constant input pressue.

A performance assessment of the bare silicon turbine is performed with and without cleaning beyond 55 million revolutions (M rev.) to better understand the long-term wear mechanisms. Figure 4.7 highlights two aspects of the long-term turbine performance. The MTD performance is measured initially, and then at progressive levels of wear up to 205M rev., measured before and after cleaning. The inset graph compares the performance before and after cleaning to the initial performance for a representative level of wear. In between performance characterizations, the device is run at 100 mN normal load to accelerate the wear process.
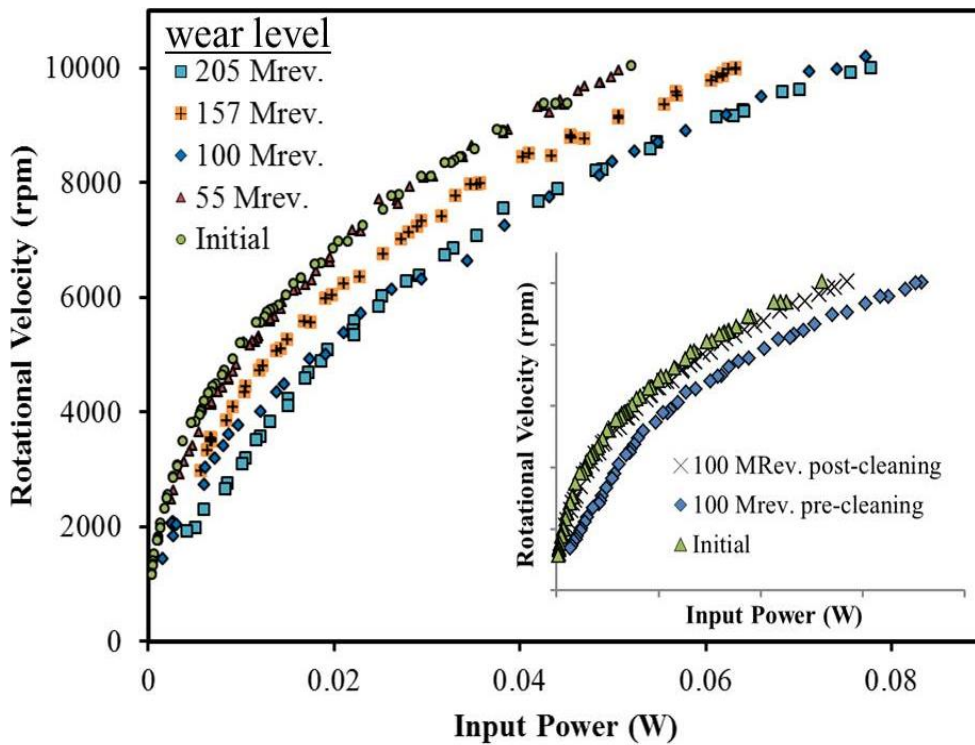
Figure 4.7. Performance curves for a single MTD through progressive levels of wear. (Inset) Peformance characterization of MTD before and after cleaning at 100M rev. wear level, compared to intial values.

The MTD performance is shown to degrade between the 55M rev. test and 205M rev. test in that it takes up to 75% more power to reach a given turbine speed. The observed performance degradation is most likely due to the random ejection and build-up of sidewall material from ball-sidewall impacts and ball material. Figure 4.7 (inset) shows the performance curve at the 100M Rev. level directly after testing (pre-cleaning) and after cleaning procedure, revealing that the turbine performance improves after cleaning. Figure 4.8 compares the sidewalls of virgin and tested devices after 2M rev.
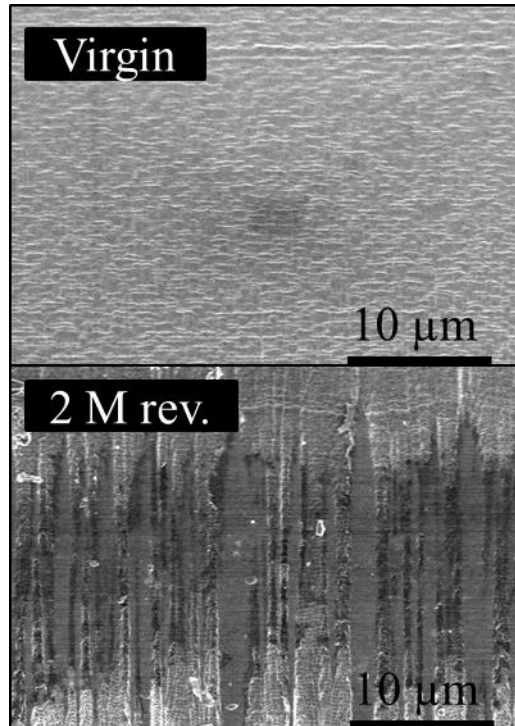
Figure 4.8. Scanning electron microscope images of the sidewalls before testing and after 2M rev. at an average of 10,000 rpm.

Ejected wear debris was observed on the plumbing wafer in tests that spanned 5M revolutions or more. Figure 4.9(a) shows the plumbing wafer removed from the MTD package after 45 M Revs. operation. A halo of wear debris, following the blade arrangement of the turbine can be observed around the turbine outlet. Figure 4.9(b) and (c) show the SEM micrograph of the wear debris and the subsequent EDS chemical analysis clearly showing the wear debris is composed primarily of iron and therefor originates from the microball.
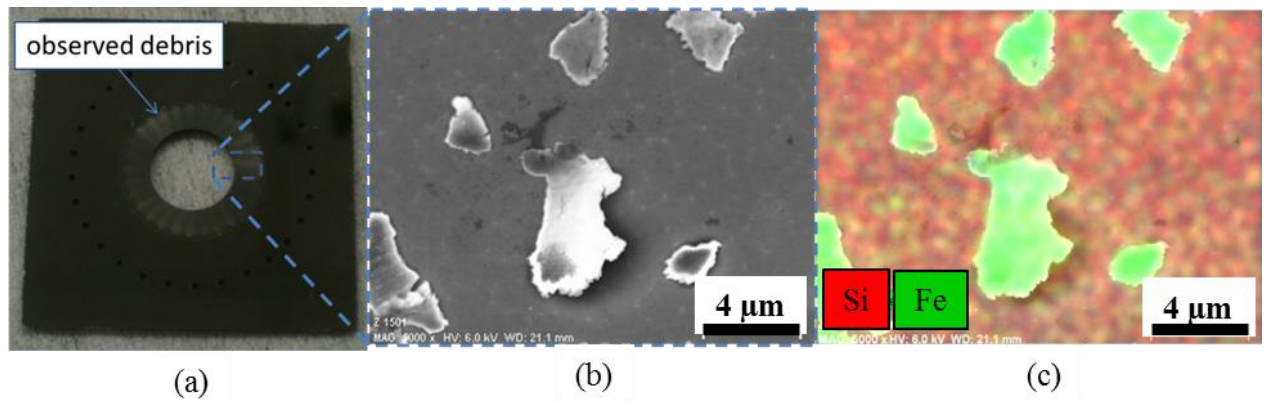
Figure 4.9. (a) Optical image of plumbing wafer after 45M rev. testing,(b) SEM image of ejected wear debris and (c) chemical analysis of SEM image showing ejected debris is ball material.

Figure 4.8 and Figure 4.9 exhibit the two debris-generating mechanisms during long-term turbine operation. This debris can be removed by ultrasonic cleaning of the device, which is shown Figure 4.7 (inset) where the device returned to original performance values after a cleaning procedure. The ratio of the effects of side wall (silicon) to ball (steel) debris is not known, although the steel debris is significantly more numerous after testing.

4.4   Adhesive mechanism

The primary mechanism of wear observed in the tested microsystems is of an adhesive nature between the ball and the raceway. Figure 4.10 shows an optical micrograph from *D1* showing patches of ball material adhered to the silicon raceway.
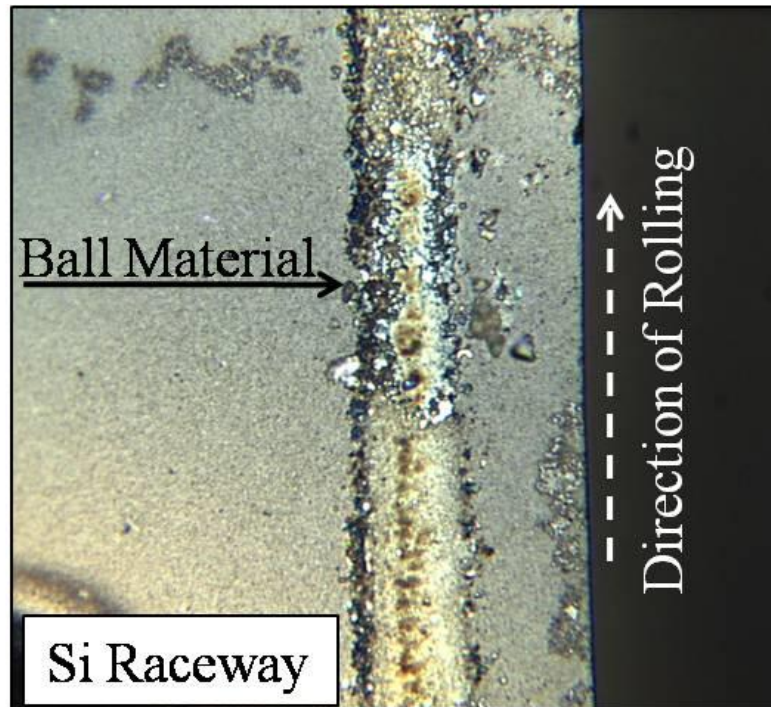
Figure 4.10. Optical Micrograph of silicon raceway after 2M rev. wear. Stainless steel ball material can be observed throughout, in both trace amounts and significant islands.

The adhesion mechanism is described schematically in Figure 4.11. Adhesion occurs when contacting materials are placed under high pressures. During rolling, temporary bonds are made between the ball and the raceway. As the ball continues to roll, shear stress acts to create a surface with minimum energy, on some occasions shearing through the ball instead of the ball/raceway interface, leaving adhered ball material behind. Stainless steel ball material is observed on thrust-loaded surfaces; therefore paths 1 & 2 dominate.
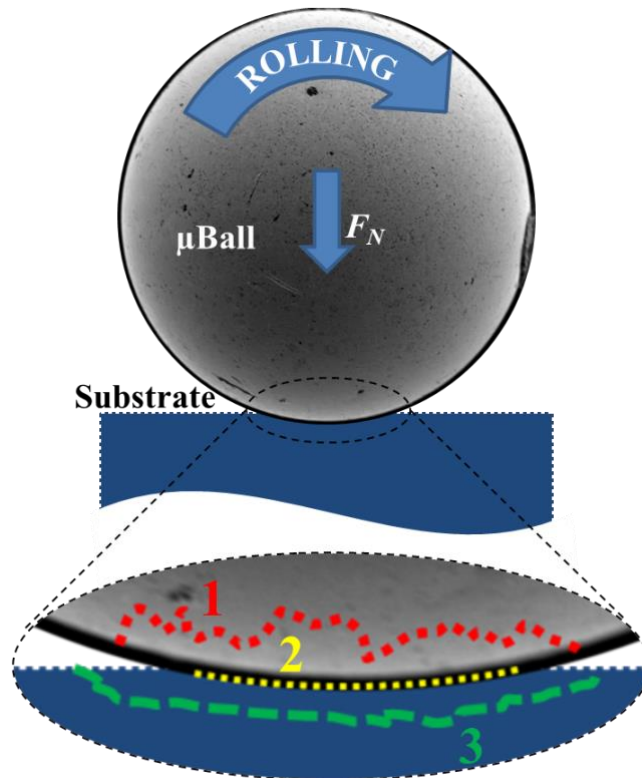
Figure 4.11. Schematic of adhesive wear mechanism. As rolling progresses, new junctions are formed at the ball-substrate interface. This junction will be released by the crack propagation mechanism of the lowest energy, following path 1 through the ball, 2 through the ball-substrate junction, or 3, through the silicon substrate.

Optical profilometry was utilized to determine the geometry of the adhered ball material. A characteristic profile of the adhered wear debris is shown in Figure 4.12, from device *D6* operated at 200 mN rotor load for 20 Mrev. The average height of wear debris was measure to be 114 nm and 301 nm for *D4 & 6*, respectively.

The measured adhered wear debris correlates to wear rates of 0.0004 μm^3/mN·rev and 0.00004 μm^3/mN·rev for *D4* and *D6,* respectively. The order of magnitude reduction in wear rate for *D6*, which underwent 4 times normal load and over 6 times the lifetime, suggests that the adhesive wear rate is high early on and then diminishes significantly over the course of operating the device. The height has not been measured on *D5* because it is still under test or

D7 because this device experienced raceway fracture.
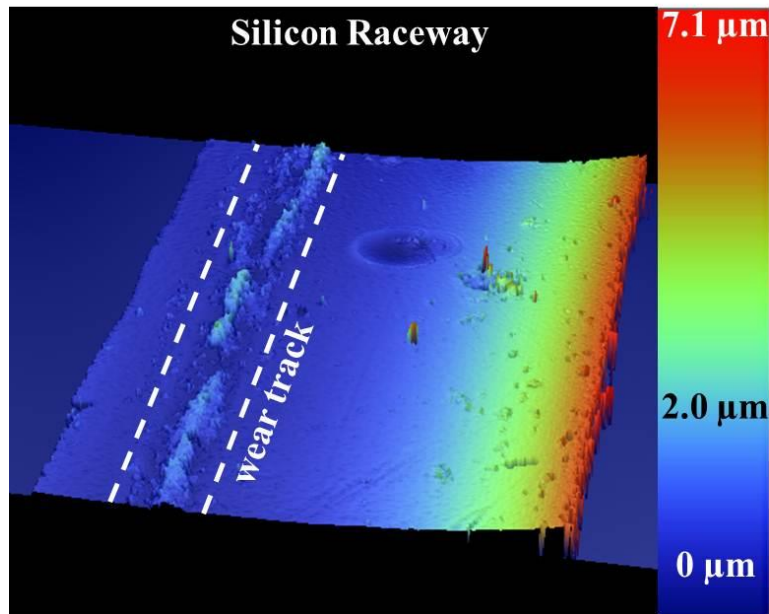
Figure 4.12. Optical profile image of silicon raceway with highlighted adhesive wear track.

SEM images in Figure 4.13(a-c) shows the adhesion of ball material for *D1* and the TiN (*D2*) and SiC (*D3*) coated raceways. It should be noted that there is not significant misshaping or observable wear on the balls themselves. This is due to the gradual nature of adhesive wear coupled with the random motion of the ball. Spatially resolved EDS spectra of the wear tracks, in Figure 4.13(d-f), reveal adhered ball material on all tested raceways, observed as the presence of Chromium and Iron peaks in the x-ray spectra.
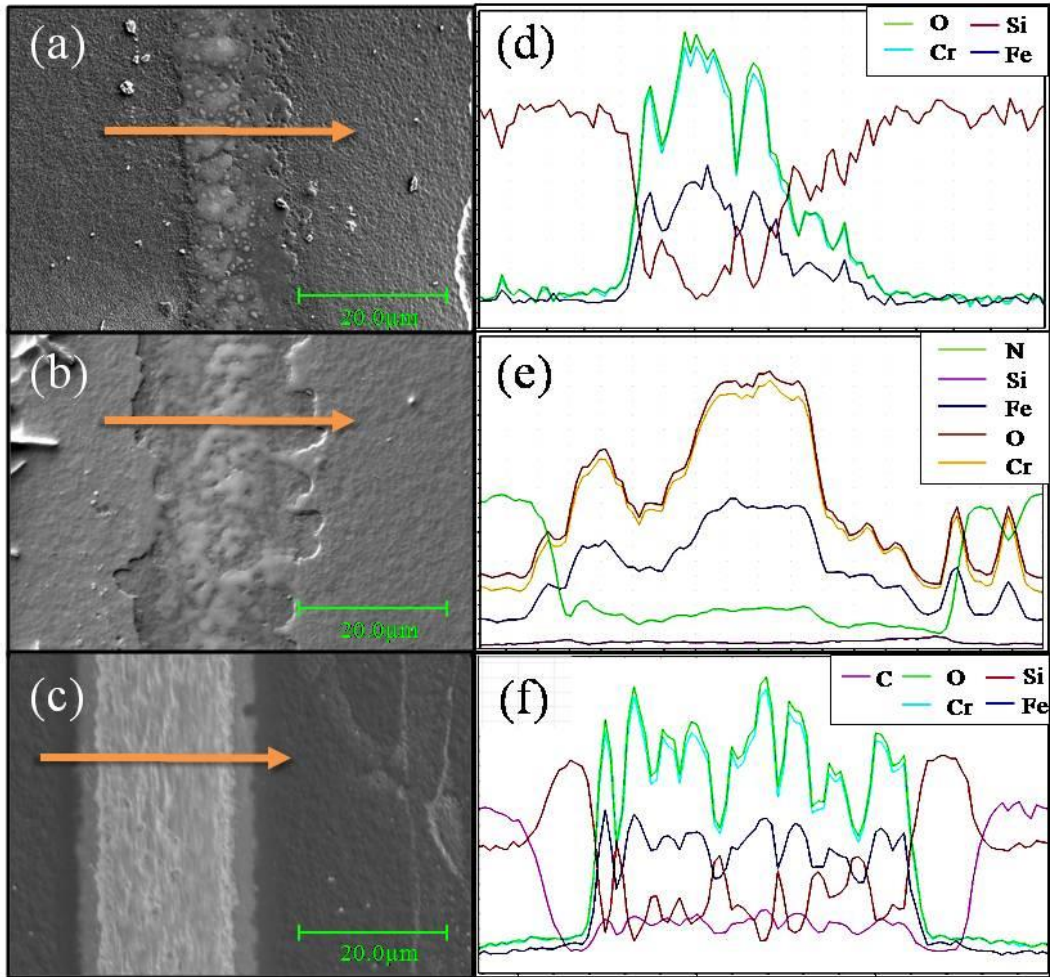
Figure 4.13. Left, (a-c) Scanning Electron Microscope images of characteristic wear track within the ball contact area for (a) silicon, (b) TiN coated and (c) SiC coated raceways. EDS line scans taken perpendicular to each wear track presented in (d-f), correlating with the adjacent SEM image. Iron and Chromium are present in each scan, arising from adhered ball material.

From the SEM images in Figure 4.13(a-c), the specific nature of the ball adhesion can be observed. Ball material adheres non-continuously in the TiN coated raceway and bare Si raceways. SiC coated raceways had an approximately continuous coating of the ball material through the wear track of the raceway. The worn ball material exhibited a directionality paralleling the direction of motion of the ball, which suggests some abrasion by the significantly harder film on the steel balls and/or sliding motion in the bearing.

To reiterate a point from the linear wear section: In the long term, the adhesive wear rate is expected to reach a virtual equilibrium. At equilibrium, the contact path in the raceway has been coated with ball material. The wear, however, does not arrest, it takes place via a ball material transfer. The ball adheres to ball material on the raceway, and fractures in three mechanisms: through the newly formed contact, through the ball (depositing on the raceway), or through the adhered wear track (depositing on the ball). The three mechanisms are equally probable, resulting in a net-zero *observed* wear rate.

4.5   Phase change

Figure 4.14a shows Raman spectra comparing worn and unworn regions of two silicon raceways (*D1* and the microturbine in [1]). The broad peak at 160 cm^{-1} and the shoulder at 470 cm^{-1} coincide with a stress-induced amorphous-silicon (α-Si) phase specific to the worn areas of the race.
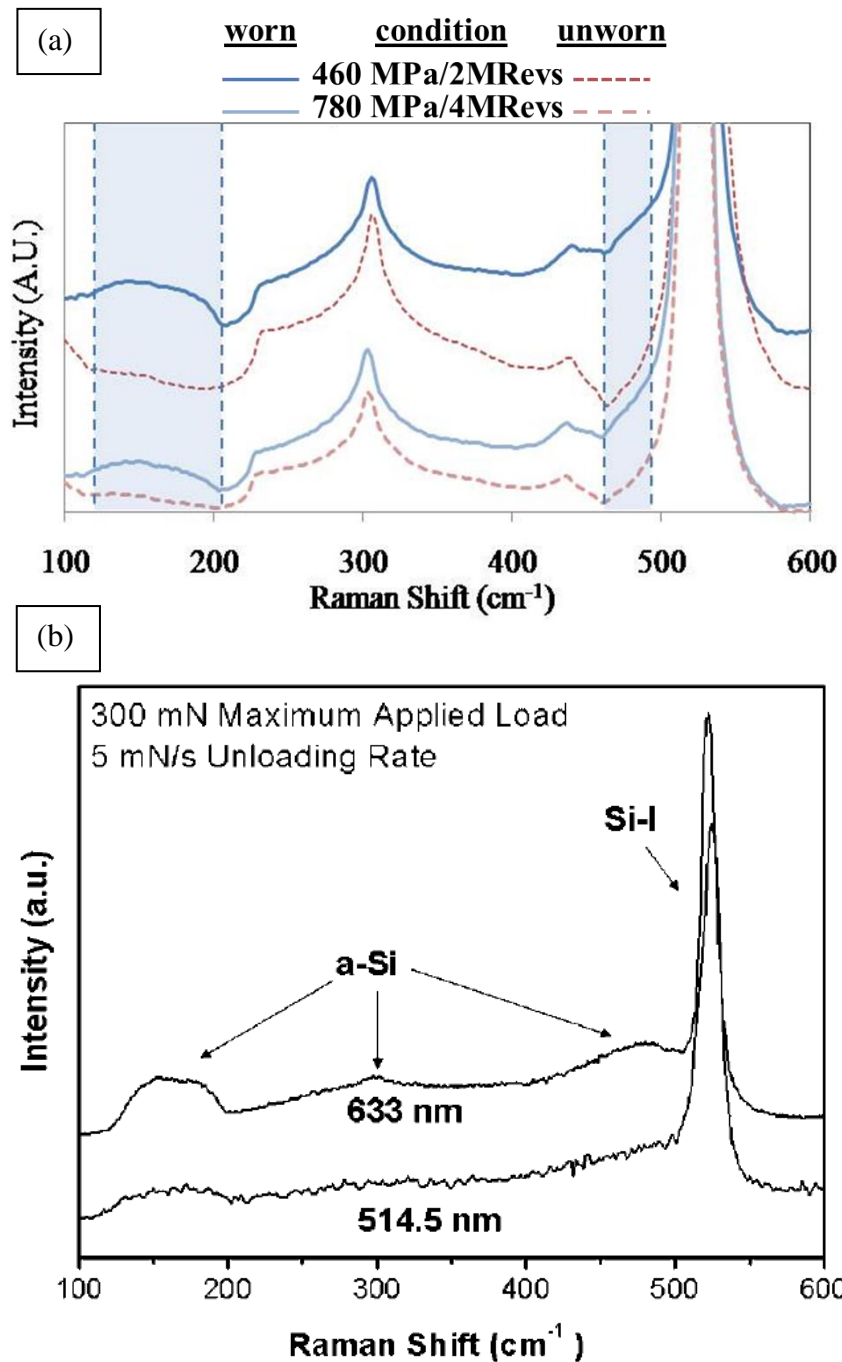
Figure 4.14. Raman Spectra from two silicon raceways, tested to a maximum contact stress of 460 MPA and 780 MPa. Amorphous silicon phase present in worn areas, at 160 and 470cm^{-1} and not visible in unworn areas of the same bearing.

Previous work on the characterization of nanoindentation of silicon with spherical indenters acts as a close analog to the morphologies observed in the microball bearing. The results presented in [99, 100] show that pressure induced phase transformations occur at

contact pressures on the order of 2 GPa up to 7 GPa, which is an order of magnitude higher than the calculated contact pressure for the microball bearings tested (figure 4.14b). In our devices, the phase change is observed at 140 MPa and 500 MPa average ball stresses, assuming 100 balls are equally supporting the load, for rotor loads of 10 mN and 500 mN, suggesting that either peak stress within the turbine is much higher than calculations, or the phase change mechanism is rate dependent. The calculated peak stress is known to be an underestimate of the actual peak stress due to the assumption that all balls are in contact with the raceway uniformly. Realistically, a fraction of balls are supporting the rotor normal load due to the raceway waviness and therefore the actual peak loads are much higher. The nanoindentation studies also showed other silicon crystalline phases present in the solid after indentation whose amount and morphology were highly dependent on the kinetics of the loading procedure [101]. The lack of alternative Si phases in our work could be due to the cyclical nature of the loading and the short elastic recovery time between loadings. α-Si has a reported Young's Modulus and hardness of up to 80% and 90% of that of single crystalline Si [102], and up to a 67% increased fracture toughness [103]. The slightly reduced modulus and hardness would cause, if anything, marginally higher rolling friction due to increased deformation (elastic and plastic), although some overall benefit may be realized because of the reduction in wear rates due to the increased fracture toughness of the a-Si, therefore the net performance benefit/detriment is unknown.

4.6   Thin film wear

Thin film coatings tested exhibited wear mechanisms in addition to the adhesive mechanism previously discussed. Inspection revealed surface wear and interfacial delamination observed in both the SEM image (Figure 4.13b) and optical micrograph (Figure 4.15a) of TiN coated raceways. The raceway coating remained 60% intact beneath the wear track after 2M rev., so the delamination is assumed to be a gradual process. The wear was

continuous along the ball contact track, with occasional spalling of the coating. The high sub-surface shear stress from the microball contact under load would be expected to induce film delamination which leads to spalling. SEM inspection revealed that ball material adheres to the TiN film as well as the exposed bare silicon, although there seems to be a significant preference for silicon over TiN surfaces from Figure 4.15a. Future TiN coatings with better adhesion properties could serve to mitigate wear in the long term through the lowered affinity for stainless steel adhesion.
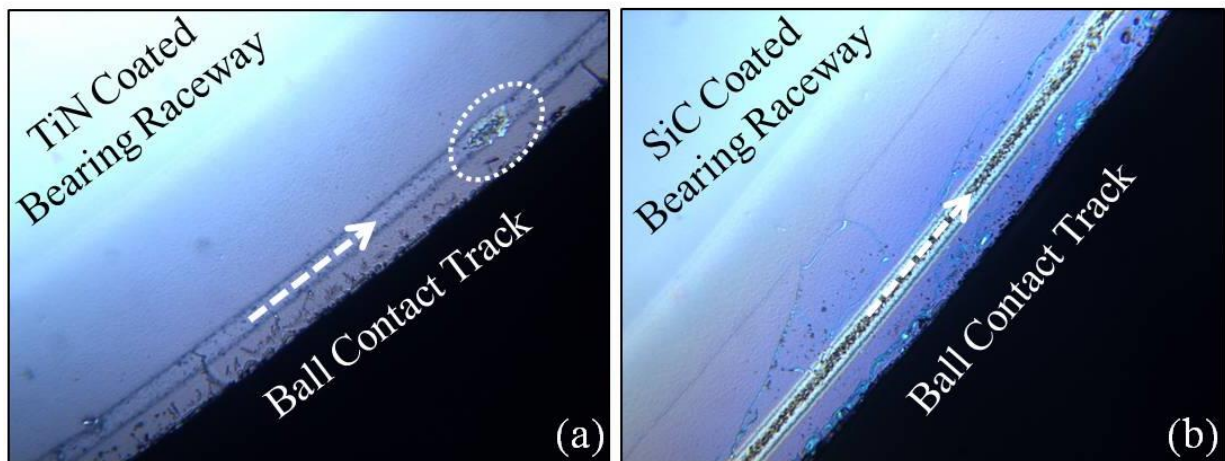
Figure 4.15. Optical micrographs of (a) TiN with ball material observed adhered to the bare silicon revealed from thin film wear and (b) SiC coated raceways exhibiting a continuous track of adhered ball material.

The sliding ball motion could have been caused by fragments of the SiC thin-film impeding the rolling of the balls, which correlates with the poor performance of the microturbine with SiC thin films shown in Figure 4.5. Figure 4.13c and Figure 4.15b show a SiC race after only 30k revolutions of testing at ball contact stress levels less than 100 MPa with significant wear. SiC film wear was limited to the contact area of the ball, while fracturing was observed throughout the raceway (Figure 4.15b). The residual stress of the film in the SiC film could have contributed to the rapid wear, although the stress was not

measured.

UNCD thin films were also considered for the rotary systems based on the positive linear tribology data. Device-level deposition of UNCD films was performed at the Center for Nano-scale Materials (CNM) at Argonne National Labs. The devices were then assembled and tested. Film delamination was problematic and CNM researchers believe it was issues with adhesion layer quality. Figure 4.16a shows the delamination of the UNCD film after an ultrasonic cleaning step before bonding. After testing, Figure 4.16b&c show the bearing raceway which exhibits significant film delamination and surface roughening in an SEM and optical profile image, respectively.
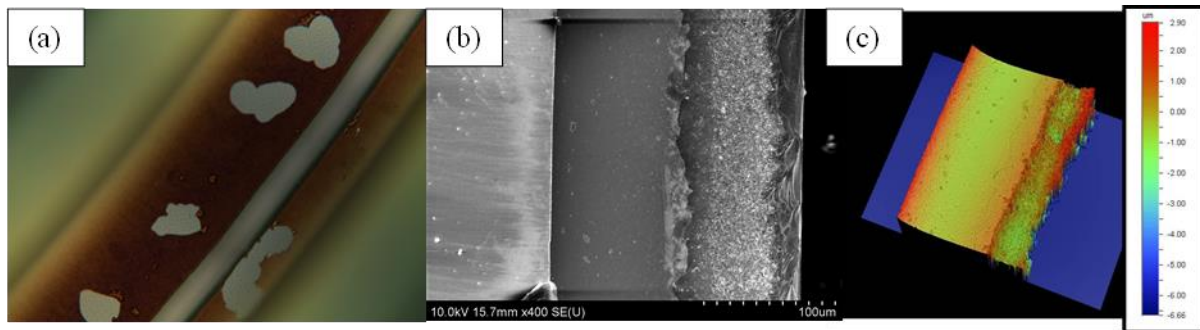
Figure 4.16. (a) optical image of UNCD coated raceway after cleaning before testing, (b) SEM of worn raceway, film delamination apparent and (c) 3D optical profile of wear area.

4.7   Ball Wear

Observation of the wear on the microball provides insight as to the wear mechanisms and general performance of the system. Adhesive wear was the primary mechanism observed on the silicon and coated raceways. Figure 4.17 shows a comparison of a fresh ball, and one that has been tested on silicon raceways for 2Mrev. and 20 mN normal load.
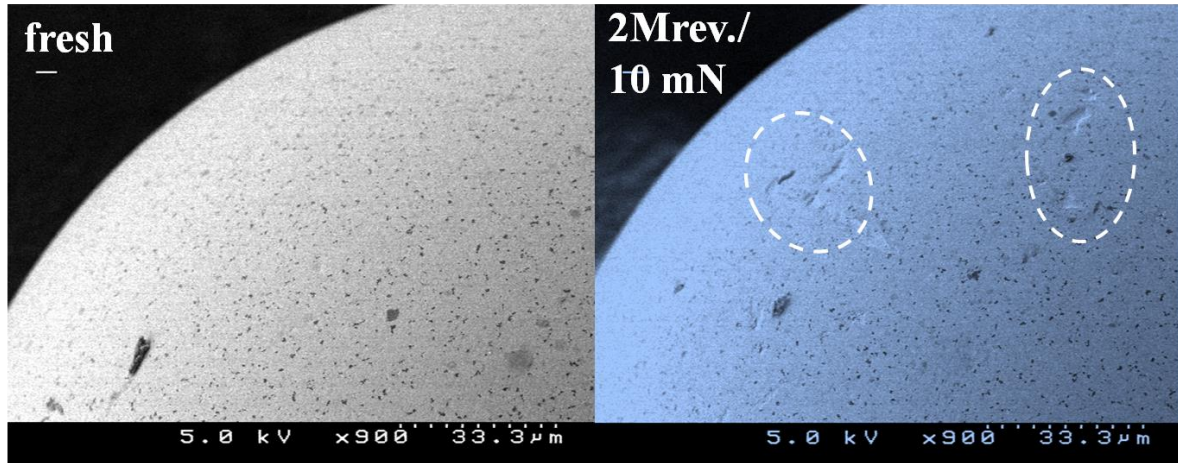
Figure 4.17. SEM images of microballs (left) unused microball and (right) microball that was tested in D1. Areas of removed ball material are shown.

The observed wear on the ball, in the form of missing ball material, was minor. The expected depth of removed ball material can be calculated knowing geometries of the system and adhered wear track, assuming all removed ball material adheres to the raceway. The largest adhesive wear track of 301 nm in height and 12 μm in width was observed for device *D6* , operated for 20 Mrev. at 200 mN rotor normal load. This correlates to total wear volume of $1.13 \times 10^{-13} m^3$. One hundred, 285 μm diameter microballs were used for this test, with a calculated total surface area of $2.55 \times 10^{-5} m^2$. If it is assumed that the ball randomly and evenly donated material to the raceway surface, then that would result in an overall change in dimension 4.45×10^{-11} m per ball. This helps to explain why the observed wear on the ball is minimal.

There was also evidence of ball-to-ball contact in the form of minor, directional plow marks. Figure 4.18 shows a zoomed in image of a microball bearing exhibiting evidence of the plowing taking place from ball-to-ball contact.
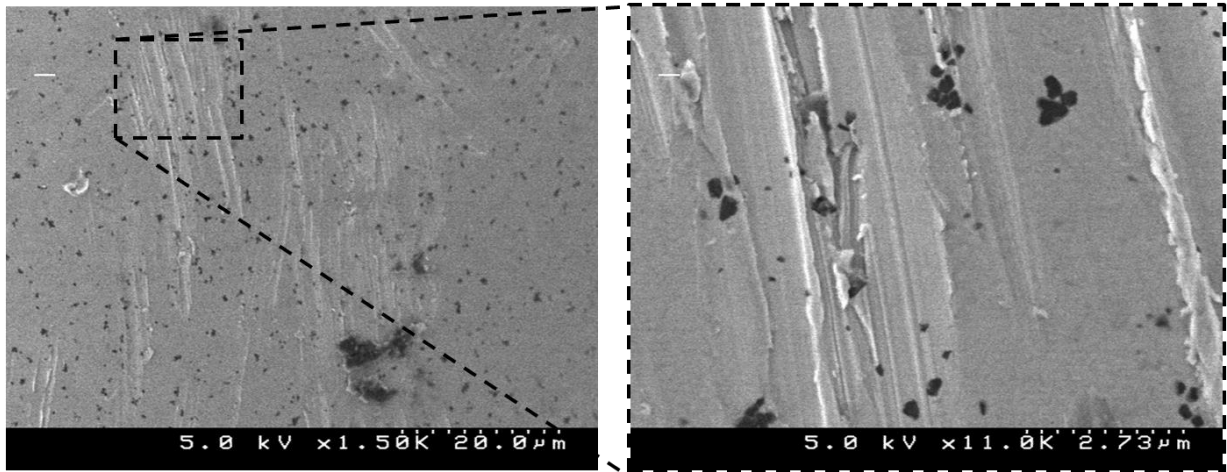
Figure 4.18. (left) SEM image of surface of worn microball. (right) zoomed-in image, showing plastic deformation of ball surface.

The width of each plow mark is on the order of 1 μm, which would suggest the plowing is from ball-to-ball contact, although some skidding could be taking place during start-up of the microturbine when it is operating under very low normal load (<5 mN) and likely has significant sliding of the microballs. This skidding at low loads would give a similar wear mechanism.

4.8 Rolling Contact Fatigue

Removal of raceway material was observed in the highest loaded system only, *D7* (400 mN rotor load, stress/ball = 485 MPa). This wear regime coincides well with the wear reported within a microfabricated turbopump, operated at similar stresses (518 MPa) [1]. *D7* was operated for 8.6 krevs before ultimate failure, attributed to fracture of the raceway. Rolling contact fatigue (RCF) induced spalling caused the progressive removal of raceway surface material, altering the raceway from a flat geometry to a curved surface mimicking the geometry of the ball. Figure 4.19 shows an SEM of the worn raceway.
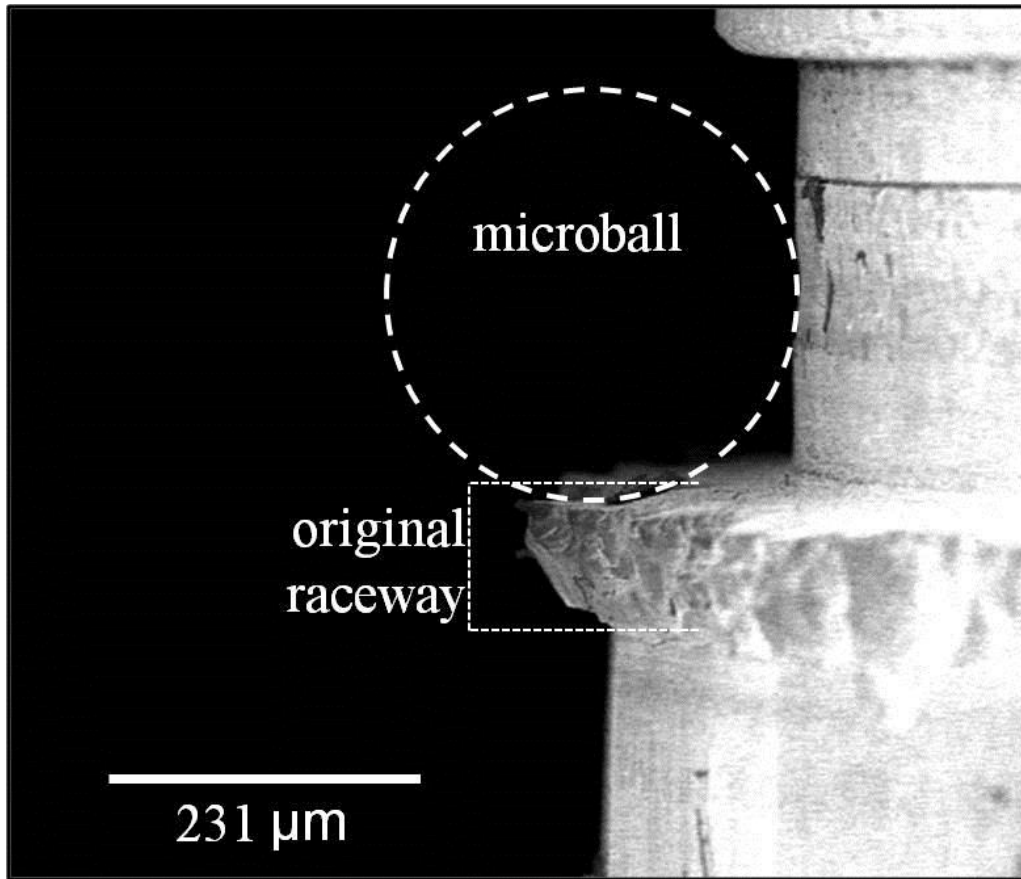
Figure 4.19. SEM image of fractured raceway surface of device tested at 400 mN rotor normal loads

The RCF spalling mechanism in ceramics is described by Wereszczak *et al.* as the progressive creation of sub-surface cracks within the ceramic which propagate and coalesce to disconnect a particle from the substrate. The wear process gradually reduces the contact pressure by increasing the contact area. Initial values of mean contact pressure and contact area per ball are calculated from Hertzian contact mechanics to be 485 MPa and 8.0 μm^2. Upon wear of the raceway, assuming a 150 μm wear groove radius (estimated from figure 13), the contact pressure is reduced by one third to 334 MPa due to a 33% increase in contact area to 12.0 μm^2. The fracture strength of silicon from a tensile test of a microfabricated specimen is estimated to be in the range of 1-3 GPa [104], well above the stresses in the bearing, therefore it is assumed that the spalling is a result of a fatigue mechanism. Bhowmick *et al.* tested bare silicon samples under static loading and fatigue conditions and

found that there is an order of magnitude decrease in strength for cycle lifetimes from 10^3-10^6 cycles [105]. This result elucidates the contact pressures that can be used in an engineering application for spall-free operation.

4.9 Conclusion

The wear mechanisms of a microfabricated ball bearing system have been evaluated. A silicon microturbine and linear test device supported on encapsulated microball bearings were utilized to serve as the test platforms for this study. The raceways were tested bare as well as coated with UNCD, SiC, and TiN thin films to evaluate a possible reduction in friction and wear. Accelerated wear testing was performed in the linear regime through the use of reciprocating motion under load. Wear was also studied by rotating the microturbine rotor under load for a set number of revolutions. Ball material adhesion was found to be the primary wear mechanism, present in in both the coated and uncoated raceways. The SiC coating immediately wore, leaving behind a silicon surface that enhanced ball adhesion. The TiN coating wore gradually, lasting 2M revolutions before the friction became too erratic to test. Inspection of the raceways revealed that select area of the TiN film had been removed, suggesting a gradual, sub-surface mechanism. For bare silicon raceways, it was shown through Raman Spectroscopy that the contact pressure beneath the balls was amorphisizing the raceways via a pressure-induced phase change. Silicon raceway fracture dominated over adhesion in only the highest-tested load regime, elucidating the maximum stress allowable for long-term (adhesion regime) operation. The ball strength and chemistry needs to be addressed for microball bearing devices to be operated in the 1 Billion revolutions regime.

The wear study has many implications regarding the design and fabrication of future microball bearing systems. Firstly, the primary observed wear mechanism of adhered ball material supports the adhesion-dominated friction hypothesis discussed in the previous

chapter. Future systems will need to utilize lower surface energy materials, such as ceramic balls, or small contact areas to reduce the magnitude of adhesion. The observation of sidewall degradation suggests that new raceway geometries should be explored that can better handle centripetally-induced radial loads. New raceway geometries will be the subject of chapter 6. It is expected that reducing blunt sidewall impacts will also reduce the volume of wear debris generated, therefore reducing its effect on long-term device performance. The wear study also illuminated the wear mechanism at high contact pressures, which provides an upper limit for the loads microball bearing machines can handle. There was no significant benefit of hard-thin-films observed for the rotary regime devices, therefore adhesion-mitigating surface layers will be explored as a possible alternative in the following chapter.

5. Lubrication

Lubrication is used to prevent solid-solid contact of mating surfaces. In the realm of sliding friction, lubrication prevents asperity contact, and therefore reduces overall friction significantly. In the realm of macro-scale rolling friction, where elastic hysteresis dominates, lubrication is primarily used to reduce the sliding friction between balls and ball-retainer ring contacts. Additionally, lubricants are used to provide a barrier against corrosive materials. In the case of micro-scale rolling friction vapor-phase lubrication (VPL) is used to address adhesion, the hypothesized dominant factor in micro-scale rolling friction, through the reduction of surface energy and the prevention of solid-solid ball-raceway contact. The experimental methods described in chapter 3, namely spin-down friction and performance testing, have been utilized with a new, custom experimental set-up that allows for the controlled introduction of vapor-phase lubricants.

.

5.1 Experiment

The efficacy of VPL was determined through the operation of a custom-built silicon microturbine as described in chapter 2. The microturbine is actuated via two different flow paths, shown below in Figure 5.1 . An apparatus was designed and constructed to actuate and pressurize the air-driven microturbine with various levels of vapor lubrication saturation. The experimental set-up includes a temperature-controlled bubbler and condenser, multiple pressure regulators, and finally a mass flow controller before the vapor-saturated nitrogen enters the microturbine packaging.

The actuation flow spins the rotor, while the thrust flow provides normal load. Constant flow is provided to the microturbine during both general performance testing and normal load-resolved spin-down friction testing (procedures discussed in chapter 3). This

flow allows for the vapor molecules to be constantly replenished on the surface of the raceways. A general schematic of the VPL system is shown below in Figure 5.2.
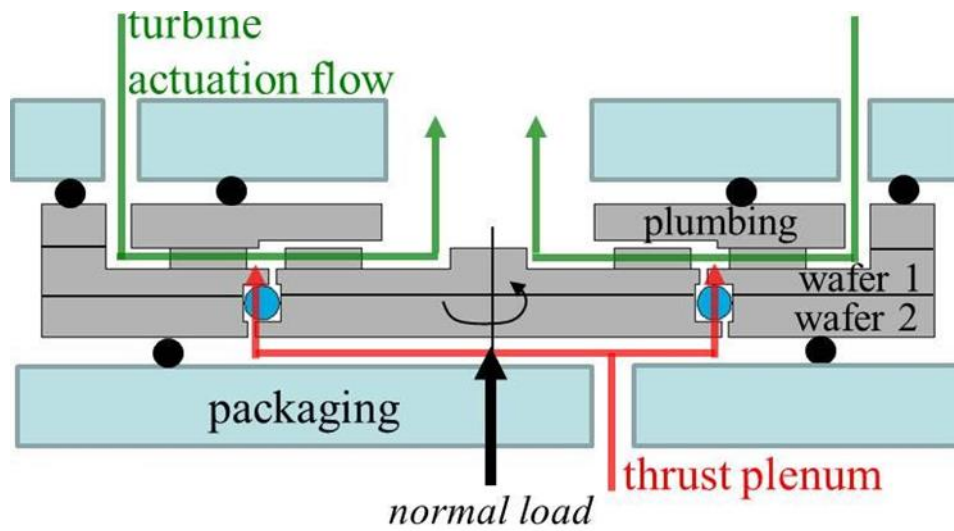
Figure 5.1. Schematic of packaged microturbine, highlighting flow paths.
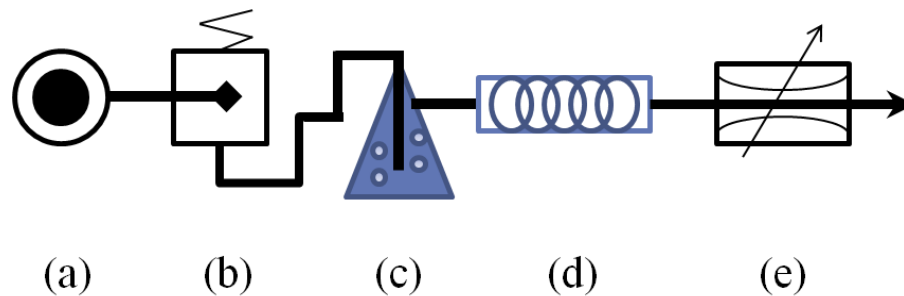
Figure 5.2. Engineering schematic of the VPL set-up. (a) input pressure source, dry nitrogen, (b) pressure regulator, (c) bubbler with heating capabilities, (d) condenser/reservoir, (e) mass flow controller to turbine output.

The carrier fluid for all of experiments is lab-grade dry nitrogen. Upon exiting the nitrogen tank, the pressure is stepped down before the heated bubbler stage (Figure 5.2(c)). The ratio of input to output pressure is critical to the relative vapor pressure at the output. The effects of pressure and temperature on lubrication quantity are discussed in greater detail in

the following sections. The next stage (Figure 5.2(d)) is the condenser, used to prevent liquid-phase lubrication from entering the mass flow controller in stage (e).

5.1.1 Characterization

The thermodynamic and kinetic system states determine the morphology and replenishment properties of the VPL molecules, as derived in the previous section. The governing system properties are temperature, pressure, and flow rate, which affect vapor pressure (P_{vap}), saturation vapor pressure (P_{sat}), and the rate at which new molecules are delivered.

Temperature control is integrated within the bubbler/condenser stage of the set-up. Heating the bubbler allows for increased P_{vap} at a given pressure, which translates to faster VPL coating and possibly greater coating thickness. To heat the bubbler, a joule (resistance) heater is affixed to the pressurized high density polyethylene (HDPE) bubbler. Power is provided to the heating tape via a variable transistor (variac). The glass transition temperature of HDPE is reported to be 135°C, but since the vessel is under pressure, a safety factor of 2 was applied and heating was limited to 65°C. A graph of the temperature/relative humidity is shown in Figure 5.3 below.
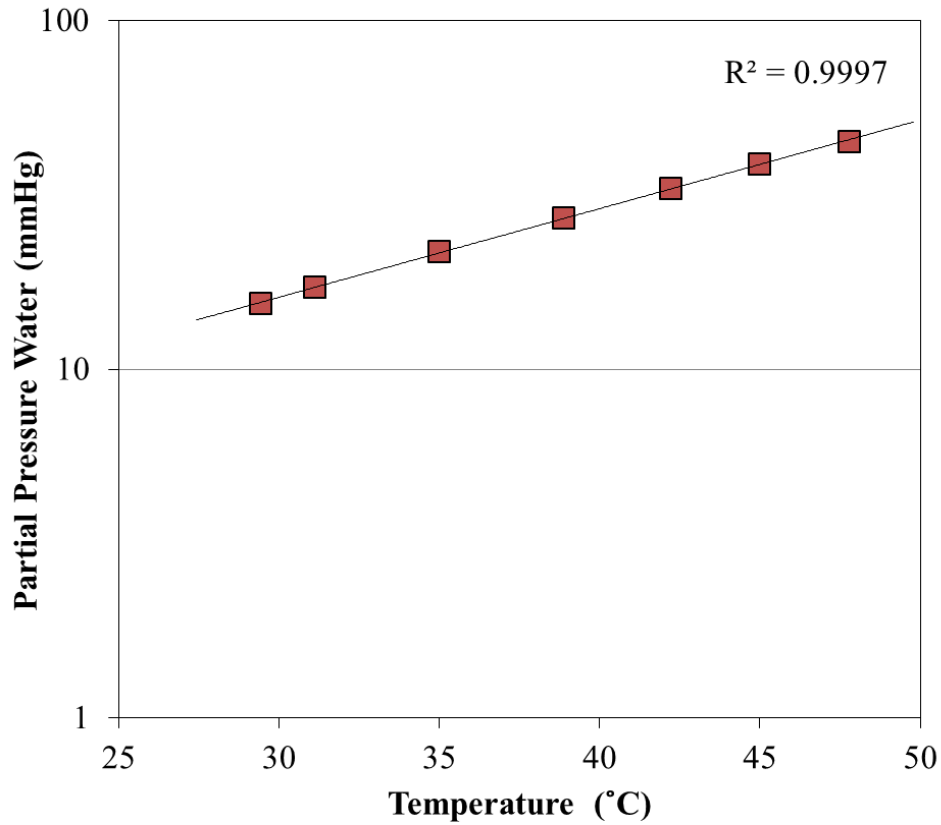
Figure 5.3. Chracterization of log water partial pressure against temperature. Exponential fit and R^2 value shown.

The relationship between temperature and P_{vap} is described by the Antoine equation.

$$log_{10}P_{sat} = A - \frac{B}{C + T} \qquad (5.1)$$

The exact equation cannot be simply fit to the characterization data because of confounding issues, such as changing pressures, volumes, and leakage. The nature of the exponential relationship between P_{vap} and temperature is maintained.

The principle use of the condenser stage is to assure there is no liquid lubricant introduced into the microturbine. When the liquid lubricant is heated in the bubbler stage, the carrier gas becomes supersaturated relative to the room temperature state, therefore as the gas

cools, less vapor molecules are supported in the suspension and some condense into liquid. This can be prevented by inducing condensation just after the bubbler by cooling the carrier gas below room temperature.

Pressure, specifically the ratio of bubbler pressure to output pressure, plays a significant role in determining the deliverable P_{vap} value. This can be explained by the weak dependence of P_{vap} on total pressure (P_T). Assuming the vapor pressure does not depend on total pressure, then the vapor pressure will be the same absolute value regardless of the pressure in the bubbler. The input pressure of the turbine has a narrow range of acceptable values, therefore the system pressure from the bubbler has to be stepped-down through the system. Since the P_{vap} is only introduced in the bubbler stage, it is set at a fixed pressure, therefore during future stages when the pressure is stepped down, the original *ratio* of P_{vap} to P_T is maintained. This is a very useful tool, as it gives a wider range of possible P_{vap} than temperature alone. Figure 5.4 shows the partial pressure at a constant output pressure vs. input pressure.
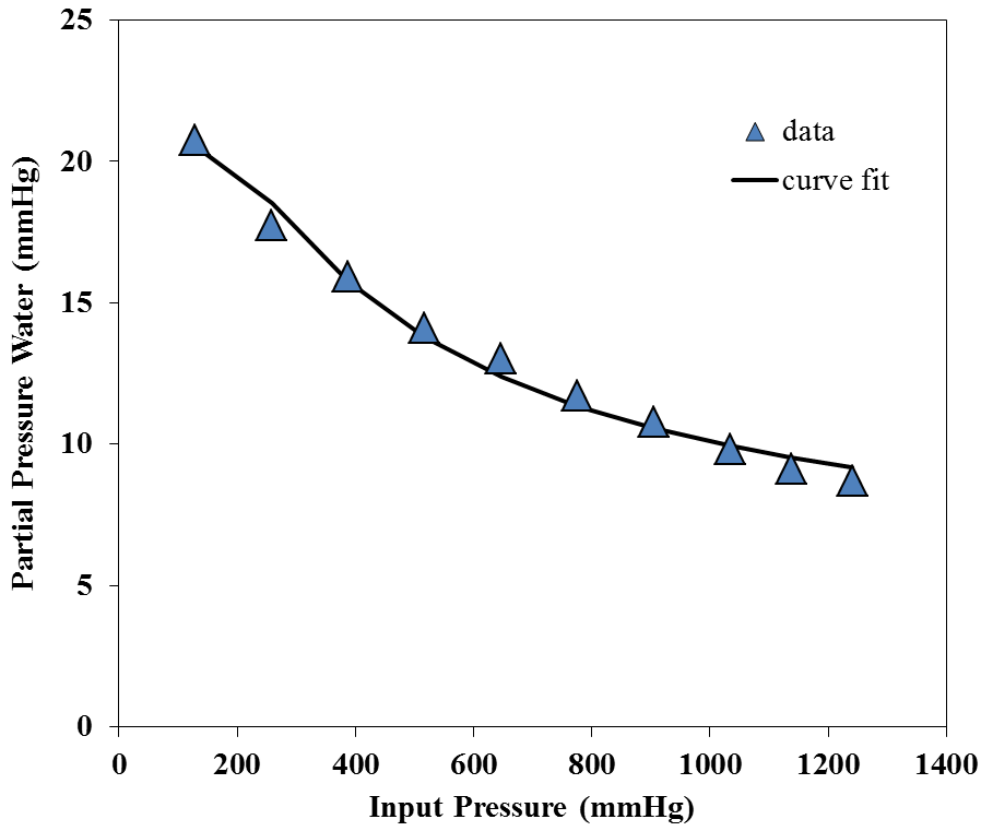
Figure 5.4. Partial pressure of water versus input pressure, plotted against theoretical curve fit.

From this data it was determined that partial pressure did not depend on the ratio of P_{vap} to P_T, but rather changes in temperature and volume had to be added to the equation, according to the ideal gas law. We know, from Antoine's equation that P_{vap} can be described as an exponential function of temperature (T),

$$Log_{10}P_{sat} = \left(A - \frac{B}{C + T}\right) \qquad (5.2)$$

with A, B, and C being material constants. T depends on the system states from the ideal gas law,

$$T_2 = \frac{P_2 V_2}{P_1 V_1} T_1 \qquad (5.3)$$

110

where T_2 is the final system temperature, T_1 and P_1 are known, and the remaining states are bundled into a constant b.

$$P_{sat} = 10^{\wedge}\left(A - \frac{B}{C + \left(\frac{b}{P_1}T_1\right)} \right) \quad (5.4)$$

Relative saturation (RS) is the ratio of P_{vap} to P_{sat}, and that P_{vap} depends on the ratio input to output pressure, so RS depends on the output pressure,

$$P_{sat} = \frac{P_{vap}}{RS} \quad (5.5)$$

And

$$RS = \frac{P_2}{P_1} \quad (5.6)$$

Rearranging we arrive at the curve fit from Figure 5.4,

$$P_{vap} = \alpha * 10^{\left(A - \frac{B}{C + \left(\frac{b}{P_1}T_1\right)} \right)} * \frac{P_2}{P_1} + \beta \quad (5.7)$$

With the α and β terms introduced as fit parameters.

The final experimental variable on the VPL set-up is flow rate. Tested flow rates ranged from 1-10 standard liters per minute (SLM), relevant to flow rates required to operate the microturbine. It was shown that, as expected, there is a weak dependence of relative humidity on flow rate. Flow rate variation has the potential to influence the kinetics of the system, more specifically, the bubble size and residence time. For the range of flow rates tested, this did not significantly affect system performance.

5.2 Set-up and experiment

The ultimate goal of the VPL system is to deliver a known amount of vapor-phase lubrication molecules to a surface while ensuring there will be no condensation to liquid phase. The delivery of known quantities of vapor, understanding the parameters that control the relative saturation of fluids, and the process of adsorption are all challenges necessary to designing and implementing a VPL scheme at any size scale.

In a mixture of ideal gases, the partial pressure of a gas is equal to the amount of pressure that the gas molecules would exert if they were the only component in the system, depending on the thermodynamic activity of the gas molecules. For non-reacting gasses, the total pressure of the system is the sum of the partial pressures of its components, known as Dalton's Law,

$$P_T = P_1 + P_2 + P_3 \qquad (5.8)$$

where P_T is the total pressure of the system and P_i is the partial pressure of a component. Equilibrium vapor pressure is the pressure exerted by the vapor-phase of an isothermal liquid or solid in a closed container. The temperature at which the vapor pressure of a liquid is equal to one atmosphere of pressure (1 atm) is known as the boiling point of that liquid. For VPL systems, high vapor pressure liquids introduce more molecules into the gas than low vapor pressure liquids for a given volume and temperature, from the ideal gas law,

$$PV = nRT \qquad (5.9)$$

Where P is pressure, V is volume, n is the number of molecules, R is the universal gas constant and T is temperature. From the ideal gas law, you can see that if pressure goes up for an isothermal, isochoric gas, then n must compensate.

To determine how many vapor molecules, n, are in a system, the saturation vapor pressure (P_{sat}) must be discussed. The P_{sat} is the pressure of vapor molecules that can be supported in a carrier gas at a given temperature and pressure, which can be determined by the vapor pressure of a liquid *just above* the surface of the liquid. It can be assumed that the gas exiting the bubbler stage of the VPL delivery system is at its P_{sat}. The calculation of P_{sat} is non-trivial, and depends significantly on empirical data of the system. The simplest treatment is the Antoine equation,

$$log_{10}P_{sat} = A - \frac{B}{C + T} \tag{5.1}$$

Where P_{sat} is vapor pressure, A, B, and C are component specific constants, and T is temperature. The values of A,B, and C have been calculated for a number of liquids and temperature ranges, and are generally available through the National Institute of Standards and Technologies website [106].

Once the gas exits the bubbler, the partial pressure of the vapor component of the mixture is at the P_{sat} of the liquid. Beyond the bubbler there are pressure and temperature variations in the system, therefore it is important to introduce the concept of relative saturation (RS), which is the ratio of the partial pressure, P_{vap}, of the vapor to P_{sat},

$$RS = \frac{P_{vap}}{P_{sat}} \tag{5.10}$$

P_{sat} is determined by T and the composition of the gas. A RS of 100% means that the vapor partial pressure of the system is at the P_{sat} for that thermodynamic state. *RS* levels above 100% will result in condensing of vapor-phase molecules. At this point it is critical to realize that the total number of vapor molecules, n, is set after the bubbler stage, therefore the rest of the system depends on the thermodynamic state of the bubbler.

Pressure plays an important role in determining the RS of the system. RS depends on the ratio of P_{vap} to P_{sat}, which is a function of T and gas composition. If the pressure of a system (P_T) is isothermally increased, then P_{vap} raises as well (Dalton equation) while P_{sat} remains the same, therefore increasesing RS. This places an emphasis on P_T at the saturation stage (bubbler). RS can be related to the bubbler pressure and output pressure as follows, assuming that the RS is 100% coming out of the bubbler,

$$RS_{output} = 100\% \frac{P_{output}}{P_{bubbler}} \tag{5.11}$$

and an isothermal process.

Temperature affects the denominator of the RS ratio, P_{sat}, by the relationship provided by the Antoine equation (5.1). In general, if you have a system at a given RS, T, and P_T, if you raise T, you increase P_{sat}, thereby reducing RS. The relationship between vapor pressure and temperature is shown in the graph below (Figure 5.5).

114
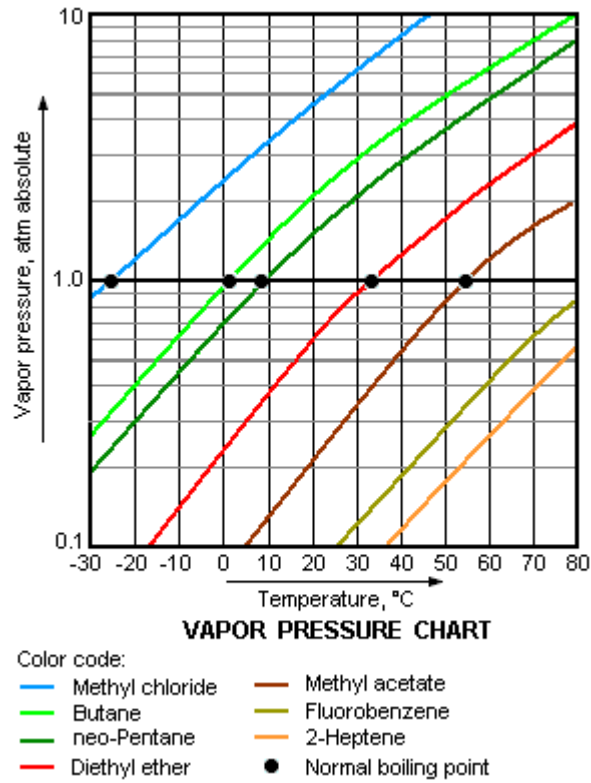
Figure 5.5. Vapor Pressure variation with temperature for a number of organic compounds [107].

P_{sat} increases with temperature according to Antoine's equation and its variants (above), and therefore RS varies with the inverse of (5.1).

Once the relationship between P_{vap} and P_{sat} with temperature and pressure is understood, it's important to see how it affects the engineering and operation of the VPL stage. A schematic (Figure 5.6) has been created to describe the relative states of *T,* P_{vap}, P_{sat}, P_T, and *RS* throughout the set-up described in Figure 5.6. In Figure 5.6, all states are normalized to reasonable values, *T*=1 is room temperature, P_T=1 is the initial pressure of the system, P_{sat}=1 is the saturation vapor pressure of a given lubricant at *T*=1, *RS*=1 is a relative saturation of 100%, and P_{vap} is not normalized to 1, but rather a function of P_{sat} in the bubbler. Throughout the system P_T is dropping, taking discrete jumps at stages (b) and (e) due to the plumbing hardware. Temperature begins at room temperature, and then rises in the

115

heated bubbler (c). Between (c) and (d) T is reducing from convective cooling in the flow lines. At the condenser (d), T drops significantly and then gradually increases towards room temperature. P_{sat} is a function of T, therefore it mimics the trends of the T state. P_{vap} and P_{sat} are equal at the bubbler stage, assuming the carrier gas is fully saturated in the heated bubbler. P_{vap} is downward-sloping from (c) to (d) due to the reduction of P_T. RS=1 at the bubbler stage. RS decreases from (c) to (d), as both P_{sat} decreases due to T, and P_{vap} decreases, due to P_T, presumably faster. At the condenser (d), $P_{sat}<P_{vap}$, thus $RS>1$, and condensation occurs, removing vapor molecules from the gas phase, lowering P_{vap}. RS decreases significantly from (d) to (e) due to the increasing P_{sat} and decreasing P_{vap}. Stage (e) is the mass flow controller directly before the saturated carrier gas enters the microturbine. The drop in P_T at (e) results in a drop of P_{vap}, and thus a reduction in RS. It should be noted that the VPL set-up can be run without a heated bubbler or chilled condenser to simplify operation. For this situation, all of the underlying principles remain the same and a similar schematic can be created. The advantages of this system are simplified operation, while the drawback is potentially a lower RS due to the lack of heating.
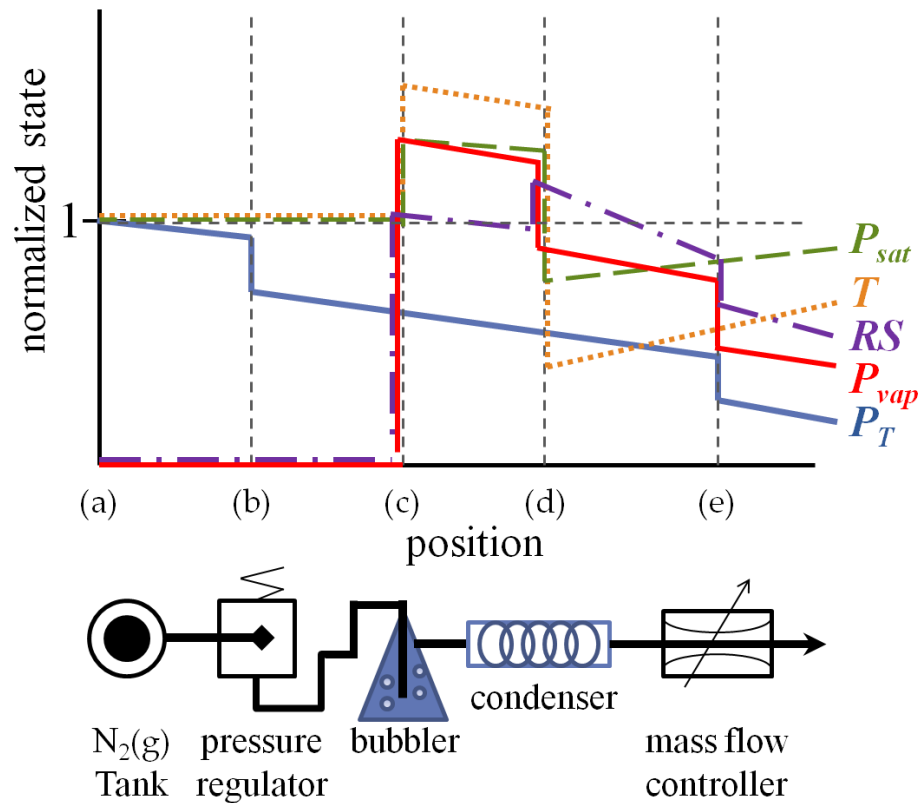
Figure 5.6. Thermodynamic state diagram of VPL set-up utilizing temperature control

The main goal of the VPL set-up is to maximize the P_{vap}, which affects the adsorption of gas-phase lubrication molecules onto the bearing surfaces. The influence of thermodynamic parameters on the VPL has been discussed. Maximum RS can be obtained by minimizing the pressure drop from the bubbler to the output of the plumbing. The P_{sat} of the system is increased at elevated temperatures, therefore higher P_{vap} levels can be maintained as long as the system stays below RS=100%, which represents the condensation conditions. The following section will discuss the parameters influencing adsorption.

5.2.1   Adsorption Isotherms

The efficacy of vapor lubrication depends on the delivery and adhesion of gas-phase molecules to the bearing surfaces through a process called adsorption. Adsorption is a result of an energy-reduction process: the surface atoms of the substrate (adsorbent) are at an

elevated energy state because they are not bound on all sides like atoms in the bulk of the adsorbent, to reduce energy, binding with molecules from the surrounding vapor (adsorbate) occurs. Binding takes one of three forms; physisorption, chemisorptions, or electrostatic attraction. In the case of physisorption, van der Waals forces dominate and adsorbate molecules can bond together and form multiple layers. Chemisorption, in contrast, is characterized by a covalent bond between adsorbent and adsorbate, and chemisorbed molecules typically only form a single layer on the adsorbent. The third mechanism is electrostatic attraction, where oppositely charged species interact.

Adsorption is typically described using isotherms, relating the thickness, mass, or number of adsorbed molecules to the pressure or concentration of said molecules at a constant temperature. The most widely known model isotherm was developed semi-empirically by Langmuir [108]. His model had four main assumptions: 1. a uniform probability distribution of adsorption on the surface of the adsorbent, 2. adsorbed molecules are non-interacting, 3. all adsorption takes place via the same mechanism, and 4. at maximum adsorption, only a monolayer can be formed, implying a saturating isotherm. While all four assumptions are not satisfied in real systems, the isotherm still provides a valid model for non-interacting adsorbates. The Langmuir model is derived from the chemical formula:

$$S^* + A \leftrightarrow SA \qquad (5.12)$$

Where S^* is an empty surface site and A is a molecule of adsorbate, and SA is a filled surface site. From this formula, the equilibrium constant,

$$K = \frac{[SA]}{[S^*][A]} \qquad (5.13)$$

The number of filled surface sites (SA) is proportional to θ, thus the number of unfilled sites, S^*, is proportional to $(1 - \theta)$, and the number of molecules (A) is proportional to the

pressure or concentration, in our case P_{vap}. Therefore, a new constant can be derived from the proportionalities and equilibrium equation,

$$\alpha = \frac{\theta}{(1 - \theta)P_{vap}}$$
(5.14)

which can be rearranged to the traditional Langmuir equation,

$$\theta = \frac{\alpha \cdot P_{vap}}{1 + \alpha \cdot P_{vap}}$$
(5.15)

The importance of P_{vap} now becomes clear, as it relates to the number of adsorbed molecules.

A second adsorption theory is necessary to describe situations where the Langmuir assumptions are not met. In 1938 Brunaur, Emmett, and Teller (BET) published a new isotherm model that allows for the gas molecules to interact, adding to the potential reactions described for Langmuir,

$$S^* + A \leftrightarrow SA$$
(5.16)

$$SA + A \leftrightarrow SA_2$$
(5.17)

$$SA_2 + A \leftrightarrow SA_3, \text{ etc…}$$
(5.18)

The BET theory makes a number of assumptions modified from Langmuir theory; 1) each adsorbed molecule can act as a bonding site for the next adsorbed molecule, 2) The uppermost layer of adsorbate has equal adsorption and desorption rates (in equilibrium with gas phase), 3) The heat of adsorption is the same for each successive layer, after the first, and 4) At P_{sat}, the isotherm tends towards infinity. The BET equation is expressed by,

$$\frac{1}{v\left[\frac{P_{vap}}{P_{sat}} - 1\right]} = \frac{c-1}{v_m c}\left(\frac{P_{sat}}{P_{vap}}\right) + \frac{1}{v_m c} \tag{5.19}$$

where v is the adsorbed gas quantity, v_m is the number of molecules in a monolayer, and c is the BET constant, given by,

$$c = exp\left(\frac{E_1 - E_L}{RT}\right) \tag{5.20}$$

Where E_1 is the heat of adsorption for the first layer, E_L is for each subsequent layer, and R is the universal gas constant.

A comparison of BET and Langmuir isotherms is presented in Figure 5.7 below. Typically, chemisorbed species follow a Langmuir model, while physisorped species follow the BET model.
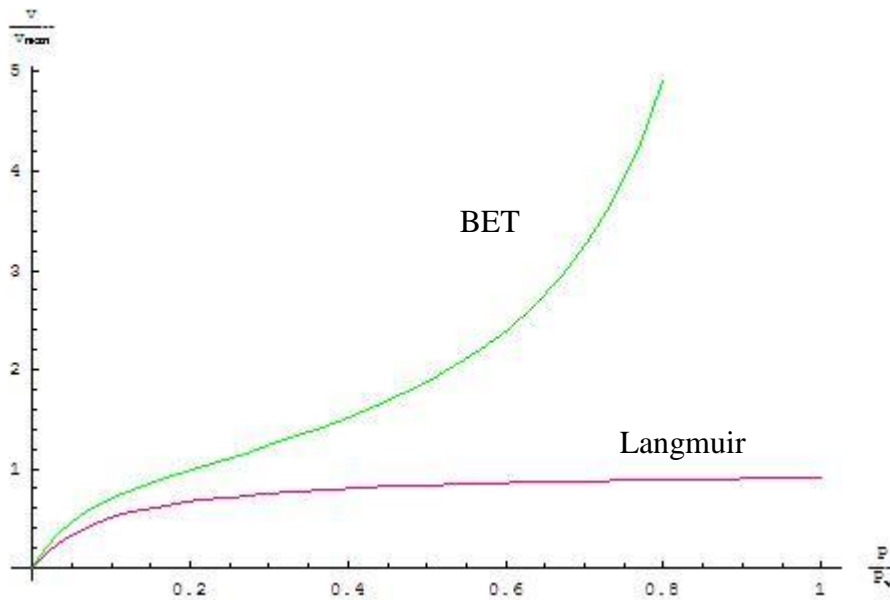
Figure 5.7. BET and Langmuir model isotherms modified from [109].

In this work, two vapor molecules are used, water and 1-pentanol. The properties of the candidate liquids to be vaporized are summarized in Table 5-1.

Table 5-1 Summary of VPL-pertinant properties

	density	surface tension	vapor pressure @ 20°C	molecular Weight	adsorption mechanism
Water	1000 kg/m^3	72.8 mN/m	2,338 Pa	18.3 g/mole	physisorption
1-pentanol	833 kg/m^3	25.7 mN/m	213 Pa	88.15 g/mole	chemisorption

To better understand the nature of the adsorption of water and 1-pentanol, their adsorption isotherms on silicon with a native oxide are presented below in Figure 5.8 and Figure 5.9, respectively.
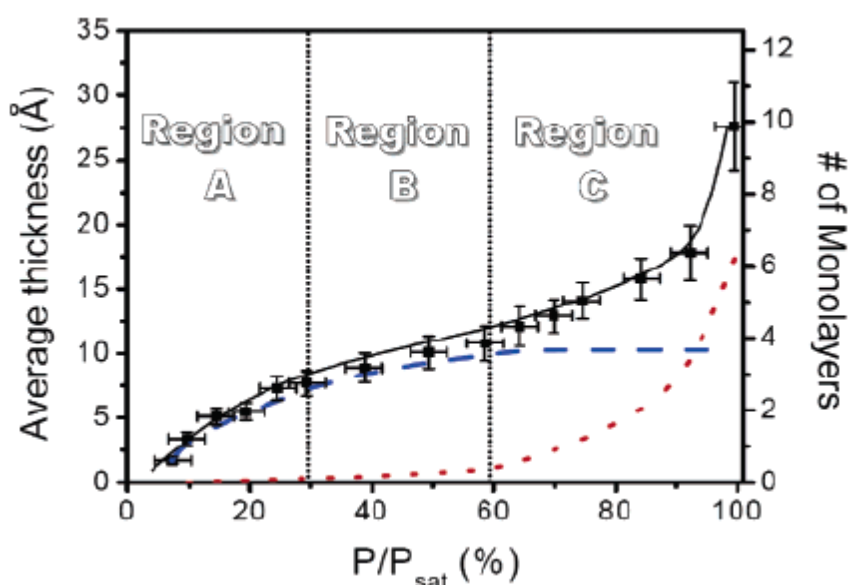
Figure 5.8. Adsorption isotherm for water on silicon, from [110]. The overal trend is shown in th black, solid line, while the individual contributions of ice-like structure and water-like structure are shown in blue and red, respectively.

The adsorption isotherm for water follows the BET model, which allows for water molecules to stack on one another. The paper from which this figure was taken describes three regions of adsorption for water: region A has an ice-like structure; region B represents a

transition to region C which has a liquid (amorphous) structure. The dashed blue line shows the growth and saturation of the ice-like structure, while the dotted red line shows the evolution of the liquid-like contribution to the structure.
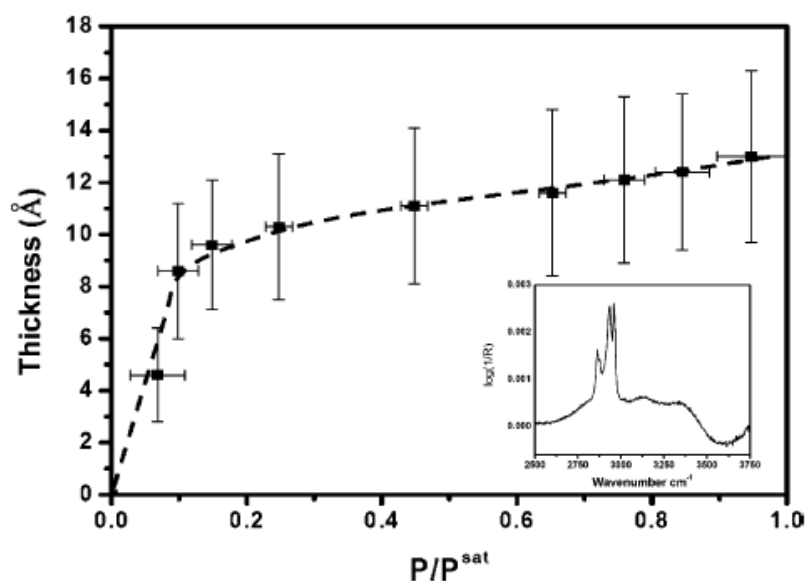
Figure 5.9. Adsorption isotherm for 1-pentanol on silicon with native oxide, from [45].

The isotherm for 1-pentanol differs significantly from that of water, as it follows the Langmuir model more closely. This is due to the fact that the 1-pentanol molecules have a low probability of forming multiple layers on the substrate.

It is important to understand the morphology of the adsorbed molecules to understand their isotherms and the role they play in reducing adhesion. The two adsorbed films are shown in Figure 5.10. Water initially forms hydrogen bonds to the exposed oxygen atoms on the surface of the natively-oxidized silicon substrate. The inter-atomic spacing is greater for the Si-O bond than the H-O bond in a water molecule, therefore the bond angle is stretched and an ice-like structure is realized. Additional layers form hydrogen bonds with the polar molecule, eventually relaxing into a more liquid-like structure. The surface is terminated with H atoms. The hydroxyl (-OH) group on the 1-pentanol molecule bonds to the substrate via

hydrogen bonding, leaving the hydrophobic alkyl group exposed. The alkyl group is non-polar, and therefore will not exhibit hydrogen bonding.
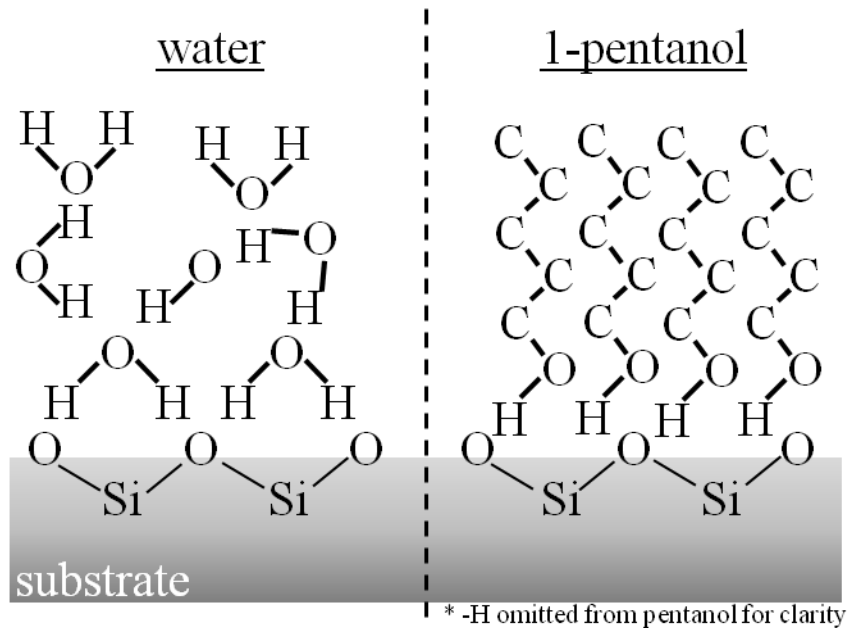
Figure 5.10. schematic representation of surface chemistry for adsorbed molecules

This dissertation is focused partly on proving rolling friction at the micro-scale has an adhesive mechanism between the ball and the raceways. Through experiments on contact area dependence (chapter 3) and wear mechanisms (chapter 4), it is hypothesized that this adhesion takes place through a series of Si-O-Fe bonds at the surface. As the ball rolls, torque can break the newly-formed bonds at this interface, or encourage crack propagation and growth on the surface of the ball. When using VPL, both molecules will completely coat the balls and the raceways. Two water molecules will come into contact during friction testing, and hydrogen bonding will occur between the counter-part molecules. The alkyl groups of the 1-pentanol molecules will come in contact when that vapor is introduced, and there will be weak van der Waals bonding. In both cases, the bonding between vapor molecules is significantly less than the covalent bonding between the steel ball and silicon substrate in the dry system.

Surface energy determines the available energy for a bond to take place. Table 5.1 shows that the surface energy values for water and pentanol are significantly different, with pentanol being lower. The lower surface energy of pentanol can be attributed to its surfactant-like properties, with the more reactive polar –OH bond adhering to surfaces, leaving the less reactive carbon chain exposed. Water will always have a hydrogen terminated surface, leading to a higher surface energy. Water was chosen to demonstrate the adhesive component of friction through the efficacy of VPL because of its high vapor pressure and ease of use. Pentanol will be utilized in future studies. In general, low surface energy, low density, high vapor pressure liquids are good vapor-phase lubricants.

5.2.2   Kinetics

The previous discussion dealt significantly with the equilibrium (time-independent) conditions of adsorption. The microturbine is a dynamic system, therefore the time-dependent adsorption kinetics are also important for successfully utilizing VPL. First and foremost, the rate of adsorption must be understood and shown to be orders-of-magnitude faster than any of the moving parts in the microturbine to prove that the replenishment rate of adsorbate far exceeds the rate it could be removed. The rate of adsorption R_{ads} per unit area can be defined as the product of impinging flux of molecules F and their probability of sticking to the surface S,

$$R_{ads} = F \cdot S \qquad (5.21)$$

The flux is further defined by the Hertz-Knudsen equation,

$$F = \frac{P_{vap}}{\sqrt{2\pi m k T}} \qquad (5.22)$$

where m is the mass of one molecule, and k is Boltzman's constant. P_{vap} once again becomes important. In the previous section, P_{vap} determined the thickness of adsorbate on a substrate. Here we see that P_{vap} also determines the rate at which the gas-phase molecules impinge upon a surface. The sticking probability, S, can also be defined as an equation of the Arrhenius form,

$$S = f(\theta)exp\left(\frac{-E_a}{RT}\right) \tag{5.23}$$

Where $f(\theta)$ is a function of the instantaneous surface coverage from the Langmuir definition (see eq. (5.15) above), and E_a is the activation energy for the adsorption event. S is highly dependent on the specific adsorbent/adsorbate system, and must be in the range $0 < S < 1$. It should be noted that this is the simplified treatment of the rate of adsorption, assuming the rate of desorption is very low, and $E_a(\theta)$ changes very little.

The flux of water molecules can be calculated at room temperature and saturated vapor conditions given the properties in Table 5-1. Assuming a sticking probability of 1 for simplicity, then all of the flux goes towards adsorption. The flux, given in molecules/m²s is,

$$F = \frac{2338\frac{N}{m^2}}{\sqrt{2\pi \cdot 18.3\frac{g}{mol}k \cdot 293K}} \tag{5.24}$$

$$F = 2.66 \times 10^{24}\frac{molecules}{m^2s} \tag{5.25}$$

The calculated area of the raceway within the microturbine used for these tests is 4.448x10^{-5} m², with a total of 5x10^{14} available sites. From Figure 5.10 above, we can see there is one water per available site, thus giving 8.5 µs to obtain a coated surface in the microturbine.

The mean-free-path (MFP) and velocity of gas-phase molecules can also help determine the rate at which vapor molecules can be replenished on a surface. The velocity of

a particle can be derived from *kinetic theory*, which defines the pressure of a gas in terms of the momentum transfer to the walls of the system, where,

$$P = \frac{Nm\overline{v^2}}{3V}$$ (5.26)

Where N is the number of molecules, m is the mass of a particle, and $\bar{v}$ is the average particle velocity. This can be plugged into a modified ideal gas law,

$$PV = NkT$$ (5.27)

And then $\bar{v}$ becomes,

$$\bar{v} = \sqrt{\frac{3kT}{m}}$$ (5.28)

The MFP is the average distance traveled by a particle between collisions. It can be derived from the average velocity of the particles, the size of each particle, and the density of particles in the system. The MFP, λ, is given by,

$$\lambda = \frac{kT}{\sqrt{2}\sigma P}$$ (5.29)

The elastic collision cross-section (σ) is,

$$\sigma = \pi d^2$$ (5.30)

At room temperature and atmospheric pressure, the MFP of a water molecule is on the order of 80 nm. The velocity for that same particle is 20 m/s. Solving for time, particles that are one MFP away from the surface of the sample will arrive in 4 ns on average. The calculations

above show that adsorbing a monolayer would take 8 μs initially and then 4 ns for replenishment, given vapor molecules are in the environment available for saturation. In comparison, the balls have a linear velocity of 2.67 m/s at 5,000 rpm and take 0.1 s to make contact with the area the previous ball was occupying. The actuation of the turbine and the mean free path are linked to the system pressure. Using these relationships, a prediction of the time constants for a ball to enter the contact area of the previous ball and the replenishment time are offered in Figure 5.11.
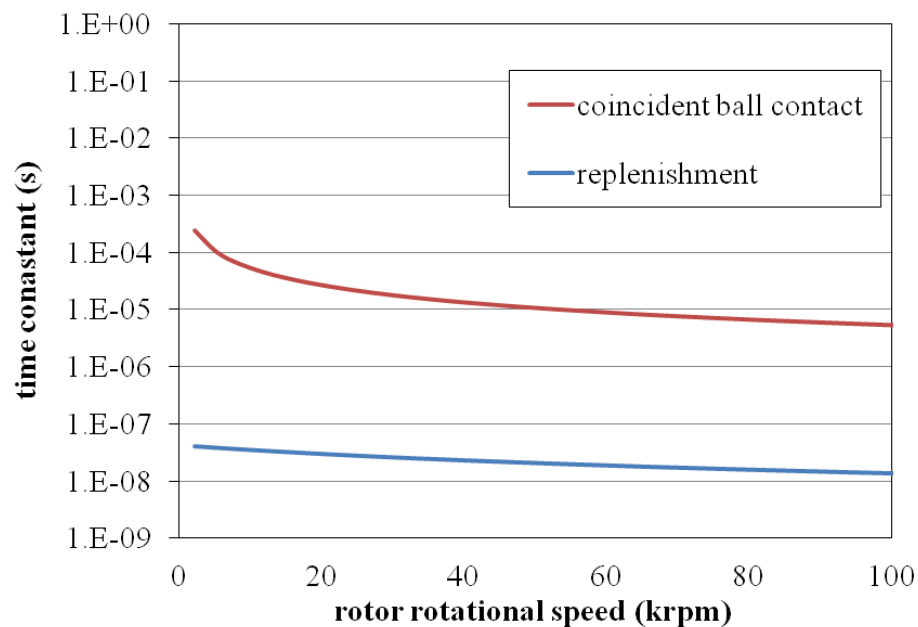
Figure 5.11. Calculated time constants for replenishment

The turbine rotational speed was calculated from previous testing. The replenishment time was calculated using the ratio of MFP to average particle velocity. While this is a rough estimate, it confirms that, regardless of pressure, the replenishment of lubrication will take place three orders-of-magnitude faster than it can be removed by the rolling balls.

5.3   Results and Discussion

The initial results were performed as a proof-of-concept experiment, using just the bubbler, no condenser, and no attempt at relative humidity control or measurement. A silicon microturbine (rotor diameter=10 mm, ball = 500 μm diameter 440C stainless steel, 95% loading) was used as the first test device, with water as the vapor lubricant. Figure 5.12 shows the turbine performance testing using dry and vapor lubricated actuation gas. Performance testing methodology is discussed in chapter 4.
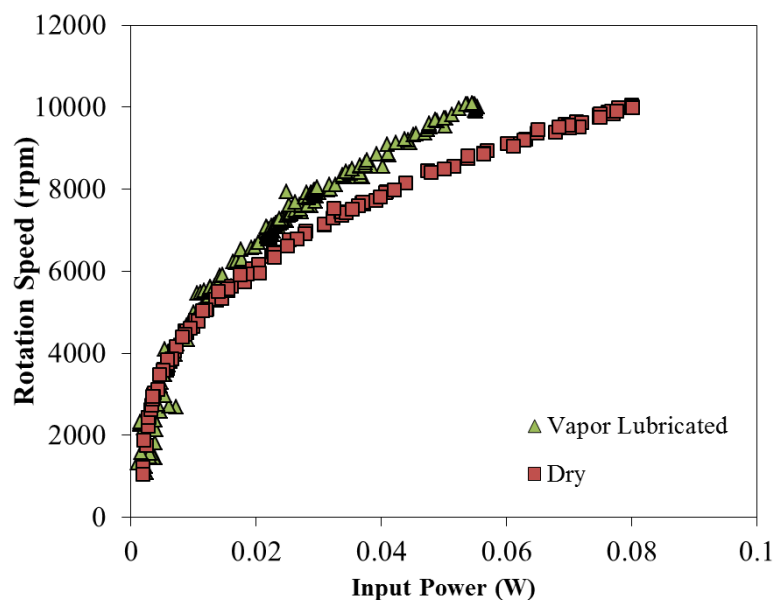
Figure 5.12. Performance testing done with dry and vapor lubricated actuation gas. Less input power for an equivalent speed represents reduced friction.

The use of vapor lubrication resulted in a 37% decrease in input power to reach 10 krpm versus operating with dry nitrogen. The error in this measurement is greater than previous performance testing, though, because the density of the actuation gas is reduced for vapor saturated nitrogen and the performance testing methodology includes both bearing frictions aspects and turbine efficiency influences. The reduced gas density would result in a turbine that *underperforms* compared to the normal gas density; therefore the benefit of vapor lubrication is even greater than it appears. The exact relative humidity of the vapor was not

measured at the time of the experiment, but the value can confidently be placed between 40-70% RH, knowing the pressure and configuration of the set-up at the time.

Spin-down friction testing does not include any aspects of turbine efficiency, so it is a higher fidelity friction measurement tool. Spin-down tests were performed with dry and vapor lubricated gas on the same microturbine that received the performance testing. During the spin-down test, thrust-side flow is provided to the microturbine rotor constantly to provide normal load. This constant flow through the bearings allows for the VPL to be constantly replenished.
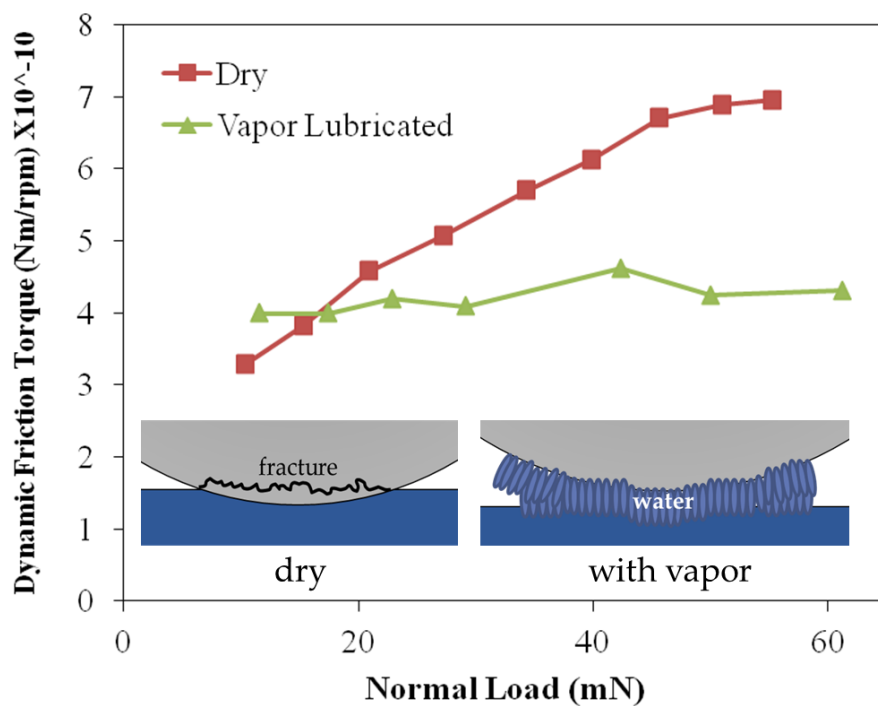
Figure 5.13. Spin-down friction testing performed with dry and vapor lubricated carrier gases. Inset schematic describing the different mechanisms of contact for the two situations.

It is shown in Figure 5.13 that VPL provided a two-fold benefit. Firstly, friction torque was significantly reduced for rotor loads above 20 mN, which is likely the reason enhanced turbine performance was observed. Secondly, and more importantly, the introduction of VPL fundamentally changed the relationship between friction torque and normal load. As stated in the introduction, VPL was chosen to specifically address the adhesive component of micro-

scale rolling friction, while not affecting the system dynamics or mechanical properties. If, for example, elastic hysteresis was the significant contributor to rolling friction, then VPL would have little effect. The friction torque curve flattened out towards the "b" (load-independent) contributions discussed chapter 3. The b value represents the minimum value of friction torque possible within the microturbine, dictated by gyroscopic, viscous, and other forces. This result is the best support for the adhesion-dominated rolling friction hypothesis so far.

Spin-down friction testing was then performed within a humidity controlled system so that the variation of friction torque with relative humidity could be explored. Humidity control was obtained through the tuning of system pressures and temperatures, as described in section 5.2. Water adsorption follows the BET isotherm, which implies that multiple layers of water molecules stack on top of one another depending on the partial pressure of water vapor in the atmosphere above the adsorbate. Asay, et al., described three regimes of water morphology when adsorbed on the surface of silicon, shown in Figure 5.8, [111]. Relative humidities used for spin-down testing were chosen to be within each regime, at 18% RH, 48% RH, and 88% RH. Figure 5.14 shows the results of the spin-down testing at various relative humidities.
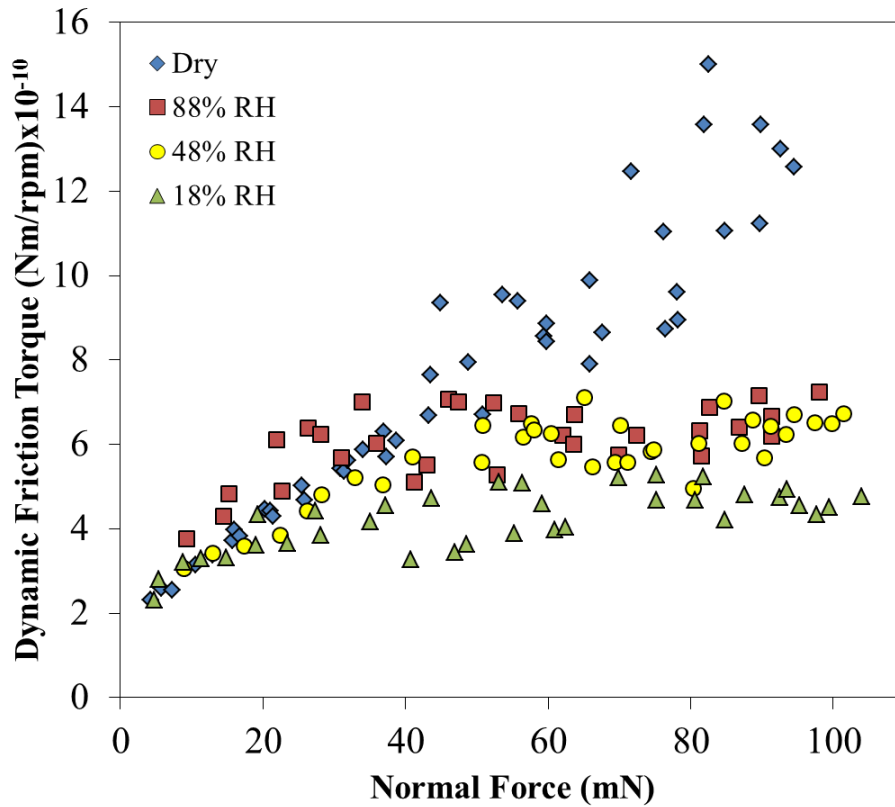
Figure 5.14. Spin down friction testing through a range of different relative humidities.

The observed friction torque is the lowest at the lowest tested relative humidity, not counting the dry case. As humidity increases, so does friction torque. This result is in agreement with other studies on the adhesion and pull-off forces of contacting objects under various relative humidities [112, 113]. In these studies, there is a positive linear relationship between adhesion and RH, with increasing capillary forces causing stronger adhesion at higher levels of RH. The dry case is discontinuous from this trend, as it represents a significantly different bonding regime (covalent), compared to van der Waals or hydrogen bonding in the lubricated conditions.

5.4   Conclusion

This chapter was focused on altering the surface energy of the microball bearing system without changing the overall properties of the system through the utilization of

adsorbed surface layers. The surface-energy altering surface layers were delivered through a custom VPL system. By specifically addressing surface energy, the influence of adhesion on friction torque can be determined independent of other factors such as the effect of elastic hysteresis. These experiments combined with the contact area study from chapter 3, which showed that friction increased with increasing contact area, and the wear experiments, which showed adhered ball material as the primary wear mechanism, all help support the adhesion-dominated friction hypothesis.

The fundamentals of vapor phase lubrication have been discussed within the context of the experiments. Pressure relations to chemistry and temperature have been explored and applied to the conditions of the VPL introduction apparatus. To this end, the experimental platform has been explained in a thermodynamic sense. The relationship between the morphology of adsorption and pressure was explored.

Once an understanding of adsorption has been established, spin-down friction testing was performed on multiple microturbines and used to show the efficacy of vapor phase lubrication. The major result was the discovering the relationship between friction torque and normal load is significantly altered with the addition of VPL, suggesting that adhesion is a dominant factor in micro-scale rolling friction. Multiple levels of RH have been saturated within the carrier gas and used to actuate the microturbine, providing insight as to the quality and nature of adhesion.

Microball bearing systems employed in the future need to focus on ways to minimize the surface energy. VPL is a good candidate because its low capillary forces, efficacy (as shown in this chapter), and high-temperature compatibility. This first challenge will be determining the ideal liquid (or solid) to vaporize. As discussed in section 5.2, liquid pre-vaporization should have a high vapor pressure for ease and speed of delivery, and low surface energy to minimize friction. An obvious challenge remains though in the engineering

of VPL systems within micro-scale packages. One would need a reservoir, a heating element, and a flow source. In the case of tested microturbine, the VPL system had to accommodate pressures in excess of 20 PSI, whereas a non-air driven device could have a low-pressure impingement of VPL flow. The speed, desired lifetime, and packaging volume will ultimately determine of VPL could be used in a real-world application.

6. Isotropic Etching for Groove Geometry Raceways

Nomenclature

F_c	centripetal load
F_N	normal load
l'	lateral etch rate
r_b	ball radius
r_c	contact radius
r_H	housing radius
r_R	rotor radius
r_1	arbitrary parallel radius
m_b	ball mass
θ_c	contact angle
t	time
v'	vertical etch rate
x_m	mask opening width
ω_b	ball angular velocity
ω_R	rotor angular velocity
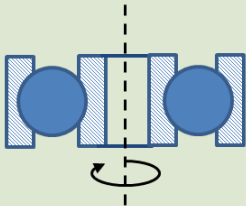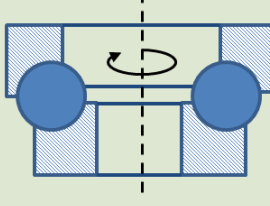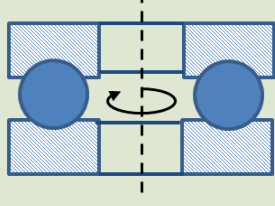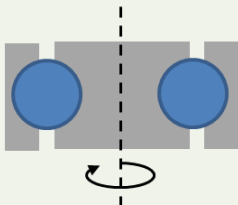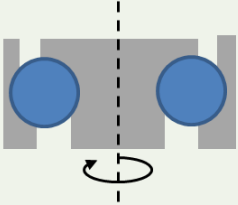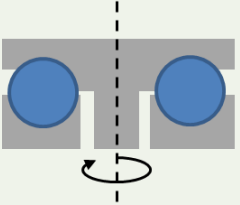
6.1   Introduction

Rolling bearings are an essential component of modern machinery, providing low friction and wear contact between moving parts. Specialized bearings are employed depending on their specific application, based on load, speed, and geometric requirements. Rolling bearing technology has been extended to the realm of micro-electromechanical systems (MEMS) in the demonstration of high-performance linear and rotary micromachines. Proof-of-concept demonstrations of micromotors [2], microturbines [6], micropumps [1], and microgenerators [114], supported on microball bearings have all relied non-ideal planar geometries for their bearing raceways. Ghodssi *et al.* recently showed that future microfabricated bearing systems will need to accommodate for actuation-induced axial loads as well as inertia-induced radial loads, and will therefore require circular cross sectioned bearing structures to handle the resultant load for high-speed microball bearing systems [115]. This chapter describes the development of a 3D etching technique used to obtain

uniform, circular cross-sectioned bearing raceways and their demonstration in a next generation rotary microsystems, allowing for high-speed operation.

Macro-scale ball bearing systems can be categorized into three types by their desired maximum operating speed and load: thrust, angular, and radial ball bearings. Each design is ideal for a specific ratio of axial to radial load, which is manifested in the bearing as the contact angle between the ball and the raceway. Contact angle will be discussed in detail in subsequent sections. It should also be noted that radial load capacity is analogous to maximum operating speed, as radial load is derived from centripetal forces. Table 6-1 compares and contrasts the three different types of ball bearings.

Table 6-1 A comparison of ball bearing types and operating conditions.

Type:	Radial	Angular	Thrust
Macro-scale:			
Micro-scale: (imagined)			
Axial Load	Low	Medium	High
Radial Load (max. speed)	High	Medium	Low
Contact angle (est.)	0-20°	40-60°	70-90°

Deep-groove thrust bearing

Each of the variations shown in Table 6-1 utilizes circular-cross sectioned raceways to allow for a range of contact angles. In fact, *all* macro-scale ball bearing systems use circular cross sectioned raceways. The micro-scale versions of each type are initial schematics, although micro-scale angular bearings are discussed in the future work within chapter 8. For the first demonstration of the microfabricated circular geometry, a subset of thrust bearings was selected: deep-groove thrust bearings. The deep-groove geometry, described in section 6.2, is a middle-ground in operating regimes between thrust and angular type systems. The deep-groove geometry also had the most overlap with previously demonstrated thrust bearing fabrication schemes, so it was selected as the first demonstration platform for the isotropic etch process.

Future microball bearing utilizing systems, such as a microgenerator, will require high speeds and therefore the ability to accommodate for high radial loads. The top-down fabrication style of MEMS will dictate that the actuation mechanism, be it electrostatic, electromagnetic, or pneumatic will impart an axial (through wafer) load on the bearings. The centripetal force acting on the rotating balls will impart radial load scaling with *velocity^{2}*, therefore radial forces on the ball bearing will need to be accounted for in addition to the thrust load. In current designs, radial load is not supported, therefore there is a maximum operation speed for a given normal load. To accomplish high-speed operation, a circular raceway cross-section is imagined. A schematic of the rectangular and deep-groove bearings can be seen in figure 6.1.

(a)

stator   rotor

(b)   (c)

stator   rotor   Axis of rotation   rotor
                                              stator

F_{radial} F_{radial}
ball   ball
              F_{axial} F_{axial}

rectangular bearing   Axis of rotation   circular bearing
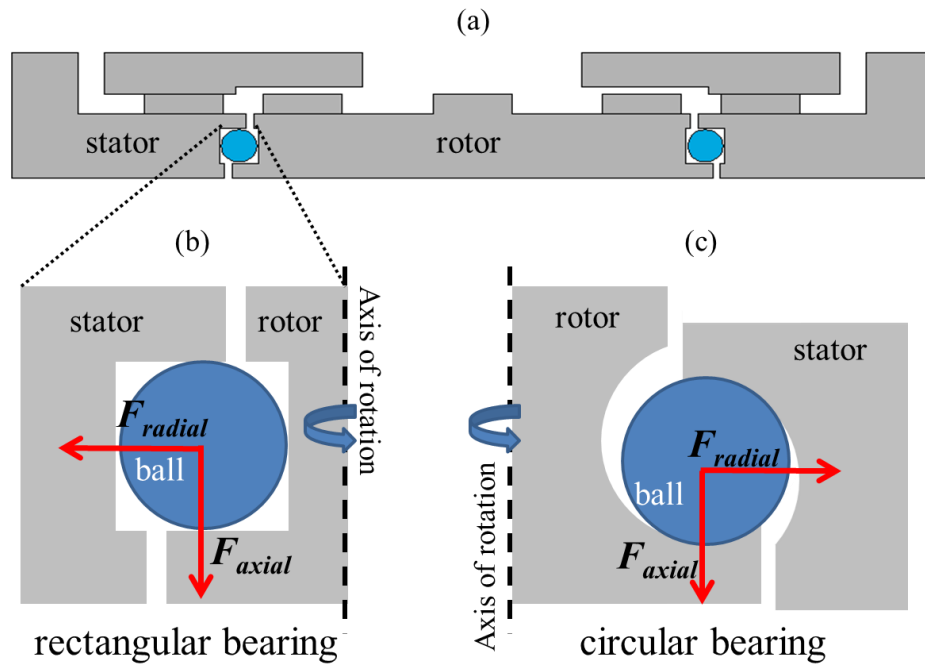
Figure 6.1. Comparison of bearing geometries. (a) schematic of microturbine to show location of bearings (b)rectangular cross-section bearing defined by DRIE and used in previous microball bearing devices. (c)circular cross-sectioned bearing developed using custom isotropic etching techniques.

The bearing in Figure 6.1a has been used in various microsystems including pumps, generators, motors, and turbines, and has shown consistent operation over 200 million revolutions at 10 krpm [46] and brief operation up to 87 krpm [1]. An ultimate limiting factor in the operation of a device with the rectangular geometry is the lack of ability to accommodate significant radial load. At low speeds the friction forces between the ball and raceway are capable of restricting the ball radial motion. At high speeds, the centripetal forces overcome the friction forces and the ball begins to make significant contact with the outer wall. The rotor then begins to wobble significantly, ultimately resulting in failure. This concept is discussed theoretically in chapter 2 and measured experimentally with on-chip accelerometers in chapter 7.

The bearing geometry in Figure 6.1b closely resembles the geometry used in macro-scale deep groove bearings, and has the capability to maintain contact with the ball under combined thrust and radial loads. The general shape of the raceway represents the middle ground between the ideal bearing geometry and the capabilities of microfabrication. The following sections will discuss the design and fabrication of a circular cross-sectioned raceway, the ball bearing dynamics within the circular geometry, and demonstration of the bearing utilized within a microturbine system.

The focus of this experiment is two-fold: the development of a unique isotropic etching technique to obtain the circular raceway cross-section and the design and demonstration of a microturbine supported on microball bearings utilizing said raceway. This cross section is realized by etching semi-circular cross sections into the surface of two mirrored wafers and then bonding them together. Obtaining semi-circular etching cross-sections required the development of a unique multi-step plasma process with tuned parameters such as power and pressure. Once the technique was demonstrated with acceptable geometries, the isotropic etching was employed within a custom fabrication flow to create the first microfabricated device with 3D bearing structures.

6.2   Bearing Design and Dynamics

Multiple silicon microturbines with deep-groove raceways have been designed and fabricated to serve as the proving platform for the circular cross-sectioned raceways. The variations of microturbine geometries tested in this chapter are summarized in Table 6-2. Two rotor diameters were chosen, 2.5 mm and 5mm, both utilizing 0.5 mm balls, giving rotor:ball diameter ratios of 5:1 and 10:1, respectively. Previous microball bearing devices had rotor:ball ratios of 35:1, whereas macro-scale bearings utilize 3-5:1 ratios to minimize

the centripetal load imparted by the balls. Stainless steel and silicon carbide balls have been utilized because of their different densities and surface properties.

Table 6-2 Microturbine variations

Rotor radius	Ball Material	# of balls
2.5 mm	Steel	15
	SiC	
5 mm	Steel	30
	SiC	

The microturbine presented herein, as well as any number of rotary MEMS devices utilizing ball bearings in circular raceways can be fabricated using the scheme presented in Figure 6.2. The microturbine is comprised of two wafers, bonded together encapsulating the ball bearings using a technology described in chapter 2, except with a new set of geometry-specific shadow masks. The outer surfaces of the wafers contain the turbine structures patterned in a silicon dioxide hard mask for later use (Figure 6.2a). The inner surfaces of the wafers contain the raceways defined in Figure 6.2. Fabrication scheme for rotary MEMS with circular raceways.b and isotropically etched in Figure 6.2c. The raceways also contain offset release structures that are defined by spray coat lithography and etched with DRIE to be accessed later (Figure 6.2d). Bond alignment structures are also defined and etched during the spray-coat process on the inner surface of the two wafers. A shadow-masked evaporation of eutectic gold/tin is deposited on the inner surfaces of the wafers. Microball bearings are then placed in the etched raceways and the two wafers are bonded (Figure 6.2e). Finally, the

silicon dioxide hard mask patterned in Figure 6.2a is utilized as a DRIE etch mask and the outer surfaces are etched make contact with the release etches, thereby releasing the rotor from the stator portions of the chip (Figure 6.2f).
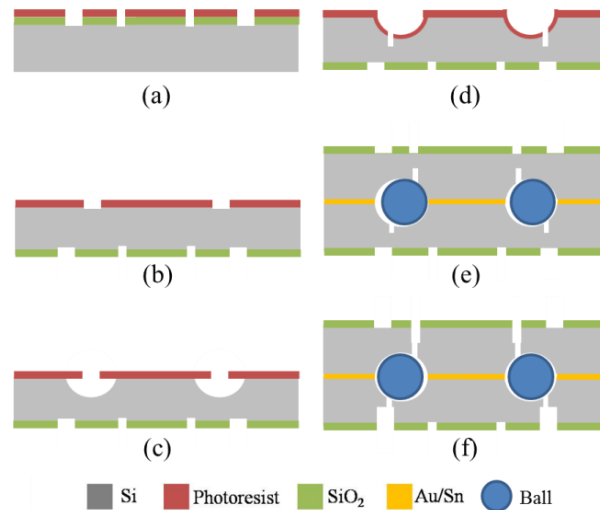
Figure 6.2. Fabrication scheme for rotary MEMS with circular raceways.

The most critical aspects of the fabrication are the geometry of the raceway and the location of the offset release etches. The etching techniques developed in this paper set forth the fabrication guidelines for obtaining circular raceways with rotor diameters from 1mm-10mm. The location of the offset release etch depends on the radius of the raceway, the geometry of the rotor, the expected centripetal load from the desired operating speeds, and the amount of thrust load tolerable. The resultant of the vector sum of radial and thrust loads gives the contact angle between the ball and raceway. The offset release etch trench on the thrust (non-turbine structured) side of the rotor is radially further from the axis of rotation than center of the raceway. At increasing speeds and centripetal load the balls will push out radially, towards the thrust side release etch structures. The release should therefore be offset as much as possible until the point where it is so far offset that the rotor is no longer held into position by the balls and could be completely removed from the stator. A maximum allowable contact angle of 37° was selected based upon the contact area of the ball and the

140

desired operating parameters. This angle then determines the maximum operating speed for a given normal load. The contact angle can be calculated from equations (6.1-2).

$$\theta_c = \arctan\left(\frac{F_N}{F_c}\right) \qquad (6.1)$$

Where θ_c is the contact angle, F_N is the normal (axial) load, and F_c is the centripetal load, defined by,

$$F_c = m_b r_R \omega_R^2 \qquad (6.2)$$

Where m_b is the mass of the ball, r_r is the rotor radius, and ω_r is the rotor speed. The contact angle has been simulated for a range of speeds and normal loads in Figure 6.3, based on the bearing variations outlined in table 6-2. Pure thrust and pure radial bearings are represented by 90° and 0° ,respectively. The simulation highlights the significantly reduced rotor normal loads needed to maintain the allowed contact angle for high speed operation.
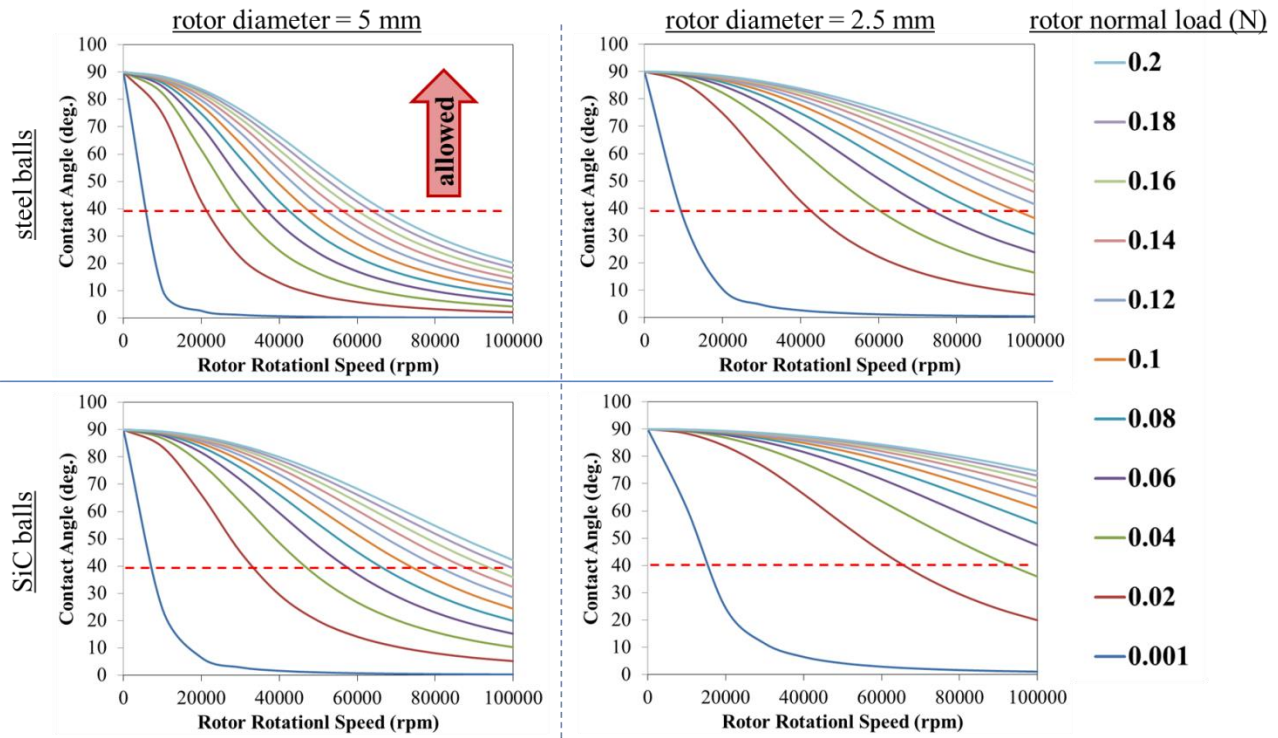
Figure 6.3. Numerical simulation of contact angle for various loads and speeds amongst the four bearing variations.

Figure 6.3 highlights the benefits of using smaller radii and less dense balls. In both of those cases, it requires significantly less normal load to operate at a given speed with a contact angle above the 37° geometrically defined maximum. A maximum rotor normal load of 200 mN was selected for the simulation, which equates to 250 MPa contact pressure beneath the ball. This contact pressure is well below the predicted 450 MPa found in chapter 4 to result in fatigue-based raceway fracture. As a point of comparison, >600 mN normal load is required on the rectangular geometry thrust bearings to operate at 60 krpm. Using a 5 mm rotor and stainless steel balls, the required normal load is reduced to 180 mN, and with a 2.5 mm rotor and SiC balls, the normal load required is below 20 mN.

6.2.1 Bearing Dynamics

The geometry of the bearing presented herein could be categorized as a deep-groove thrust bearing. On the macro-scale, these bearings are used to accommodate primarily thrust loads at moderate speeds. As the contact angle decreases towards the horizontal (0°) the style of bearing transitions from thrust to an angular contact to a radial bearing. This transition is due to the need for the axis of rotation of the ball and the contact angle (from the axial and radial load vetors) being nearly perpendicular in the ideal case. Of these bearing types, a radial bearing-style would be inappropriate for a microfabricated ball bearing system because of its inability to accommodate the inevitable thrust loads imparted by on-rotor actuation schemes. An angular bearing would be ideal, but the machining tolerances required to create one using microfabrication are not currently obtainable. Specifically, the ball would need to be press-fit into the angular bearing system, so uniformity and geometry would need to be on the single micrometer level. Therefore a deep-groove thrust bearing orientation is utilized as a middle-ground between the ideal geometry and realistic fabrication capabilities, at the expense of bearing performance.

A schematic of the bearing during operation is presented in Figure 6.4. This figure highlights the worse-case scenario when the thrust and radial loads give a near 37° contact angle.
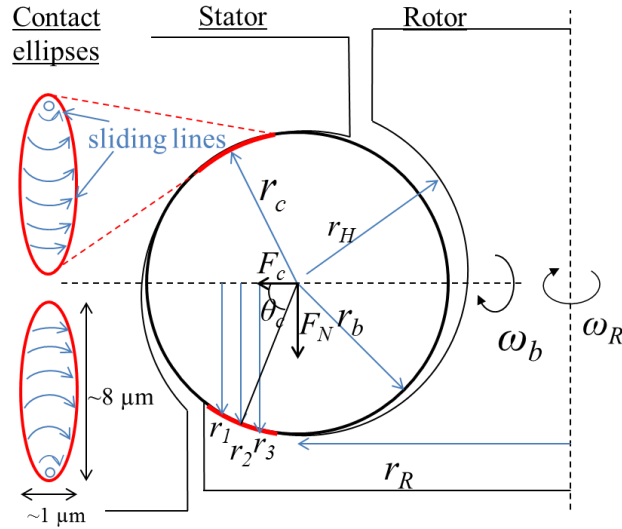
Figure 6.4. Bearing Dynamics Diagram

The contact angle, defined by the vector sum of the radial and axial load components is ideally perpendicular to the ball axis of rotation. When they are perpendicular, the center of the contact ellipse experiences pure rolling, and progressively higher magnitude sliding takes place radially outward from center of the contact area. As the contact angle increases, the center of the contact ellipse moves away from the point of pure rolling, and the ball undergoes more sliding. The velocity of the sliding can be calculated from the angular velocity of the rotor and geometry, where:

$$\omega_b = \frac{1}{2}\frac{r_b}{r_R}\omega_R \tag{6.3}$$

From the angular velocity calculated in eq. (6.3), the linear velocity of a parallel at radius r (from Figure 6.4. Bearing Dynamics Diagram) can be calculated according to equation (6.4),

$$V_{r_{1,2,3}} = \omega_b r_{1,2,3} \tag{6.4}$$

144

It should be noted that there is also sliding induced from gyroscopic effects, which are not accounted for in this analysis. The gyroscopic forces on the microball bearings were found to be minimal in the rectangular bearing [93]. It is unclear the magnitude of the detrimental effect of the geometry-based sliding effects, but it is shown to be significant from the observed raceway wear, discussed in a following section.

The efficacy of the deep-groove bearing is determined by monitoring turbine performance. A custom package was designed to deliver high flow rates (>10 SLM) while monitoring input pressure and thrust load with integrated pressure transducers and turbine speed via a tachometer-style optical displacement scheme. A picture of the packaged microturbine is provided in Figure 6.5.
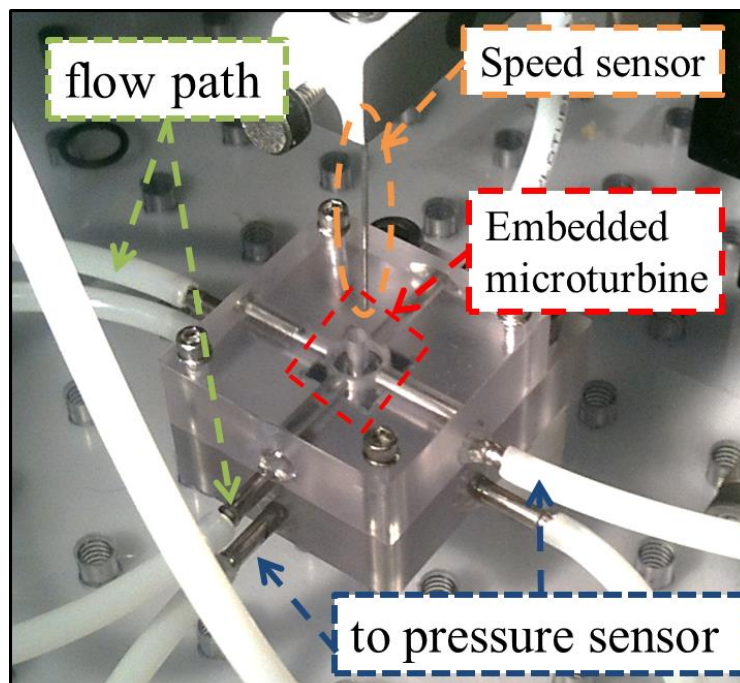
Figure 6.5. Photograph of packaged microturbine under test.

The packaging directs flow through the turbine actuation structure. During operation, some flow is allowed to leak through the backside of the device, allowing for normal load control. The package also includes ports to pressure sensors and an optical displacement sensor used

to measure speed. The bearings are analyzed post-mortem using scanning electron microscopy and vertical scanning interferometry to determine the governing wear regimes.

6.3   Etch Development

6.3.1   Isotropic etching development

Microfabrication technology uses an array of techniques to obtain characteristic isotropic etching profiles. These techniques include wet etching in an HNA solution or dry techniques, including XeF_2 chemical etching, or SF_6 plasma-based etching. Inductively-coupled plasma (ICP) based techniques were chosen based on a review of the current state of the art technologies in section 1.4.4. ICP etching provides both a physical etch via ions accelerated from the plasma sputtering the substrate and a chemical component based on the well characterized fluorination of silicon through the SF_6 – silicon interaction [116, 117].

A two-step ICP process was chosen as the methodology to obtain the circular bearing cross-sections. In the two-step isotropic etch a bulk of the material is removed in the first etch and the depth and curvature are almost fully realized. The second etching step is used to remove the re-entrant silicon from beneath the masking material, ultimately widening the raceway and slightly affecting the curvature. A visual representation of the evolution of the two-step etch process is provided in Figure 6.6. A similar process was first described by Larsen in [81] used to make batch-fabricated micro-lenses with good geometric control.
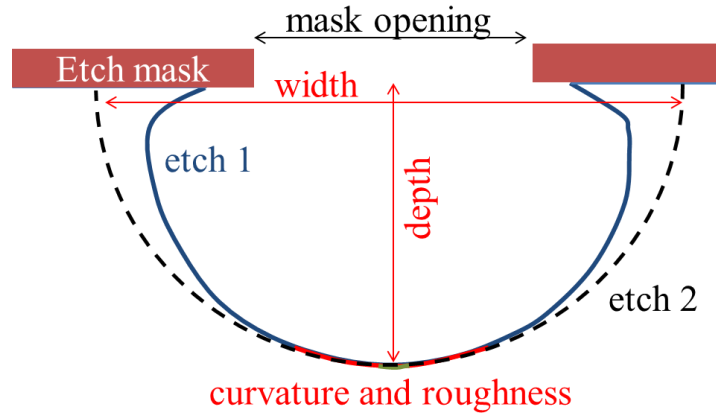
Figure 6.6. Graphic representation of the raceway profile during the two-step etching process. Geometric parameters of interest are highlighted.

The important geometric characteristics of the bearing are depth, width, and curvature as well as minimizing surface roughness and maximizing etch uniformity across the raceway and across the wafer. The parameters chosen to tune within the ICP process are RF plate power, chamber pressure, and etch time. The plate power applies a bias between the plasma and the substrate, acting on the ions from the plasma and giving the etch directionality. The chamber pressure principally affects the mean free path of an ion in the plasma, with lower pressures providing longer paths, and thus higher energy ions. Finally, it was found that the etch rates were non-linear, so the evolution of the etch was studied with time-resolved etching. Initial conditions for the custom etch were derived from the stock etching step within a DRIE recipe.

6.4   Results and Discussion

6.4.1   Isotropic Etching

The isotropic etch experiment took place in three distinct phases: designing the proper etch mask geometry that results in a nearly semi-circular raceway etch, determining the exact etch parameters necessary to obtain the proper width, depth, and curvature with minimal

147

roughness, and performing a time-resolved study to determine etch rates and integrating it in the microturbine fabrication flow.

The design of the correct masking geometry was the first challenge of the isotropic etching study. The mask required opening (x_m) can be estimated from the vertical and lateral etch rates given equations (5-7) below,

$$r_H = v't \qquad (6.5)$$

$$r_H = l't + 0.5x_m \qquad (6.6)$$

$$x_m = 2t(v' - l') \qquad (6.7)$$

Knowing that the ball radius is 250 μm, the raceway housing radius (r_H) can be estimated to be 260 μm at minimum. In the two-step etch process; the depth is defined in the first etching step so the time, *t*, can be estimated from equation (6.5) only. Vertical (*v'*) and lateral (*l'*) etch rates were assumed to be 3.6 μm/min and 2 μm/min, respectively. Substituting the time, radius, and etch rates into equation (6.7), one obtains a mask opening of 230 μm. Because the second step in the two-step process widens the raceway without significant etching vertically (refer to figure 6.6), the mask opening experiments were adjusted to be centered on a 200 μm opening.

Test structures were etched using a non-optimized two-step etching process to help understand the evolution of the general shape of the raceway for different mask openings. The first isotropic etch was performed with a 10 μm *AZ9260* photoresist etch mask. The second isotropic etch was performed on the wafer after the removal of masking material in an ultrasonicated acetone bath. The shape ratio, defined as the ratio of etch radius (lateral distance from center of mask opening to edge of etch) to etch depth, where 1 is a semi-circle, was tracked over a range of mask openings in Figure 6.7.
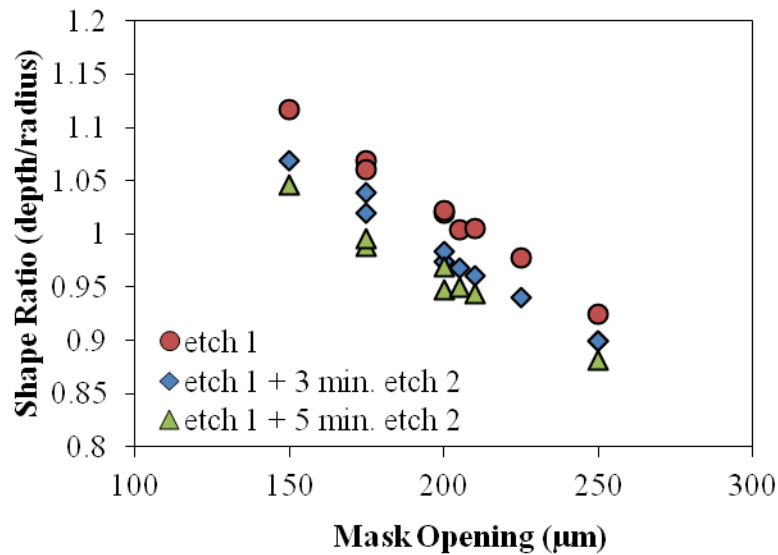
Figure 6.7. Shape ratio for different mask openings after successive etching steps.

The mask opening data suggests that an opening of 200-215 µm is sufficient to give a semi-circular cross-section with a radius of 260-280 µm, and was therefore selected as the opening for future isotropic etching experiments. It should be noted that the mask opening was chosen to err on the side of being slightly wider than a perfect circular cross section so as not to inadvertently create a raceway too narrow for the ball.

Once the mask opening was determined, the bulk of the experiment was focused on the careful manipulation of *etch 1* plasma parameters in order to finely tune the raceway geometry. As discussed earlier, the plasma properties of interest were primarily the chamber pressure and RF plate power. Eight identical wafers were prepared with arrays of test raceways patterned with photolithography in 10 µm-thick *AZ9260* photoresist. Each wafer was etched for 65 min. to obtain near final dimensions. Table 6-3 presents the pertinent etch conditions and the resulting parameters.

Table 6-3 Parametric *Etch 1* study

Universal Parameters					
Plate power (W)	Chamber pressure (mTorr)	RF coil power (W)	Plate temp (ºC)	SF$_6$ flow (sccm)	Ar flow (sccm)
variable	**variable**	850	30	100	40
Process			**Geometric Parameters**				
Recipe	Plate power (W)	Chamber pressure (mTorr)	Vertical rate (µm/min)	Lateral rate (µm/min)	Roughness (RMS µm)	Curvature (µm)	Etch selectivity
1	6	22	3.6	2.0	>0.02	524	95.4
2	8	22	3.7	2.1	>0.02	518	84.8
3	10	22	3.7	2.0	>0.02	512	75.9
4	12	22	3.8	2.0	>0.02	516	64.2
5	14	22	3.7	1.9	>0.02	368	41.5
6	16	22	3.7	2.0	>0.02	352	39.9
7	12	27	4.0	2.3	0.11	532	87.9
8	12	17	3.4	1.8	0.14	422	35.2

Recipes 1 through 6 were etched at a constant chamber pressure with variable RF plate power. The principle difference amongst them is the curvature of the bottom of the raceway and the selectivity of etching the substrate versus masking material, which is important for designing a final fabrication process flow. Varying the RF plate power will change the strength of the electromagnetic field that directs the plasma ions to the surface of the substrate. In general, the ICP etching mechanism is a combination of chemical etching from the fluorination and subsequent volatilization of silicon, and physical etching from the sputtering of surface atoms by plasma ions. The range of plate powers tested (6-16 W) is not expected to produce ions with enough energy to overcome the 4.62 eV binding energy of

silicon. This implies the etch process here is purely chemical and explains the consistent etch rates observed in the system, e.g., if higher plate powers increased the etch rate, then there would be some physical etching mechanism at play. The significant change in selectivity, however, shows that the masking material does undergo physical sputtering, and is therefore less effective at high plate powers. The reduction in curvature at higher powers can be explained by the enhanced density of ions delivered to the bottom of the trench versus the sidewalls by the increased directionality of the ion paths. It should also be noted that sample 4 served as the recipe for the mask opening relationship study and was utilized as the baseline for the parametric study.

Chamber pressure was compared amongst recipes 4, 7, and 8. The physical implications of chamber pressure are complicated because of the competing effects of plasma density and a change in the mean-free-path (MFP) of the plasma molecule. Longer MFP ions travel further without a collision at lower pressures versus higher pressures, implying that the ions will have slightly more time to accelerate and will therefore hit the surface with a higher energy. Higher pressures may reduce the mean free path, but increase the plasma density and therefore the number of reactive species on the surface. Based on the etch rates from (6.6-7) the increased plasma density accelerated etching. The diameter of curvature obtained ranged from $422 - 532$ μm as pressure was raised from $17 - 27$ mTorr, which is expected based on the reduced directionality of ions in higher-pressure plasmas. The surface roughness was significantly affected by the change in chamber pressure, with both high (27 mTorr) and low (17 mTorr) pressures significantly increasing the surface roughness. At high pressures, ion bombardment energy is reduced due to the shortened mean free path; therefore the roughness will be dictated by enhanced chemical etching. At low pressures, ion bombardment energy is higher; therefore the surface roughness is likely due to enhanced physical etching. Minimum roughness is obtained when the chemical and physical etches are tuned properly. A similar

relationship with chamber pressure and roughness was observed by Chen in his thesis work on ICP etching [118].

Etch 2 was a blanket etch, taking place after the masking material was removed post-etch 1. Etch 2 was used to target the re-entrant edges left after etch 1(see Figure 6.6), which are selectively etched due to their high surface area compared to the surface of the wafer and the semi-circular raceway. A comparison of the etch rates of two blanket etches is presented below in Figure 6.8.
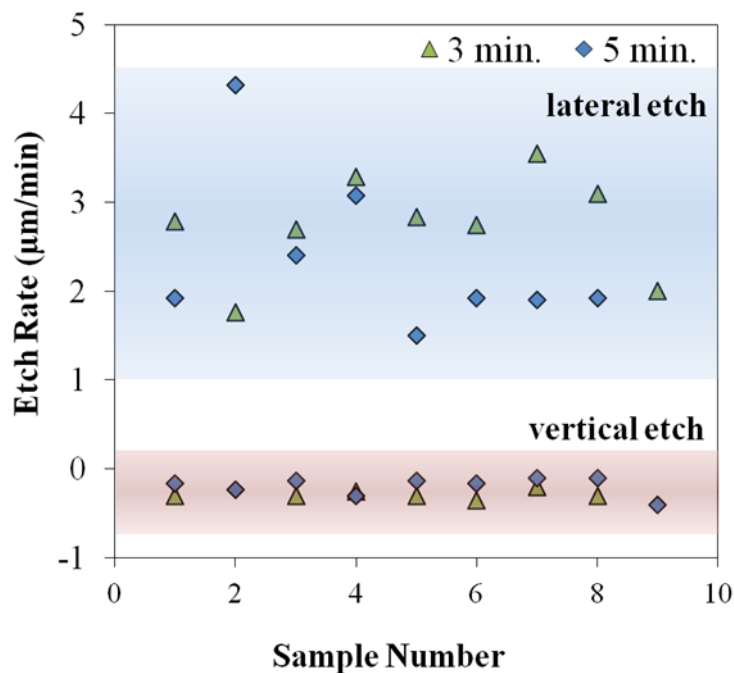
Figure 6.8. A comparison of etch rates for vertically and laterally for the blanket etch step after 3 and 5 min of etching.

The lateral etch rate ranges from 1.9 to 4.3 µm/min, which is a function of the sharpness of the initial re-entrant profile. The vertical etch rate was slightly negative relative to the top surface of the wafer, a function of broad wafer thinning. The power and pressure parameters of etch 2 were not found to have a significant impact on the etch geometry and were therefore not optimized.

Finally, the two-step etching process was integrated into the microfabrication flow of the microturbine, described in the previous section. The final mask opening was selected to be 215 μm, recipe 2 was selected for *etch 1* and recipe 4 was utilized for the blanket *etch 2*. The raceway etching was performed in 2 to 20 minute intervals to better understand the evolution of the raceway geometry. The depth, width, and curvature radii of the final raceway etch are presented in Figure 6.9.
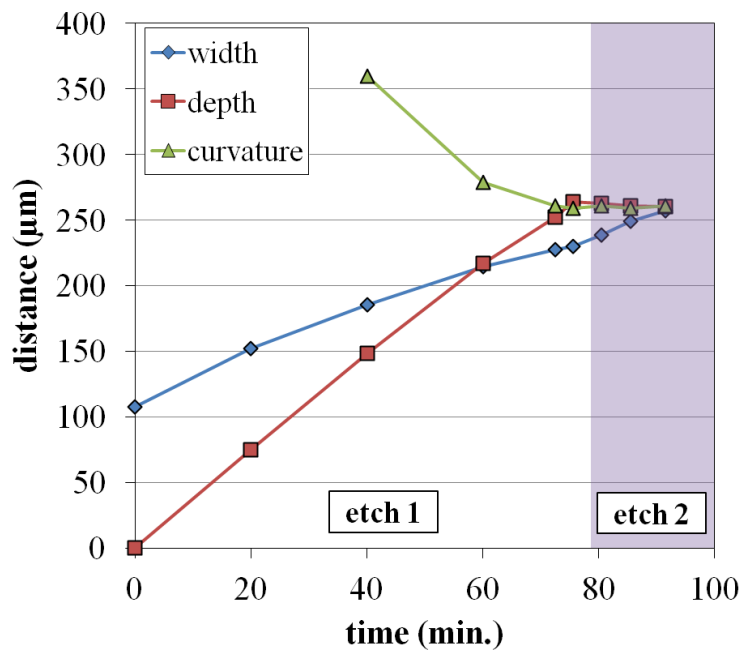
Figure 6.9. Evolution of raceway geometry through multistep etching process.

The bulk of the material is removed during the *etch 1* step and the curvature and depth nearly reach their final values. It is also interesting to note that there is some non-linearity in the lateral etch rate, with the etch slowing down towards the end of *etch 1*. This is a result of a minor starvation of reactants to the undercut sidewalls. The final raceway uniformity was measured by optical profilometry and presented in Figure 6.10. It is important to minimize variation in raceway depth to minimize out-of-plane vibration in the rotor during operation which can lead to excessive wobble and uneven loading of the balls.
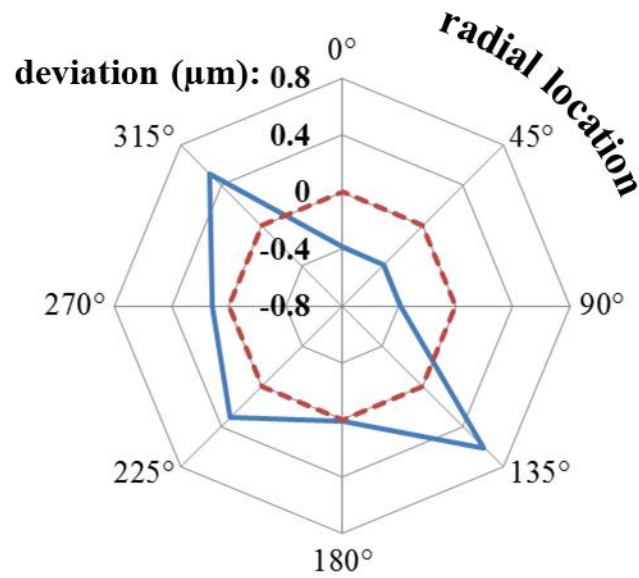
Figure 6.10. Radial plot of raceway depth variation. The average depth is plotted at "0" and deviation is either positive (deeper than average) or negative (shallower than average).

An average variation of 340 nm or 0.15% of the raceway depth around a 5 mm diameter rotor was measured. This value of uniformity is on par with well-tuned DRIE and very good for isotropic etching techniques [119].

Upon completion of the raceway etch, the wafer was spray-coated with *AZ 4999* photoresist to cover the inside surfaces of the raceway to mask the offset release etches. The offset release pattern lithography was compensated by reducing feature sizes to take into account the curved substrate and UV light spreading. Scanning electron microscopy images of a completed raceway with the offset release etch as well as a bonded microturbine with the turbine impeller structure removed is shown below in Figure 6.11.
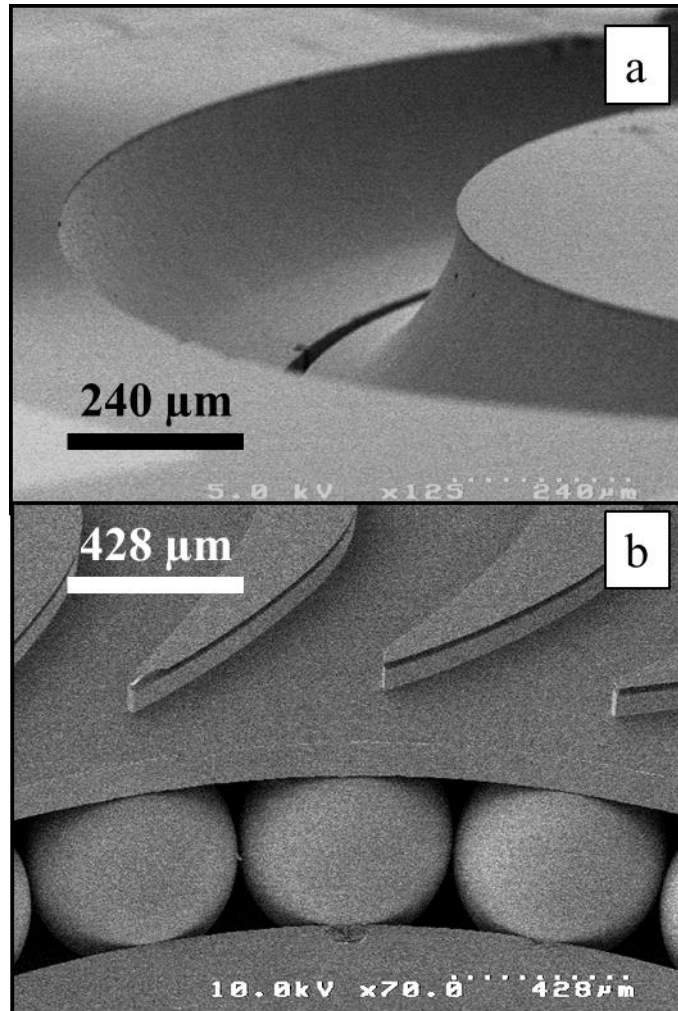
Figure 6.11. SEM images of microturbine. a) completed raceway with nested offset release etch visible. b) bonded device with turbine impeller removed.

6.4.2 Microturbine Operation

Three of the four variations of the deep-grooved raceway microturbine were tested, employing two rotor diameters (2.5 and 5 mm) and two ball materials (steel and silicon carbide). The first set of tests was performed on raceways that were 512 μm in diameter, providing 12 μm of clearance for these devices. Testing is performed by monitoring the turbine operating parameters: flow, pressure, and speed, through an acrylic package (Figure 6.5). A custom LABVIEW ™ interface was created to control the device and acquire data, similar to the set-up described in 2.4.

The 5 mm, silicon carbide variation was the first device tested. It was operated successfully above 65 krpm before catastrophic failure. The normal load on the rotor was 30 mN at 65 krpm, which resulted in a contact angle between 25° and 40°, allowing the ball to make contact with the offset release etch. It is assumed raceway facture was initiated at the sharp contact point where the offset etch meets the raceway. Once fracture was initiated on the raceway, the rotor became unstable and completely fractured the raceway over a time period of <10 seconds. Testing of this turbine was an experimental confirmation of the limits set forth from the numerical simulation.
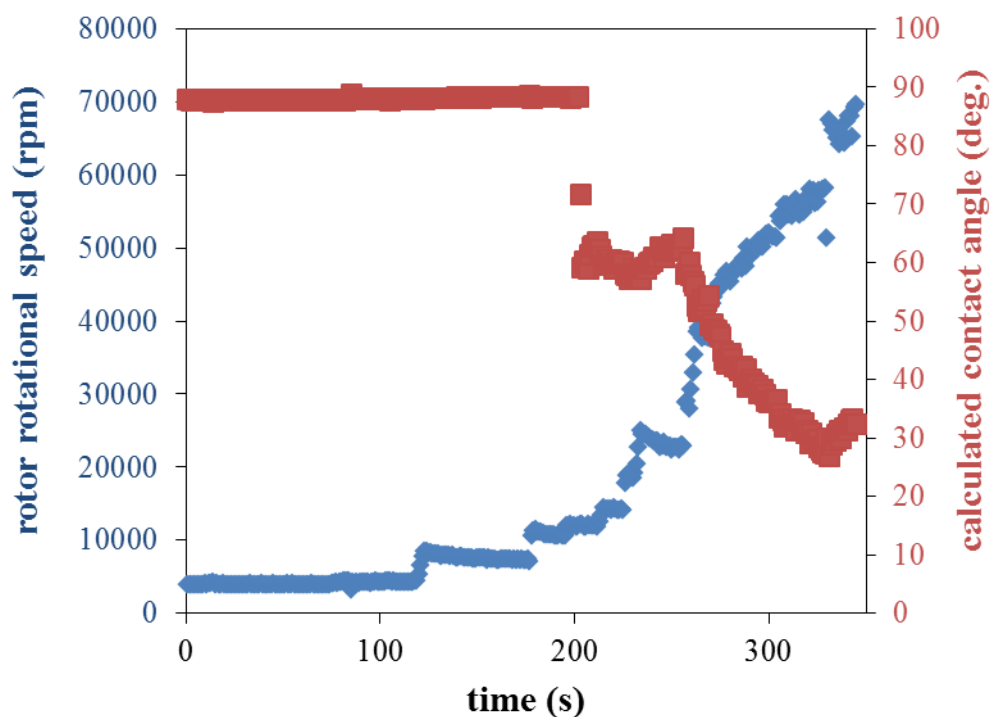
Figure 6.12. Operation of the first isotropic bearing-containing microturbine, showing measured rotor speed and calculated contact angle.

A drop below the 37° contact angle minimum is observed just before bearing failure. The erratic nature of the contact angle comes from human error in the operation of the device. Actuation flow and thrust flow are controlled manually, therefore adjustments are made discretely and there is lag between adjustments and microturbine response. Future systems

156

could integrate a contact angle calculator and adjust flows to maintain a desired contact angle for a given speed.

The next turbine tested was the 2.5 mm diameter, silicon carbide ball containing device. The rotor was actuated to 47 krpm under 15 mN rotor normal load, resulting in a calculated contact angle of 47°, over the geometrically defined 37° limit. This device was actuated for 5 minutes and then disassembled to observe the wear using SEM (Figure 6.13).
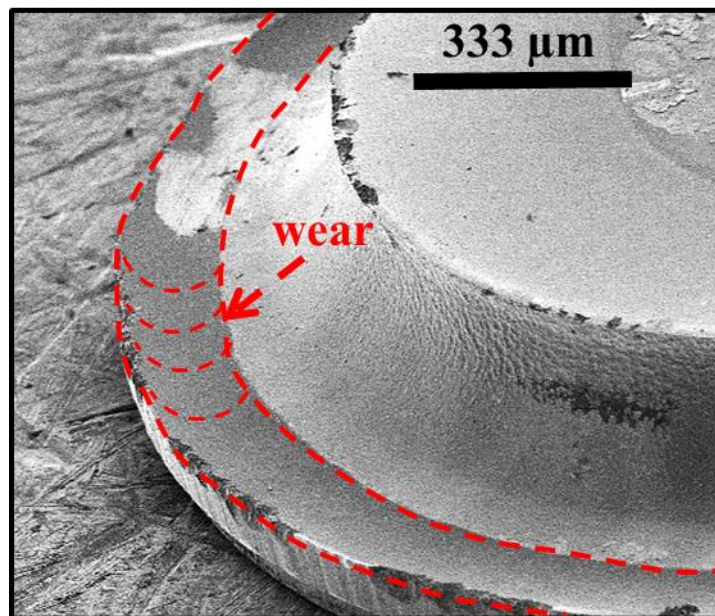
Figure 6.13. SEM of worn raceway from 2.5 mm rotor with silicon carbide balls. Wear area is highlighted.

The wear observed in Figure 6.13 was of an abrasive nature, with the harder SiC balls removing material from the Si raceways. The effect was significant, measuring 1-2 μm of removed raceway material within the contact area of both the top and bottom ellipsis. This abrasive wear is due to the significant sliding motion imparted by the geometry of the raceway, discussed in the *bearing dynamics* section above. Higher normal loads would reduce the magnitude of the sliding by shifting the contact ellipse towards perpendicular of

157

the axis of rotation of the ball and allow for better rolling. Lubrication has also been shown to work well in the case of sliding-regime wear, and is the subject of future studies.

A second set of microturbines were fabricated with much larger tolerances in order to reduce the size of the contact ellipse, thereby reducing the amount of sliding in the system. The tested microturbine was 2.5 mm in diameter and contained stainless steel balls. The diameter of the raceway was measured to be 560 μm, resulting in 60 μm of side-to-side play. This width was chosen to give ample room for the ball during encapsulation and bonding, as well as a 38% decrease in contact area at 100 mN rotor normal load for the 2.5 mm SS device. The testing of the device is shown in Figure 6.14.
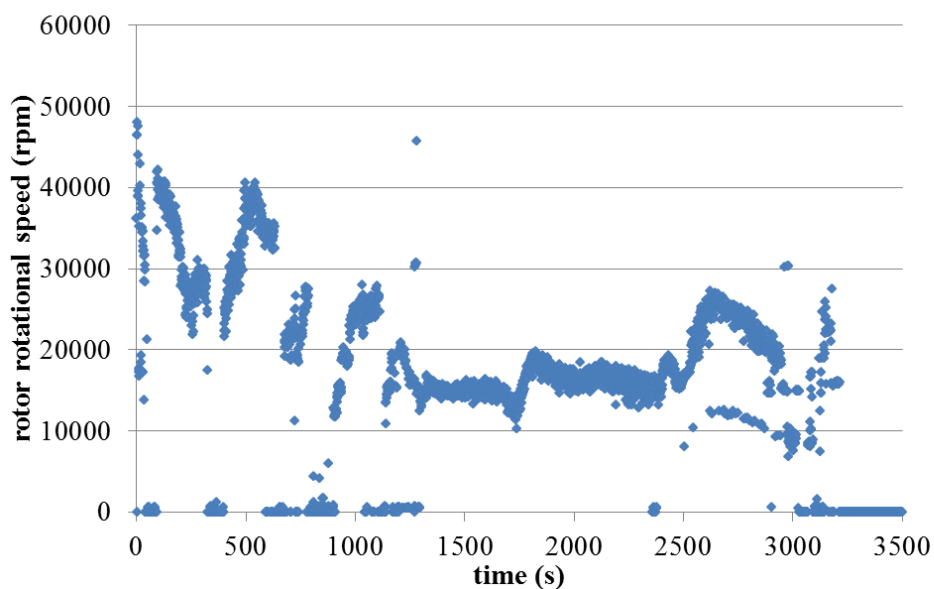
Figure 6.14. Operation of a 2.5 mm SS microturbine with isotropic raceways.

The device begins spinning at 40 krpm, then quickly fails. This pattern of on/off operation continues with a general trend towards decreasing operating speeds. As a point of reference, it requires 11 W of input power to operate this microturbine at 10 krpm compared to 0.05 W to operate the *500, high* variation microturbine described in chapter 3. The bearing and turbine inefficiencies are convoluted in the input power vs. speed comparison; therefore it is

difficult to determine the source of the performance difference. From the turbine efficiency standpoint, the device with the isotropic bearings has 100 μm tall blades and 60 μm of rotor sag, leaving 40 μm of exposed turbine structure, compared to 250 μm tall blades with 10 μm of sag for the *500, high* device. Therefore it is estimated that the difference in performance has a significant turbine efficiency component.

The second major influence on the device performance is the side-to-side play allowed for in the rotor. The *500, high* devices utilized 510 μm raceways, allowing for 10 μm side-to-side play in the raceway as well as a 50 μm tolerance within the journal etch. During radial movement of the rotor, the ball would be brought into contact with the sidewalls of the raceways before the rotor would contact the stator in the journal release etch. Conversely, the second generation deep-groove devices used 560 μm diameter raceways and 20 μm journals, meaning the rotor and stator are allowed to come into direct contact without obstruction from the ball. An image of the tested devices is shown in Figure 6.15.
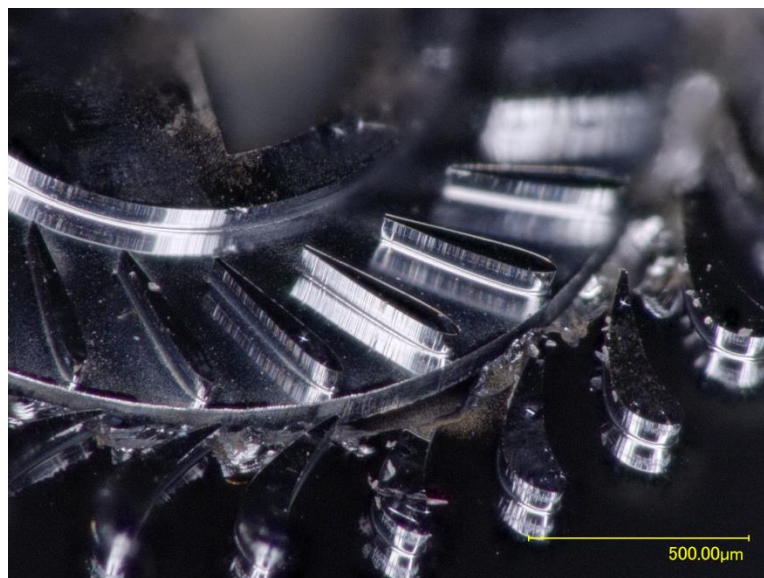
Figure 6.15. Photograph of 2.5 mm rotor diameter, stainless steel ball device after testing

Significant wear, in the form of brittle fracture, can be observed on the stator around the journal release etch. This is due to the side-to-side play in the device during operation

allowed for by geometry. The stop/start behavior of the device was likely caused by the generation and removal of fractured stator material.

SEM inspection of the raceway after 3000 s of discontinuous operation revealed a significant amount of abrasive wear. The abrasive wear mechanism, caused by sliding, was observed in Figure 6.13 for the silicon carbide balls after 300 s, and is shown for the 2.5 mm stainless steel ball device in Figure 6.16.
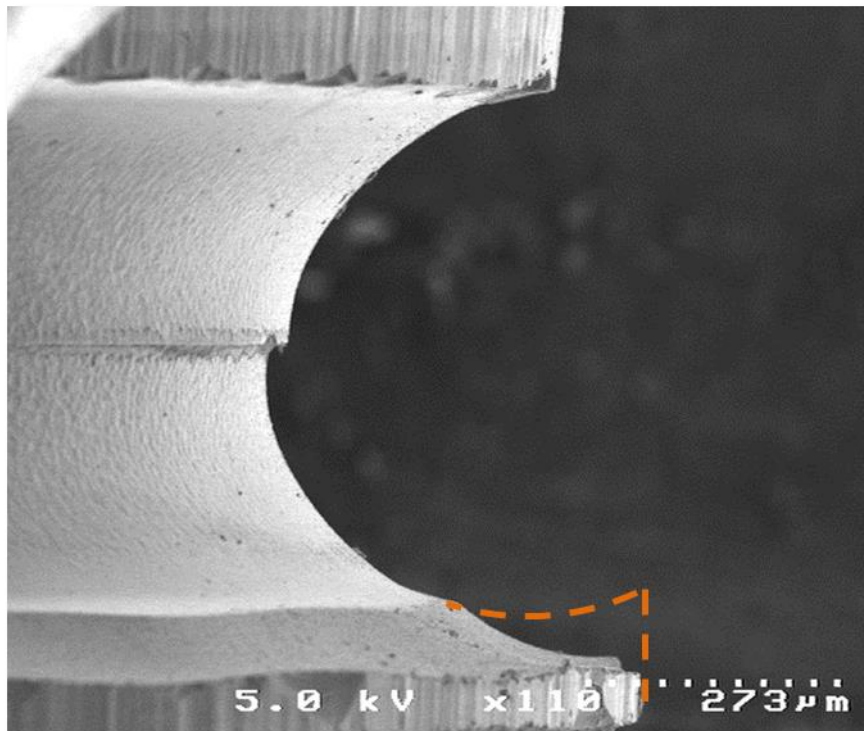
Figure 6.16. SEM of 2.5 mm, stainless steel device after 3000 s of operation. An estimate of the orignal raceway profile is shown.

During operation, the ball wore away a second radius within the grooved raceway. The original raceway profile is shown by the orange dashed line, estimated from known geometries. It should also be noted that there is some slight bond misalignment observed for this device (<20 µm), which will affect the device performance by introducing side-to-side motion. The significant amount of abrasive wear comes from the sliding discussed in section 6.2.1, which is inherent in the deep-groove design. Future devices should utilize lubrication

160

or new geometries to limit solid-solid contact, or reduce the magnitude of sliding, respectively.

Three devices utilizing deep-groove raceway geometry were fabricated and tested. Challenges arose with the operation, wear, and geometry of the devices, so the ultimate goal of high-speed, reliable operation was not realized, but speeds in excess of 65 krpm were obtained briefly. Next generation microturbines utilizing deep-groove geometry should utilize taller turbine structures, wider journal bearings, and lubrication for improved device performance.

6.5   Conclusion

This chapter presents the development of a 3D fabrication technique with the potential of significantly improving the performance of micro-scale rotary structures. The utilization of microball bearings for MEMS has shown great promise through an array of demonstrations, but there has always been a fundamental speed limit set by geometries limited by fabrication techniques. By developing a process to create uniform, smooth, curved surfaces, micro-scale ball bearings are enabled in regimes where load can be accommodated for both axially and radially. Deep-groove style ball bearings were selected to demonstrate the isotropic etch process within a functional device. Accordingly, a dynamic model of the bearing system was developed around a deep-groove style microfabricated geometry.

A two-step etching process for deep-groove bearing raceways was developed around the specific goal of integration within a microturbine testing structure. The first etch step was parametrically studied to optimize depth, width, and curvature, while maintaining good raceway uniformity and low roughness. The second etch step was performed to remove the re-entrant etch profile, widening the raceway to obtain the final geometry. Single device non-

uniformity in raceway depth was measured to be <0.15% and yield across the wafer was above 90% for the raceways.

The deep-groove geometry was demonstrated within multiple microturbines, reaching a maximum speed of >65 krpm. Significant sliding abrasive wear was observed from the large contact area, the combined centripetal and axial loads and geometrical profiles that provide linear velocity differentials across the area of contact. Devices with wider tolerances had significant amounts of radial play in the rotor, and therefore had non-ideal performance characteristics. With minor modifications to the raceway geometries, a deep-groove micro-scale bearing could be realized to long-lived operation.

This study presents a methodology to allow for a range of new micro-scale bearing geometries to be realized, based on circular-cross sectioned raceways. The isotropic etching technique can also be applied to other micro-scale geometries such as those used in optical and mechanical resonator systems. Future high-speed microball bearing systems will utilize isotropically etched profiles within application-specific geometries.

7. On-chip accelerometer-based diagnostics

This chapter demonstrates the utilization of an Off-The-Shelf (OTS) MEMS accelerometer to determine the onset of instability and perform *in situ* diagnostics of a high-performance rotary MEMS device. The accelerometer is shown to provide high sensitivity, wide bandwidth vibration measurements when bonded to the stator of a MEMS device. Vibration sensing is augmented with optical displacement sensors to create a multi-modal sensor platform. The sensor suite has been used to characterize the rotor instability for rotor speeds from 10-20 krpm, diagnose imbalance acceleration with sensitivity down to 0.001 g, determine rotor wobble of with an accuracy of <500 nm, and monitor system resonances through the speed range of 5-20 krpm. The aforementioned mechanical characteristics all signify the health of a mechanical system, therefore a knowledge of their baseline values, and a monitoring of any changes, provides a diagnostics/prognostics tool to increase device reliability. The data provided by the on-chip accelerometer can be used in feedback systems to optimize device performance and increase operational lifetimes.

7.1   Introduction

The MEMS accelerometer has become a critical sensor for scientific and industrial process monitoring and control. This includes consumer product applications such as motion sensing and image stabilization, structural applications including monitoring of bridge loading and earthquakes, and industrial applications in vibration-based condition monitoring of machines. The ubiquity of the accelerometer is due to the high sensitivity, high shock load resistance, and low mass of the sensors.

Complex rotary MEMS have been explored for such as power conversion [19], actuation [2], and sensing [120]. These devices serve as micro-scale analogues to their macro-scale counterparts. On the macro-scale, such machines undergo constant diagnostics to assure operation is in a low-wear regime and the device is taken offline before critical failure. As micro-scale systems become more widely adopted and relied upon for critical data or power in the case of sensors or generators, their constant operation will rely on diagnostic information. On-board diagnostics of this nature can also be accomplished within microsystems by integrating high sensitivity sensors with the microsystem.

All rotary devices have unstable operating regimes regardless of the bearing mechanism. In non-contact bearings, such as the microturbine reported by Frechette et al. [19], these instabilities arose from aerodynamic affects in the journal and thrust bearings. In the case of the microball bearings, instability arises from fabrication limiting the design to be a thrust bearing (parallel axis of rotation and primary load). The radial centripetal force acting on the rotating balls scales with *velocity*^{2}. The radial forces on the ball bearing will eventually encourage the ball to roll along the sidewall, rather than the intended thrust surface. The static friction between the ball and raceway counteracts the radial sliding. The rotor gradually loses load carrying capacity as it is accelerated to higher speeds unless a counter-acting normal load is imparted to keep the microballs in thrust-oriented operation. Using the accelerometer bonded to the microturbine, the instability-inducing load is determined for a range of speeds.

Rotor speed results in an angular acceleration of the microball bearings, manifested as centripetal load. The centripetal load of a microball bearing system is calculated and graphed in Figure 2.2. Chapter 2 and Chapter 6 make arguments for speed-induced stability issues within the rectangular bearing system. The rectangular bearing configuration cannot accommodate for high ball contact angles from high speed operation, and therefore has a

maximum speed limit. This chapter demonstrates the manifestation of these issues through vibration measurement.

Micromachined rotors are very sensitive to fabrication-induced imbalances. The centripetal force imparted on the rotor is the product of the *mass*, *radius*, and *angular velocity*[2] of a single defect. A minor defect on a low speed micro-scale device becomes significant at the speeds of 50krpm to >1Mrpm intended for power-generating MEMS because of the velocity dependence. Such minor imbalances can arise from misalignment in bonding or lithography processes or etch non-uniformities. Early detection of a rotor imbalance is critical to preventing catastrophic device failure as it is accelerated to operating speeds.

Machines from the macro- to micro-scale undergoing a vibration load need to design away from resonant operation modes. The resonance is characterized by a tendency to absorb significant amounts of energy when the input energy matches a natural resonant frequency of the mechanical system. Large amplitude oscillations are the result of operating in the resonant regime, which leads to accelerated wear and early failure. To counteract this potentially damaging operating regime, machines are often designed to operate sub- or super-resonant or incorporate damping to reduce oscillation amplitude.

The resonance of interest to micro-scale rotating machinery is the displacement of the rotor. Therefore the mechanical properties of the bearing, specifically the stiffness and damping, are the variables available to engineers to tailor micromachine operation to non-resonant modes. In the case of the microturbine from [19], the device was designed to operate above 1.4 Mrpm. To reach this speed, multiple resonant modes needed to be traversed, so active monitoring and control was necessary. Once it was determined that a resonant mode

165

was being approached through optical displacement sensing, the pressure-drop across the air journal bearing was adjusted to change the spring constant, and thus the resonant frequency. Outside of the lab setting, such a device would need to have resonant monitoring capabilities built-in to the system.

Four operating parameters were selected as the focus of the on-chip diagnostics: *bearing instability, imbalance diagnosis, rotor wobble,* and *system resonances.* It should be noted that while a microball bearing supported device was used to demonstrate the capability of the on-chip accelerometer, any rotary MEMS device could utilize this platform for similar analysis.

7.2   Experiment

A microfabricated silicon turbine supported on stainless steel microball bearings (*285, high* from chapter 3) serves as the platform for the diagnostic testing and characterization (Figure 7.1). The friction and performance of the microturbine has been thoroughly characterized chapters 2-5. The accelerometer (*Analog Devices, ADXL325*) is monitored through custom packaging that integrates turbine pneumatic actuation and sensing elements with electrical components. Testing is performed in a vibration-isolated isochoric chamber.
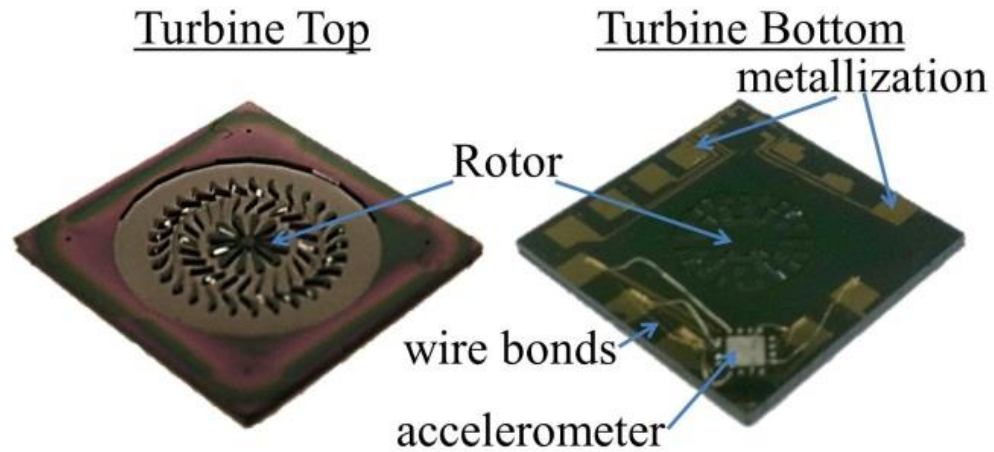
Figure 7.1. Photograph of silicon microturbine with attached OTS MEMS used for vibration sensing.

The silicon microturbine of the *285,high* (chapter 3) variation was modified to include backside contact metallization, where various accelerometers could be attached to the surface to ensure solid mechanical contact. Metallization was performed by sputtering Ti/Cu through a silicon shadowmask at the chip-level. The microturbine rotor is actuated to speeds up to 20 krpm with compressed N_2 gas flow. A new packaging was created for the vibration study to included manifold layers for turbine actuation and pneumatically controlled thrust load, pressure sensors, optical displacement sensor, as well as electrical contacts for accelerometer input and output voltages. The packaging of the test device segregated turbine flow and a thrust plenum, allowing for the decoupling of thrust and actuation loads.

The *ADXL 325* accelerometer used to measure mechanical vibrations has a bandwidth of 1.5 KHz, sensitivity of 167 mV/*g*, and range of +/- 5 *g*. A MEMS accelerometer operates by constantly comparing the capacitance between reference and measurement plates attached to the frame and proof mass, respectively. As the device is accelerated, the proof mass shifts relative to the frame, the distance change is then measured as a change in capacitance. The sensor has the potential for 3-axis acceleration monitoring, although it was found that a majority of the useful information came from the axis parallel to the radial direction relative

to the rotor axis of rotation. Electrical contact was made via low-stiffness, spring-loaded pins to minimize vibration dampening.

An optical displacement sensor (*Philtec, D-6)* was utilized to measure out of plane displacement around the periphery of the rotor (wobble) to augment the accelerometer measurements. The optical sensor has a displacement sensitivity of 380 nm over a range of 51 μm. This wobble is induced by the imperfect depth profile of the raceways supporting the microball bearings. The deep-reactive ion etched raceways show a measured depth variation of 0.25% around the 10 mm diameter trench which sets a minimum peak-to-peak distance for the potential wobble of the system.

Significant measures were taken to assure the measured accelerations and wobble were isolated from the surrounding conditions. The microturbine made soft, elastomeric contact to its packaging through the use of rubber o-rings. The package was suspended through another elastomeric contact above the floor of an isochoric chamber, also through the use of rubber O-rings in between a cantilevered turbine package. The chamber was supported on a floating table. This was to assure that outside vibration did not translate to the device or *vice versa*. The LabVIEW™ code for the software is included in the appendix. A photograph of the testing chamber is shown in Figure 7.2.
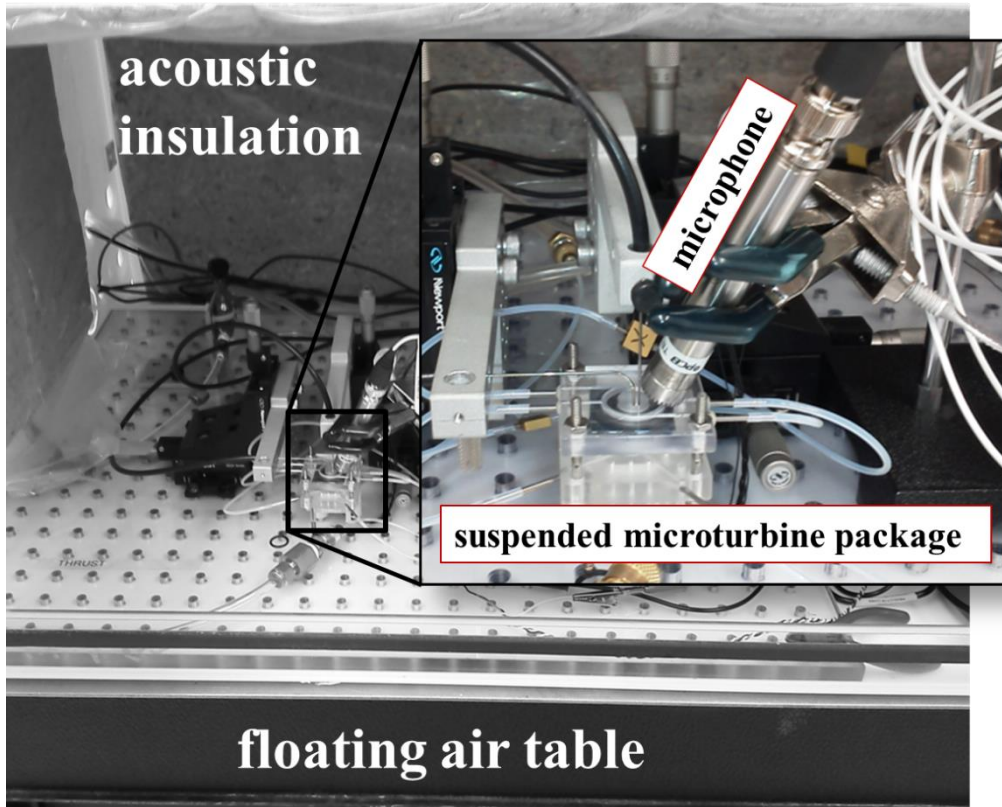
Figure 7.2. Photograph of the testing set-up used in the diagnostic experiments.

7.3   Results

7.3.1   Bearing Instability

Figure 7.3 shows the measured radial vibration, representative of increased ball-to-sidewall contact for a range of speeds and normal loads. These results correlate well with the calculated transition from thrust to radial operating regime (Figure 7.3inset). The microturbine was not operated to a completely unstable regime due to the potential for catastrophic failure. It is expected that if the normal load is decreased significantly below the thrust operating regime, the rotor will lose stiffness in the axial direction and wobble violently. On the other hand, excessive normal load will lead to accelerated wear rates in the

raceway as shown in chapter 4. The information from the accelerometer highlights the need to balance speeds and loads for operation in low vibration/low wear regimes.
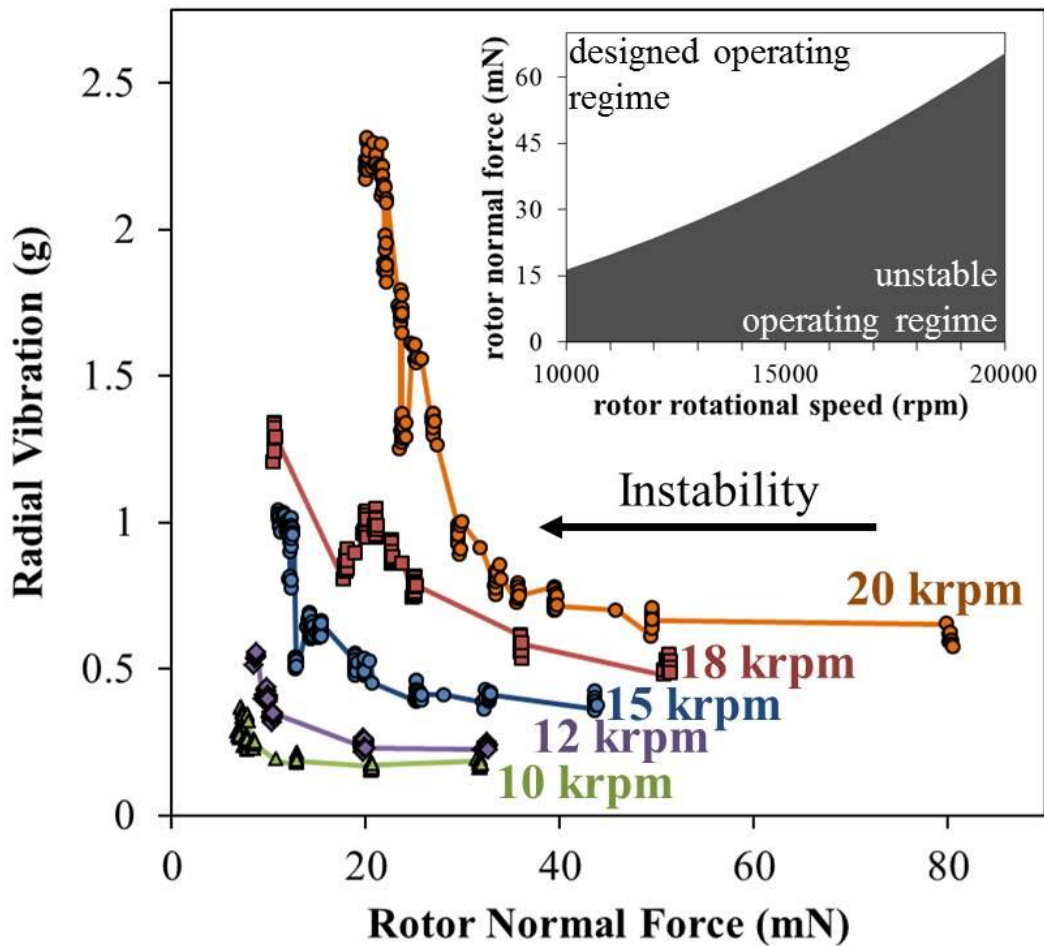
Figure 7.3. Measurement of radial vibrations over a range of loads for set speeds. (inset) graphical representation of bearing operating regime calculated from first principles.

As normal load is decreased at a given speed, radial vibration significantly increases. This is a feature of the increasing influence of centripetal load on the balls, and the reduction of the ability for friction between the ball and the raceway to keep the balls in place. Knowing this, an optimal operation load can be selected for each speed, which is the minimum load before a significant increase in radial vibration, 40 mN at 20krpm in Figure 7.3. While this imbalance was theorized in previous chapters, this is the first measurement of its existence.

7.3.2 Imbalance Diagnosis

The accelerometer has been used to diagnose an experimentally unbalanced rotor. For these testes, the rotor is operated at a set rotational speed and a time-averaged vibration spectrum is obtained for the radial (perpendicular to the axis of rotation). The unbalance is observed by taking the FFT of the vibration spectrum data. A peak is observed corresponding to the operating speed. The microturbine is unbalanced by placing less than 1 milligram of polymer photoresist in a single location along the periphery of the rotor, measured with a microbalance. Figure 7.4 shows the appearance of the fundamental peak for an unbalance rotor, and the baseline measurement taken before unbalancing and after the polymer is removed.

The force sensitivity limit of the on-chip accelerometer has been demonstrated as low as 0.001 g. To generalize the diagnostic capabilities, a sensitivity coefficient of 0.0098 ($m_i \times r_i \times \omega^2$)/$m_r$ is defined where ω is rotor rotational velocity, m_r is the rotor mass, m_i and r_i are the mass and radius of the imbalance, respectively. This correlates to a minimum sensed mass imbalance of 0.2 μg at the periphery of the rotor spinning at 50 krpm.
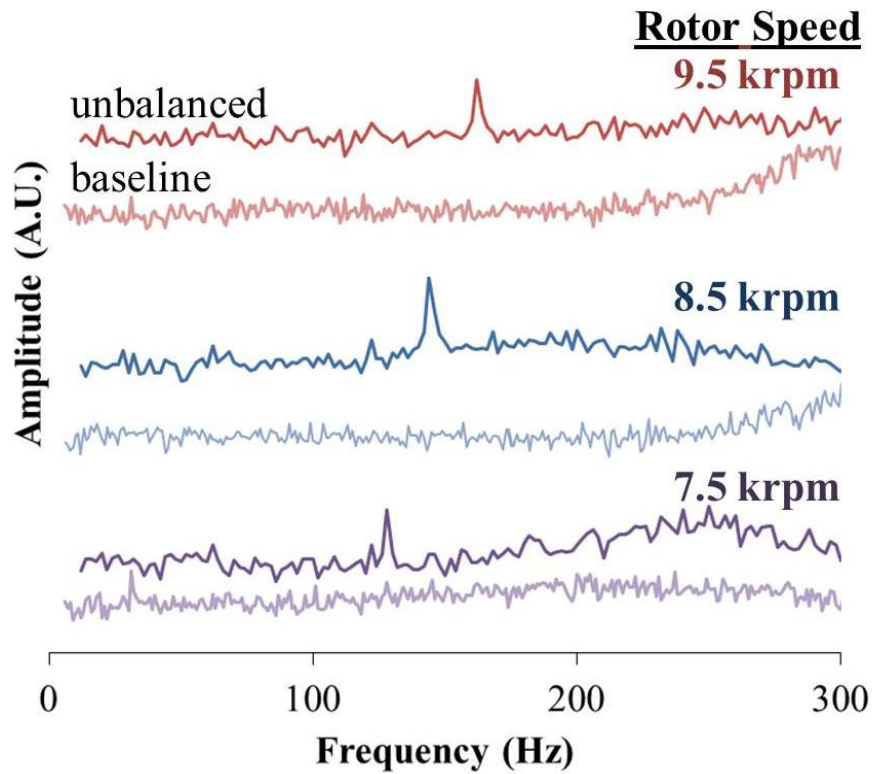
Figure 7.4. Imbalance is induced on the microturbine rotor and measured via the on-chip accelerometer.

The observed imbalance shifts with increasing speed, as expected. At higher speeds, the magnitude of the imbalance peak would also significantly increase. Because of the velocity dependence, very minor imbalances will become observable at very high speeds. Contact lithography methods, used to define many of the features in MEMS fabrication, has an alignment tolerance of about 0.5 μm. If multiple layers are misaligned, then the total misalignment could be on the order of micrometers, which would result in a significant imbalance. Using this diagnostic method, imbalanced rotors could be identified before being deployed in commercial systems.

Multiple on-chip accelerometers could be used to triangulate imbalances, so they could be located and potentially corrected. If the radial position of the rotating element is synchronized with the accelerometer, then the phase shift between the fundamental peak and peaks in the FFT of the vibration signal could be used to determine angle of the net

172

imbalance. Impact event locations could be determined through the synchronization of two accelerometers and the rotating element, using the time delay of the signal to determine the location and magnitude of the impact signal eliminate uncertainty due to rotational symmetry.

7.3.3 Rotor Wobble

Rotational sensors and actuators need to accommodate for wobble when establishing sensitivity and operating parameters. On-rotor optics intended for long-range sensing will be extremely sensitive to unintended out of plane movement. Similarly, rotary gyroscopes are inherently sensitive to tilt in the rotational axis. Therefore, we determine rotor wobble is an important metric for rotary microsystems.

The out-of-plane movement of the rotor is monitored using an optical displacement sensor. From this data, the minimum normal load is discovered to insure minimum wobble operation. Figure 7.5 shows the peak-to-peak wobble versus normal load. While the microfabrication of the silicon microturbine is not the focus of this paper, it is important to note a necessary asymmetry in the raceways.

The microturbine test device is shown schematically in Figure 7.5b. A complete fabrication scheme is detailed in section 2.3. The implication of the offset release etch is that the balls make contact to flat surfaces in one direction of net normal load, and contact to etched corners in the unintended direction of normal load (Figure 7.5b), resulting in a desired direction of normal load.
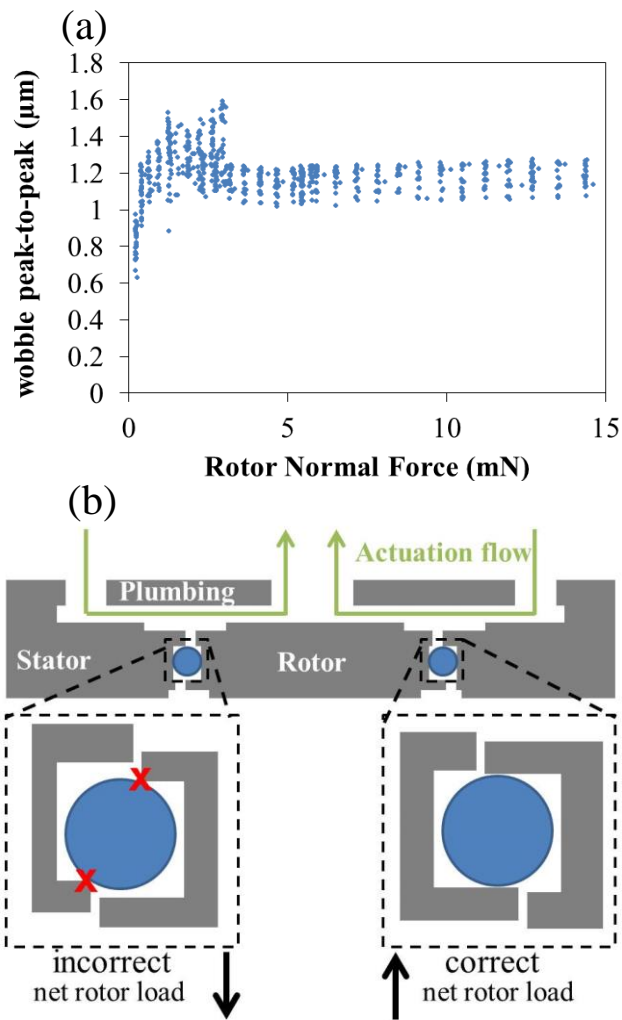
Figure 7.5. (a) Rotor wobble versus normal load. (b) cross-sectioned schematic of the microturbine highlighting two possible operating orientations.

The rotor wobble data shows that at low normal loads, the actuated load and external gravitational load are nearly balanced, so the rotor flutters between the two bearing orientations. Once the actuated load exceeds gravitational load, the rotor settles to a 1.2 μm peak-to-peak operation. The steady-state wobble is due to non-uniformity in the raceway etching process. The non-uniformity is expected to improve for smaller radii devices, because uniformity is geographically dependent on the wafer, so smaller devices will span shorter distances.

7.3.4   System Resonance

The resonance of the microball bearing supported turbine was discovered in this study using the on-chip accelerometer. The microturbine was repeatedly actuated to 20 krpm and the average vibration acceleration was obtained periodically. Additionally, the FFT of the vibration signal was obtained through the range of speeds. The amplitude of the FFT at the 1X fundamental frequency was extracted and plotted against the average acceleration in Figure 7.6. A peak in the peak amplitude of the fundamental frequency can be observed at 11.3 krpm, which represents a resonant operating mode of the microturbine rotor. Past 11.3 krpm the fundamental peak height scales comparably with the average vibrational acceleration.
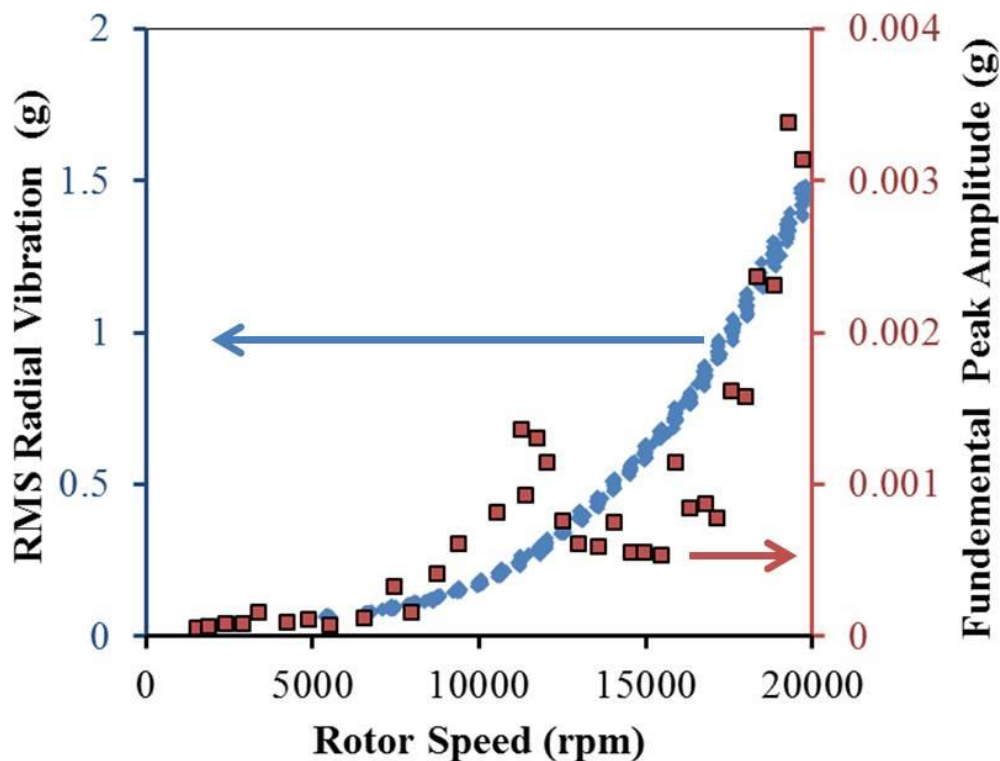
Figure 7.6. The fundamental peak amplitude and RMS average radial vibration. The fundamental peak height shows a peak at 11.3 krpm corresponding to a rotor resonance.

The resonant frequency of the rotor also contains information about the bearing stiffness at the resonant speed. Assuming the bearing is lightly damped, the rotor-bearing system can be treated as a simple harmonic oscillator (SHO), where the resonant frequency is equal to the root of the ratio of the spring constant to the mass. Based on the properties of the system, a resonance at 11.3 krpm (183 Hz) corresponds to a spring constant of 6 N/m in the bearing (from SHO calculation). Acceleration is transmitted from the rotor to the accelerometer via two possible paths: a non-contact perturbation of the air within the release trench and bearing cavity, or a contact of the ball bearing to the sidewalls of the rotor and stator. The spring constant calculated from the resonance confirms that the rotor displacement is only a perturbation of the air journal bearing and not squeezing the ball in solid-solid contact, therefore this specific resonant mode is not expected to have a significant detriment on microturbine lifetime.

7.4 Conclusion

This chapter highlights the importance of *in situ* diagnostics for mechanical systems by using an on-chip, OTS, MEMS accelerometer to accurately and repeatedly determine the onset of instability and perform diagnostics of a high-performance rotary MEMS device. The diagnostics can be used to determine low-wear operating regimes, increasing device lifetimes. The vibration sensing mechanism was used to determine the ideal operating loads and speeds for the micro-ball bearing based microturbine. The centripetal force-induced instability in the thrust ball bearings was determined for speeds from 5 krpm to 20 krpm. The device was unbalanced artificially and measured experimentally. The mechanical vibration sensing has been augmented by non-contact optical displacement measurements of wobble. Resonance was measured in the rotor and used to calculate the effective bearing stiffness.

These features would have otherwise been difficult to accurately predict due to the complex, highly coupled nature of moving microsystems.

The precedence for on-board, monolithically fabricated diagnostics does not currently exist in the MEMS community. While this work is focused on the integration and demonstration of currently available technologies, it is also possible to monolithically fabricate accelerometer structures on chip for direct sensing. It is envisioned for future fabrication schemes that allow for on-rotor vibration sensing with on-chip electronics for signal processing towards systems with integrated feedback.

8. Conclusions and Future work

8.1   Summary

This work explores the fundamentals of rolling contact in systems relevant to current and future technologies specifically microfabricated rolling bearings for future micro-machines. The main focus has been to determine the main source of rolling friction in the micro-scale systems from a theoretical/physical perspective and through experiments. In parallel, the wear regimes have been explored for a number of different operating conditions. Finally, a diagnostic platform was employed. A new micro-scale bearing geometry has been engineered using an etch process developed for high-speed bearing operation, and the new geometry has been tested.

Rolling friction is understood to be the complex combination of plastic deformation, elastic hysteresis, differential slip, surface adhesion, and many other minor components. The extent of the contribution of each individual component is strongly dependent on the materials and geometries in question. Previous work by McCarthy *et al.* on microball bearings, suggested a power-law relationship between friction torque and normal load [6]. The power-law relationship provided a reasonably good fit to data but did not have any physical significance. This dissertation has identified adhesion as the fundamental source of micro-scale rolling friction which allowed for the development of a friction/normal load relationship with physical meaning based on the properties of the adhesive mechanism.

This work presents a model for micro-scale rolling friction which is adhesion-dominant contrary to macro-scale friction models which are elastic hysteresis dominan. To test the adhesive

component of rolling friction, two studies were performed; One experiment varied the contact area, while a second varyied the adhesive energy. Silicon thrust bearings packed with 285 μm and 500 μm diameter stainless steel balls have been tested over a load and speed range of 10-100mN and 500-10,000 rpm, respectively. A relationship between friction torque and applied load is derived from Hertzian contact mechanics and validated by experiments and observed adhesive wear. The experimentally derived relationship suggests that surface effects dominate over volumetric contributions to rolling friction, unique to the micro-rolling regime, as well as taking into account the load-independent contributions to system friction such as viscous drag.

The wear mechanisms have been studied for a microfabricated ball bearing platform that includes silicon and thin-film coated silicon raceway/steel ball materials systems. Adhesion of ball material, found to be the primary wear mechanism, is universally present in all tested materials systems. Volumetric adhesive wear rates are observed between $4\text{x}10^{-4}$ μm^3/mN•rev and $4\text{x}10^{-5}$ μm^3/mN•rev, suggesting that the adhesive wear mechanism is heading towards equilibrium. Pressured-induced phase changes take place in the contact areas of the bare silicon raceways, changing the mechanical properties of the raceway contact. An understanding of the wear mechanisms within microfabricated ball bearings will help optimize operational parameters and materials systems for long-term reliability through operation in known load and speed regimes, and efforts to mitigate adhesive wear.

The fundamentals of vapor phase lubrication have been discussed within the context of the experiments to address adhesion through the reduction of surface energy via the addition of adsorbed vapor layers. Pressure relations to chemistry and temperature have been explored. The experimental platform has been explained in a thermodynamic sense. From the pressure relationships, the nature of adsorption is explored.

Once an understanding of adsorption has been established, spin-down friction testing is performed on multiple microturbines and used to show the efficacy of vapor phase lubrication (VPL). The relationship between friction torque and normal load is significantly altered with the addition of VPL, suggesting that adhesion is a dominant factor in micro-scale rolling friction. Multiple levels of RH have been saturated within the carrier gas and used to actuate the microturbine, providing insight as to the quality and nature of adhesion. VPL provides an example mechanism to reduce system friction, translating to reduced drive-mechanism power requirements for future microball bearing enabled devices, as well as reduced wear rates, leading to longer device lifetimes.

This work also demonstrates the utilization of an Off-The-Shelf (OTS) MEMS accelerometer to accurately and repeatedly determine the onset of instability and perform in situ diagnostics of a high-performance rotary MEMS device. The accelerometer is shown to provide high sensitivity, wide bandwidth vibration measurements when bonded to the stator of a MEMS device. Vibration sensing is augmented with optical displacement sensors to create a multi-modal sensor platform. The sensor suite has been used to characterize the rotor instability for rotor speeds from 10-20 krpm, diagnose imbalance acceleration with sensitivity down to 0.001 g, determine rotor wobble of with an accuracy of <500 nm, and monitor system resonances through the speed range of 5-20 krpm. The data provided by the on-chip accelerometer can be used in feedback systems to optimize device performance in *real-time* and increase operational lifetimes.

This work also presents the development of a 3D fabrication technique for creating uniform, smooth, curved surfaces, enabling micro-scale ball bearings to support axial and radial loads. This will significantly improve the performance of future, high-speed, micro-scale rotary structures.

Finally, it is important to discuss the applicability of this work to systems outside those that were specifically studied. In general, when a system is scaled down in dimension, the influence of surface properties will always increase relative to the volumetric properties. This transition is continuous rather than discrete, so there should not be a specific size-scale where surfaces begin to dominate rolling friction, but rather a gradual increase in the influence of surfaces as the dimensions are scaled down. From a manufacturing standpoint, two factors need to be considered: the size limitations of macro-scale machining, and the availability of spherical ball bearings. Macro-scale ball bearing systems can be reliably manufactured to diameters around 2.5 mm, using balls 0.5 mm in diameter. Given the maturity of this technology, it does not make sense for micro-fabricated ball bearing systems to compete at this scale unless 1) silicon is simultaneously used as a mechanical and electrical material or 2) there are structures other than the bearings which are smaller than the capabilities of macro-scale machining. This defines the maximum size for a microfabricated ball bearing system. The minimum size is determined by the availability of high-grade ball bearings. Steel balls, grade 10, of 285 μm in diameter and be reliably sourced. If the ideal ball diameter-to-inner diameter is 1:3, then that gives a rotating element size < 1mm diameter. The adhesion-based rolling friction hypothesis should apply through the size range limited at the maximum by competition with macro-scale machining and at the minimum by the availability of very small, high grade balls.

8.2   Summary of accomplishments

- Showed through a series of experiments that adhesion plays a significant role in micro-scale rolling friction in opposition to well-accepted macro-scale relationships.

- Developed and tested a new, microfabricated deep-groove bearing geometry that will enable micro-rotary structures to be operated at high-speeds.

- Developed a new MEMS characterization system based on an off-the-shelf accelerometer.

8.3 Future work

Tribology is a field of science that combines aspects of materials and mechanical engineering, chemistry, and contact mechanics. This combination of contributing factors makes any knowledge of a tribological system specific to the materials and geometries in action. For this study, the focus was on silicon raceways and steel balls and adhesion was found to be a dominant factor. One suggestion that emerged from this dissertation is to use ceramic balls for their decreased density and adhesive energy. Future ceramic microball supported devices will likely not be dominated by adhesion-based friction, but rather a new, unknown mechanism. The methodologies and analysis methods presented herein could be used to study such systems but the conclusions and suggestions moving forward would be different. Until microball bearings are mass-produced, any future microball bearing device will be designed on an application-specific basis and future work will have to be done on the application specific tribology of that system.

8.3.1 Angular Contact Microfabricated Bearings

It was shown in chapters 2, 6, and 7 that high-speed bearing operation for power-generation applications is unrealistic without modifications to the bearing geometry. The geometry realized in chapter 6 was proven beneficial compared to the original rectangular –cross section but was still

non-ideal from a dynamics standpoint due to the spinning within the contact area arising from the relationship between the rotor and ball axis of rotation. On the macro-scale, combination thrust and radial loads are handled by an angular contact bearing. This could be done on the micro-scale but the fabrication challenge of obtaining this geometry is beyond the scope of this dissertation. Figure 8.1 shows the theoretical angular contact bearing geometry.
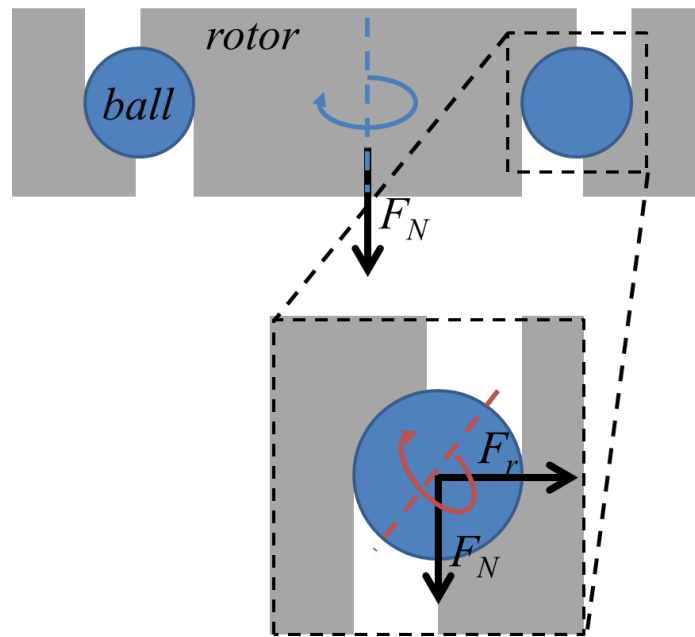
Figure 8.1. (top) micro-scale device with angular contact bearings, showing the rotor axis of rotation and principle direction of normal load. (bottom), zoomed-in view of bearing, showing the radial and normal loads, as well as the ball-axis of rotation.

The angular contact bearing can handle radial and thrust load, although the thrust load must be in a single direction for the lifetime of the device. To keep the device from falling apart, very tight geometries would be needed to press-fit the rotor into place with the balls loaded. This geometric requirement was the principle reason this geometry was not explored in this study. The main benefit is derived from the axis of rotation being allowed to exist perpendicularly to the ball contact angle,

minimizing sliding friction. In the deep groove bearings presented in chapter 6, the ball contact angle and axis of rotation were not perpendicular, leading to significant sliding friction.

8.3.2   Retainer Ring Integration

Ball separating retainer rings are almost universally utilized in macro-scale bearings. In micro-scale bearings, retainer ring technology could greatly reduce the overall cost of the device, due to the reduction of high cost of the precision microballs used. In addition to evenly distributing loaded bearings, another advantage of using a silicon retainer is that electronics could be easily integrated on the retainer. An SEM image of a retainer ring-containing device is shown in Figure 8.2. In parallel work, Hergert *et al.* has shown that a silicon retainer ring integrated into a silicon microturbine with a thrust ball bearing can provide reliable and repeatable operation for at least 500,000 revolutions [121], although the current geometry imparts significant sliding friction into the bearing, reducing microturbine performance by at least an order of magnitude compared to free balls.
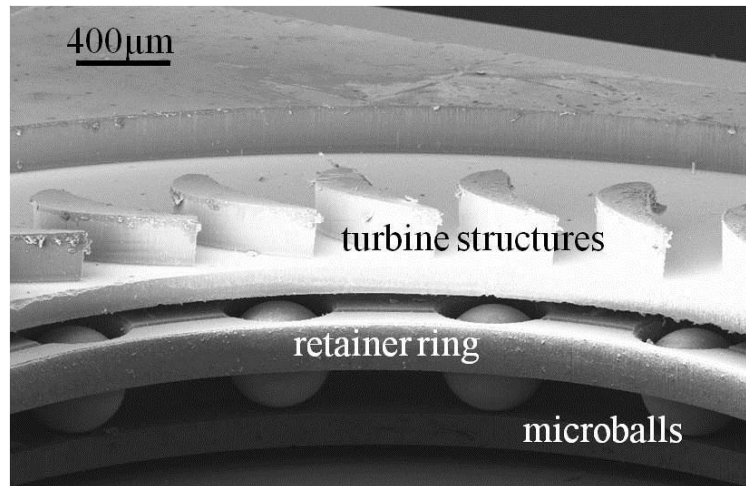
Figure 8.2. Microfabricated silicon retainer ring within a microfabricated thrust bearing, rotor removed. SEM image adapted from [121].

8.3.3 Systems integration

The use of a silicon rotor in a ball bearing supported micromachine allows for the system-level integration of a variety of components. The integration of multiple electro-mechanical components on-rotor is the primary reason silicon was used in the first place. The performance of a fully-integrated device consisting of several sensors and actuators supported on microballs heavily depends on system dynamics defined by the bearings. In applications where speed plays a major role in achieving high performance, parameters such as the air gap between stationary and rotary components, tolerances in the ball raceway, and materials used are the primary factors determining device speed, stability and lifetime. While a small rotor-stator air gap leads to higher power density and actuation forces, it also results in higher normal loads, specifically in electrostatic and electromagnetic transductions, that may induce excessive wear in the raceway and decrease system lifetime. High tolerances in the bearings are easier to fabricate, however as shown in chapter 6, they can lead to instabilities in the system. In sensing applications where the ball bearing supported rotor can be used as a platform for directional sensor integration, positioning resolution, precision, and

accuracy become the figures of merit. Attaining high performance in these merits impose additional fabrication restrictions on the ball raceway to achieve smooth surfaces. Friction characteristics of the raceway surface also define the mechanical damping that directly correlates with positioning settling time. The stable and robust nature of ball bearing supported micromachines enables the incorporation of multiple functional components based on a variety of transduction mechanisms for the development of fully-integrated microsystems. The performance factors in such systems are defined through the optimization of the geometry, dimensions, and materials that is possible by tailoring microfabrication processes.

9. Bibliography

[1]   C. M. Waits, M. McCarthy, and R. Ghodssi, "A Microfabricated Spiral-Groove Turbopump Supported on Microball Bearings," *Journal Of Microelectromechanical Systems,* vol. 19, pp. 99-109, Feb 2010.

[2]   M. McCarthy, C. M. Waits, M. I. Beyaz, and R. Ghodssi, "A rotary microactuator supported on encapsulated microball bearings using an electro-pneumatic thrust balance," *Journal Of Micromechanics And Microengineering,* vol. 19, Sep 2009.

[3]   N. Ghalichechian, A. Modafe, M. I. Beyaz, and R. Ghodssi, "Design, fabrication, and characterization of a rotary micromotor supported on microball bearings," *Journal Of Microelectromechanical Systems,* vol. 17, pp. 632-642, Jun 2008.

[4]   N. Ghalichechian, A. Modafe, J. H. Lang, and R. Ghodssi, "Dynamic characterization of a linear electrostatic micromotor supported on microball bearings," *Sensors And Actuators A-Physical,* vol. 136, pp. 496-503, May 16 2007.

[5]   C. M. Waits, B. Geil, and R. Ghodssi, "Encapsulated ball bearings for rotary micro machines," *Journal Of Micromechanics And Microengineering,* vol. 17, pp. S224-S229, Sep 2007.

[6]   M. McCarthy, C. M. Waits, and R. Ghodssi, "Dynamic Friction and Wear in a Planar-Contact Encapsulated Microball Bearing Using an Integrated Microturbine," *Journal Of Microelectromechanical Systems,* vol. 18, pp. 263-273, Apr 2009.

[7]   A. D. Corwin and M. P. de Boer, "Effect of adhesion on dynamic and static friction in surface micromachining," *Applied Physics Letters,* vol. 84, pp. 2451-2453, Mar 29 2004.

[8]   N. S. Tambe and B. Bhushan, "Nanowear mapping: A novel atomic force microscopy based approach for studying nanoscale wear at high sliding velocities," *Tribology Letters,* vol. 20, pp. 83-90, Sep 2005.

[9]   B. Bhushan, "Micro/nanotribology using atomic force microscopy/friction force microscopy: state of the art," *Proceedings Of The Institution Of Mechanical Engineers Part J-Journal Of Engineering Tribology,* vol. 212, pp. 1-18, 1998.

[10]   U. Beerschwinger, R. L. Reuben, and S. J. Yang, "Frictional study of micromotor bearings," *Sensors And Actuators A-Physical,* vol. 63, pp. 229-241, Dec 1997.

[11]   V. R. Dhuler, M. Mehregany, and S. M. Phillips, "A Comparative-Study Of Bearing Designs And Operational Environments For Harmonic Side-Drive Micromotors," *Ieee Transactions On Electron Devices,* vol. 40, pp. 1985-1989, Nov 1993.

[12]   M. Mehregany, S. D. Senturia, and J. H. Lang, "MEASUREMENT OF WEAR IN POLYSILICON MICROMOTORS," *Ieee Transactions on Electron Devices,* vol. 39, pp. 1136-1143, May 1992.

[13]   M. Mehregany, S. F. Bart, L. S. Tavrow, J. H. Lang, and S. D. Senturia, "Principles In Design And Microfabrication Of Variable-Capacitance Side-Drive Motors," *Journal Of Vacuum Science & Technology A-Vacuum Surfaces And Films,* vol. 8, pp. 3614-3624, Jul-Aug 1990.

[14]   M. Mehregany, S. D. Senturia, and J. H. Lang, "Friction and wear in microfabricated harmonic side-drive motors," in *Solid-State Sensor and Actuator Workshop, 1990. 4th Technical Digest., IEEE*, 1990, pp. 17-22.

[15]   D. Kim, D. Cao, M. D. Bryant, W. J. Meng, and F. F. Ling, "Tribological study of microbearings for MEMS applications," *Journal of Tribology-Transactions of the Asme,* vol. 127, pp. 537-547, Jul 2005.

[16]   M. L. Chan, B. Yoxall, H. Park, Z. Y. Kang, I. Izyumin, J. Chou*, et al.*, "Design and characterization of MEMS micromotor supported on low friction liquid bearing," *Sensors and Actuators a-Physical,* vol. 177, pp. 1-9, Apr 2012.

[17]   B. E. Yoxall, M. L. Chan, R. S. Harake, T. R. Pan, and D. A. Horsley, "Rotary Liquid Droplet Microbearing," *Journal of Microelectromechanical Systems,* vol. 21, pp. 721-729, Jun 2012.

[18]   G. Sun, T. Liu, P. Sen, W. Shen, C. Gudeman, and C.-J. Kim, "Electrostatically Driven Rotor on Conductive Liquid Ring Bearings," in *Solid-State Sensors, Actuators, and Microsystems Workshop*, Hilton Head, South Carolina, 2012, pp. 78-81.

[19]   L. G. Frechette, S. A. Jacobson, K. S. Breuer, F. F. Ehrich, R. Ghodssi, R. Khanna*, et al.*, "High-speed microfabricated silicon turbomachinery and fluid film bearings," *Journal Of Microelectromechanical Systems,* vol. 14, pp. 141-152, Feb 2005.

[20]   V. Badilita, M. Pauls, K. Kratt, and U. Wallrabe, " CONTACTLESS MAGNETIC MICRO-BEARING BASED ON 3D SOLENOIDAL MICRO-COILS FOR ADVANCED POWERMEMS COMPONENTS," in *Proceedings of PowerMEMS 2009*, Washington, DC, USA, 2009, pp. 87-90.

[21]   J. Y. Chen, J. B. Zhou, and G. Meng, "Diamagnetic bearings for MEMS: Performance and stability analysis," *Mechanics Research Communications,* vol. 35, pp. 546-552, Dec 2008.

[22]   J. Y. Chen, J. B. Zhou, G. Meng, and W. M. Zhang, "Evaluation of Eddy-Current Effects on Diamagnetic Bearings for Microsystems," *Ieee Transactions on Industrial Electronics,* vol. 56, pp. 964-972, Apr 2009.

[23]   D. Garmire, H. Choo, R. Kant, S. Govindjee, C. H. Sequin, R. S. Muller*, et al.*, "Diamagnetically Levitated MEMS Accelerometers," in *Solid-State Sensors, Actuators and Microsystems Conference, 2007. TRANSDUCERS 2007. International*, 2007, pp. 1203-1206.

[24]   F. Han, Z. Fu, and J. Dong, "Design and simulation of an active electrostatic bearing for MEMS micromotors," in *4th IEEE International Conference on Nano/Micro Engineered and Molecular Systems*, 2009, pp. 80-85.

[25]   S. Kumar, D. Cho, and W. Carr, "A Proposal For Electrically Levitating Micromotors," *Sensors And Actuators A-Physical,* vol. 24, pp. 141-149, Jul 1990.

[26]   A. Modafe, N. Ghalichechian, A. Frey, J. H. Lang, and R. Ghodssi, "Microball-bearing-supported electrostatic micromachines with polymer dielectric films for electromechanical power conversion," *Journal Of Micromechanics And Microengineering,* vol. 16, pp. S182-S190, Sep 2006.

[27]   M. I. Beyaz, M. McCarthy, N. Ghalichechian, and R. Ghodssi, "Closed-loop control of a long-range micropositioner using integrated photodiode sensors," *Sensors And Actuators A-Physical,* vol. 151, pp. 187-194, Apr 29 2009.

[28]   Y. Naruse, N. Matsubara, K. Mabuchi, M. Izumi, and S. Suzuki, "Electrostatic micro power generation from low-frequency vibration such as human motion," *Journal Of Micromechanics And Microengineering,* vol. 19, Sep 2009.

[29]   D. Dowson and B. Hamrock, "History of Ball Bearings," National Aeronautics and Space Administration TM-81689, 1981.

[30]   O. Reynolds, "On Rolling Friction," *Proceedings of the Royal Academy of Sciences,* vol. VI, 1875.

[31]   H. L. Heathcote, "The Ball Bearing in the Making, Under Test and in Service," *Proceedings of the Institute of Automotive Engineers,* vol. 15, pp. 569-702, 1921.

[32]   D. Tabor, "The Mechanism of Rolling Friction. II. The Elastic Range," *Proceedings of the Royal Society of London. Series A. Mathematical and Physical Sciences,* vol. 229, pp. 198-220, April 21, 1955 1955.

[33]   K. R. Eldredge and D. Tabor, "The Mechanism of Rolling Friction. I. The Plastic Range," *Proceedings of the Royal Society of London. Series A. Mathematical and Physical Sciences,* vol. 229, pp. 181-198, April 21, 1955 1955.

[34]   D. Tabor, "Elastic Work Involved in Rolling a Sphere on Another Surface," *British Journal of Applied Physics,* vol. 6, pp. 79-81, 1955.

[35]   A. Palmgren, *Ball And Roller Bearing Engineering*, 3rd ed. Philadelphia: SKF Industries Inc. , 1954.

[36]   K. Kendall, "Rolling Friction and Adhesion Between Smooth Solids," *Wear,* vol. 33, pp. 351-358, 1975.

[37]   I. Z. Dzhilavdari and N. N. Riznookaya, "An Experimental Assessment of the Components of Rolling Friction of Balls at Small Cyclic Displacements," *Journal of Friction and Wear,* vol. 28, pp. 330-334, 2008.

[38]   L. O. Heim, J. Blum, M. Preuss, and H. J. Butt, "Adhesion and Friction Forces between Spherical Micrometer-Sized Particles," *Physical Review Letters,* vol. 83, pp. 3328-3331, 1999.

[39]   Y. Ando, "Lowering Friction Coefficient under low loads by minimzing the effects of adhesion force and viscous resistance," *Wear,* vol. 254, pp. 965-973, 2003.

[40]   I. Goryacheva and Y. Makhovskaya, "Adhesive Interaction of Elastic Bodies," *Journal of Applied Mathematics anf Mechanics,* vol. 65, pp. 273-282, 2001.

[41]   R. Ghodssi, D. D. Denton, A. A. Seireg, and B. Howland, "Rolling Friction In A Linear Microactuator," *Journal Of Vacuum Science & Technology A-Vacuum Surfaces And Films,* vol. 11, pp. 803-807, Jul-Aug 1993.

[42]   T. W. Lin, A. Modafe, B. Shapiro, and R. Ghodssi, "Characterization of dynamic friction in MEMS-Based microball bearings," *Ieee Transactions On Instrumentation And Measurement,* vol. 53, pp. 839-846, Jun 2004.

[43]   X. B. Tan, A. Modafe, and R. Ghodssi, "Measurement and modeling of dynamic rolling friction in linear microball bearings," *Journal Of Dynamic Systems Measurement And Control-Transactions Of The Asme,* vol. 128, pp. 891-898, Dec 2006.

[44]   W. Weiyuan, W. Yuelin, B. Haifei, X. Bin, and B. Minhang, "Friction and wear properties in MEMS," *Sensors and Actuators A (Physical),* vol. A97-98, pp. 486-491491, 1 April 2002.

[45]   D. Asay, M. Dugger, and S. Kim, "In-situ Vapor-Phase Lubrication of MEMS," *Tribology Letters,* vol. 29, pp. 67-74, 2008.

[46]   B. Hanrahan, M. Beyaz, M. McCarthy, C. Waits, and R. Ghodssi, "A New Performance Regime for Microfabricated Ball Bearings," in *Proceedings of PowerMEMS 2010*, Leuven, Belgium, 2010, pp. 191-194.

[47]   H. Heshmat and S. Jahanmir, "Tribological behavior of ceramics at high sliding speeds in steam," *Tribology Letters,* vol. 17, pp. 359-366, Oct 2004.

[48]   S. Achanta and J. P. Celis, "On the scale dependence of coefficient of friction in unlubricated sliding contacts," *Wear,* vol. 269, pp. 435-442, Jul 2010.

[49]   C. W. Cho and Y. Z. Lee, "Tribological characteristics of oxide layer formed on TiN coated silicon wafer," *Tribology Letters,* vol. 16, pp. 259-263, May 2004.

[50]   I. S. Y. Ku, T. Reddyhoff, A. S. Holmes, and H. A. Spikes, "Wear of silicon surfaces in MEMS," *Wear,* vol. 271, pp. 1050-1058, Jul 2011.

[51]   M. Alberts, K. Kalaitzidou, and S. Melkote, "An investigation of graphite nanoplatelets as lubricant in grinding," *International Journal Of Machine Tools & Manufacture,* vol. 49, pp. 966-970, Oct 2009.

[52]   M. R. Hampson, E. W. Roberts, M. D. Cropper, R. B. Watters, and D. J. Forster, "Towards the effective solid lubrication of ball bearings operating at high temperature," *Proceedings Of The Institution Of Mechanical Engineers Part J-Journal Of Engineering Tribology,* vol. 222, pp. 1041-1049, Dec 2008.

[53]   R. Bandorf, D. M. Paulkowski, K. I. Schiffmann, and R. L. A. Kuster, "Tribological improvement of moving microparts by application of thin films and micropatterning," *Journal of Physics-Condensed Matter,* vol. 20, Sep 2008.

[54] Y. F. Li, D. Trauner, and F. E. Talke, "EFFECT OF HUMIDITY ON STICTION AND FRICTION OF THE HEAD DISK INTERFACE," *Ieee Transactions on Magnetics,* vol. 26, pp. 2487-2489, Sep 1990.

[55] R. Maboudian and R. T. Howe, "Stiction reduction processes for surface micromachines," *Tribology Letters,* vol. 3, pp. 215-221, Sep 1997.

[56] N. Tas, T. Sonnenberg, H. Jansen, R. Legtenberg, and M. Elwenspoek, "Stiction in surface micromachining," *Journal of Micromechanics and Microengineering,* vol. 6, pp. 385-397, Dec 1996.

[57] S. T. Walsh, R. Boylan, and S. F. Bart, "Overcoming stiction in MEMS manufacturing," *Micro,* vol. 13, pp. 49-&, Mar 1995.

[58] B. Bhushan, "Tribology on the macroscale to nanoscale of microelectromechanical system materials: a review," *Proceedings of the Institution of Mechanical Engineers Part J-Journal of Engineering Tribology,* vol. 215, pp. 1-18, 2001 2001.

[59] A. Krauss, O. Auciello, D. Gruen, A. Jayatissa, A. Sumant, J. Tucek*, et al.*, "Ultrananocrystalline diamond thin films for MEMS and moving mechanical assembly devices," *Diamond and Related Materials,* vol. 10, pp. 1952-1961, NOV 2001 2001.

[60] G. Radhakrishnan, P. Adams, R. Robertson, and R. Cole, "Integration of wear-resistant titanium carbide coatings into MEMS fabrication processes," *Tribology Letters,* vol. 8, pp. 133-137, 2000 2000.

[61] N. Kumar, S. Dash, S. Rajagopalan, A. Bahuguna, A. K. Tyagi, and B. Raj, "Tribological properties of SiC coatings deposited by r.f. magnetron sputtering as a function of substrate temperature," *Philosophical Magazine Letters,* vol. 91, pp. 465-472, 2011.

[62]   G. Xie, Q. Wang, L. Si, S. Liu, and G. Li, "Tribological Characterization of Several Silicon-Based Materials Under Ionic-Liquids Lubrication," *Tribology Letters,* vol. 36, pp. 247-257, DEC 2009 2009.

[63]   D. B. Asay and S. H. Kim, "Evolution of the adsorbed water layer structure on silicon oxide at room temperature," *Journal of Physical Chemistry B,* vol. 109, pp. 16760-16763, Sep 2005.

[64]   D. B. Asay, E. Hsiao, and S. H. Kim, "Effects of adsorbate coverage and capillary on nano-asperity friction in atmosphere containing organic vapor," *Journal of Applied Physics,* vol. 110, Sep 2011.

[65]   D. B. Asay and S. H. Kim, "Effects of adsorbed water layer structure on adhesion force of silicon oxide nanoasperity contact in humid ambient," *Journal of Chemical Physics,* vol. 124, May 2006.

[66]   K. Strawhecker, D. B. Asay, J. McKinney, and S. H. Kim, "Reduction of adhesion and friction of silicon oxide surface in the presence of n-propanol vapor in the gas phase," *Tribology Letters,* vol. 19, pp. 17-21, May 2005.

[67]   K. Strawhecker, D. Asay, J. McKinney, and S. Kim, "Reduction of adhesion and friction of silicon oxide surface in the presence of n-propanol vapor in the gas phase," *Tribology Letters,* vol. 19, pp. 17-21, MAY 2005 2005.

[68]   A. L. Barnette, D. B. Asay, D. Kim, B. D. Guyer, H. Lim, M. J. Janik*, et al.*, "Experimental and Density Functional Theory Study of the Tribochemical Wear Behavior of SiO2 in Humid and Alcohol Vapor Environments," *Langmuir,* vol. 25, pp. 13052-13061, 2009.

[69]   I. W. Rangelow, "Critical tasks in high aspect ratio silicon dry etching for microelectromechanical systems," *Journal of Vacuum Science & Technology A,* vol. 21, pp. 1550-1562, Jul-Aug 2003.

[70]   C. M. Waits, B. Morgan, M. Kastantin, and R. Ghodssi, "Microfabrication of 3D silicon MEMS structures using gray-scale lithography and deep reactive ion etching," *Sensors and Actuators a-Physical,* vol. 119, pp. 245-253, Mar 2005.

[71]   B. Morgan, J. McGee, and R. Ghodssi, "Automated two-axes optical fiber alignment using grayscale technology," *Journal of Microelectromechanical Systems,* vol. 16, pp. 102-110, Feb 2007.

[72]   A. Bertsch, H. Lorenz, and P. Renaud, "3D microfabrication by combining microstereolithography and thick resist UV lithography," *Sensors and Actuators a-Physical,* vol. 73, pp. 14-23, Mar 1999.

[73]   S. Bichler, S. Feldbacher, R. Woods, V. Satzinger, V. Schmidt, G. Jakopic*, et al.*, "Functional flexible organic-inorganic hybrid polymer for two photon patterning of optical waveguides," *Optical Materials,* vol. 34, pp. 772-780, Mar 2012.

[74]   J. D. Madden and I. W. Hunter, "Three-dimensional microfabrication by localized electrochemical deposition," *Journal of Microelectromechanical Systems,* vol. 5, pp. 24-32, Mar 1996.

[75]   A. A. Tseng, "Recent developments in micromilling using focused ion beam technology," *Journal of Micromechanics and Microengineering,* vol. 14, pp. R15-R34, Apr 2004.

[76] H. Robbins and B. Schwartz, "CHEMICAL ETCHING OF SILICON .2. THE SYSTEM HF, HNO3, H2O, AND HC2H3O2," *Journal of the Electrochemical Society,* vol. 107, pp. 108-111, 1960.

[77] B. Schwartz and H. Robbins, "CHEMICAL ETCHING OF SILICON .4. ETCHING TECHNOLOGY," *Journal of the Electrochemical Society,* vol. 123, pp. 1903-1909, 1976.

[78] G. Marcos, A. Rhallabi, and P. Ranson, "Monte Carlo simulation method for etching of deep trenches in Si by a SF6/O-2 plasma mixture," *Journal of Vacuum Science & Technology A,* vol. 21, pp. 87-95, Jan-Feb 2003.

[79] S. Azimi, A. Sandoughsaz, B. Amirsolaimani, J. Naghsh-Nilchi, and S. Mohajerzadeh, "Three-dimensional etching of silicon substrates using a modified deep reactive ion etching technique," *Journal of Micromechanics and Microengineering,* vol. 21, Jul 2011.

[80] K. Gantz, L. Renaghan, and M. Agah, "Development of a comprehensive model for RIE-lag-based three-dimensional microchannel fabrication," *Journal of Micromechanics and Microengineering,* vol. 18, Feb 2008.

[81] K. P. Larsen, J. T. Ravnkilde, and O. Hansen, "Investigations of the isotropic etch of an ICP source for silicon microlens mold fabrication," *Journal of Micromechanics and Microengineering,* vol. 15, pp. 873-882, Apr 2005.

[82] L. Yin, S. J. Meschter, and T. J. Singler, "Wetting in the Au-Sn system," *Acta Materialia,* vol. 52, pp. 2873-2888, Jun 2004.

[83] V. Chawla, R. Jayaganthan, and R. Chandra, "Structural characterizations of magnetron sputtered nanocrystalline TiN thin films," *Materials Characterization,* vol. 59, p. 1015, 2008.

[84] H. Hertz, "On the Contact of Rigid Elastic Solids," *Gesammelte Weke,* vol. 1, 1895.

[85] K. L. Johnson, K. Kendall, and A. D. Roberts, "SURFACE ENERGY AND CONTACT OF ELASTIC SOLIDS," *Proceedings of the Royal Society of London Series a-Mathematical and Physical Sciences,* vol. 324, pp. 301-&, 1971.

[86] Y. P. Zhao, L. S. Wang, and T. X. Yu, "Mechanics of adhesion in MEMS - a review," *Journal of Adhesion Science and Technology,* vol. 17, pp. 519-546, 2003.

[87] R. S. Bradley, "The Cohesive Force between Solid Surfaces and the Surface Energy of Solids," *Philosophical Magazine,* vol. 13, 1932.

[88] D. Tabor, "SURFACE FORCES AND SURFACE INTERACTIONS," *Journal of Colloid and Interface Science,* vol. 58, pp. 2-13, 1977.

[89] B. V. Derjaguin, V. M. Muller, and Y. P. Toporov, "EFFECT OF CONTACT DEFORMATIONS ON THE ADHESION OF PARTICLES," *Progress in Surface Science,* vol. 45, pp. 131-143, Jan-Apr 1994.

[90] D. Maugis, "ADHESION OF SPHERES - THE JKR-DMT TRANSITION USING A DUGDALE MODEL," *Journal of Colloid and Interface Science,* vol. 150, pp. 243-269, Apr 1992.

[91] K. L. Johnson, "Mechanics of Adhesion," *Tribology International,* vol. 31, pp. 413-418, 1999.

[92] D. Liu, J. Martin, and N. Burnham, "Which Fractal Parameter Contributes Most to Adhesion?," *Journal of Adhesion Science and Technology,* vol. 24, pp. 2383-2396, 2010 2010.

[93] B. Hanrahan, J. Feldman, M. McCarthy, C. Waits, and R. Ghodssi, "Microball Bearing Tribology Part I: Friction," *Journal of Micromechanics and Microengineering,* vol. *to be submitted*, p.

, 2012.

[94] Y. S. Muzychka, J. R. Culham, and M. M. Yaovanovich, "Thermal Spreading Resistance in Compound and Orthotropic Systems," *Journal of Thermophysics and Heat Transfer,* vol. 18, pp. 45-51, 2004.

[95] F. Incropera, D. DeWitt, T. Bergman, and A. Lavine, *Fundamentals of Heat and Mass Transfer*, 6th ed. USA: John Wiley and Sons, 2006.

[96] M. McCarthy, B. Hanrahan, C. Zorman, and R. Ghodssi, "Rolling Friction in MEMS Ball Bearings: The Effects of Loading and Solid Film Lubrication," in *STLE/ASME International Joint Tribology Conference*, San Diego, CA, USA, 2007.

[97] B. Hanrahan, M. McCarthy, J. Balsam, C. M. Waits, H. Bruck, and R. Ghodssi, "An Investigation of Hard Film Coatings for High-Speed Rotary PowerMEMS supported in Microball Bearings," in *Proceedings of PowerMEMS 2009*, Washington, DC, USA, 2009, pp. 589-592.

[98] C. Livermore, A. R. Forte, T. Lyszczarz, S. D. Umans, A. A. Ayon, and J. H. Lang, "A high-power MEMS electric induction motor," *Journal Of Microelectromechanical Systems,* vol. 13, pp. 465-471, Jun 2004.

[99] T. Juliano, V. Domnich, and Y. Gogotsi, "Examining pressure-induced phase transformations in silicon by spherical indentation and Raman spectroscopy: A statistical study," *Journal Of Materials Research,* vol. 19, pp. 3099-3108, Oct 2004.

[100] F. Demangeot, P. Puech, V. Paillard, V. Domnich, and Y. G. Gogotsi, "Spatial distribution of strain and phases in Si nano-indentation analysed by Raman mapping," in *Gettering And Defect Engineering In Semiconductor Technology*. vol. 82-84, ed Zurich-Uetikon: Trans Tech Publications Ltd, 2002, pp. 777-782.

[101] V. Domnich, Y. Gogotsi, and S. Dub, "Effect of phase transformations on the shape of the unloading curve in the nanoindentation of silicon," *Applied Physics Letters,* vol. 76, pp. 2214-2216, Apr 17 2000.

[102] D. M. Follstaedt, J. A. Knapp, and S. M. Myers, "Mechanical properties of ion-implanted amorphous silicon," *Journal Of Materials Research,* vol. 19, pp. 338-346, Jan 2004.

[103] J. G. Swadener and M. Nastasi, "Increasing the fracture toughness of silicon by ion implantation," *Nuclear Instruments & Methods In Physics Research Section B-Beam Interactions With Materials And Atoms,* vol. 206, pp. 937-940, May 2003.

[104] M. S. Gaither, F. W. DelRio, R. S. Gates, E. R. Fuller, and R. F. Cook, "Strength distribution of single-crystal silicon theta-like specimens," *Scripta Materialia,* vol. 63, pp. 422-425, Aug 2010.

[105] S. Bhowmick, J. J. Melendez-Martinez, and B. R. Lawn, "Contact fatigue of silicon," *Journal of Materials Research,* vol. 23, pp. 1175-1184, Apr 2008.

[106] R. L. Brown and S. E. Stein. (Feb. 2). *NIST Chemistry WebBook*.

[107] Mbeychok. (2007, Feb. 1, 2012). *Vapor Pressure Chart (3rd ed.)*.

[108] I. Langmuir, "THE CONSTITUTION AND FUNDAMENTAL PROPERTIES OF SOLIDS AND LIQUIDS. PART I. SOLIDS," *Journal of the American Chemical Society,* vol. 38, pp. 2221-2295, 1916/11/01 1916.

[109] R. Gomez. (2007, Feb. 1, 2012). *adsorption isotherms (1st ed.).*

[110] D. B. Asay and S. Kim, "Evolution of the adsorbed water layer structure on silicon dioxide at room temperature," *Journal of Physical Chemistry B,* vol. 109, pp. 16760-16763, 2005.

[111] D. B. Asay and S. Kim, "effect of adsorbed water layer structure on adhesion force of silicon dioxide nanoasperity contact in humid ambient," *Journal of Chemical Physics,* vol. 124, pp. 174712-5, 2006.

[112] R. Jones, H. M. Pollock, J. Cleaver, and C. Hodges, "Adhesion forces between glass and silicon surfaces in air studied by AFM: Effects of Relative Humidity, particle size, roughness, and Surface Treatment," *Langmuir,* vol. 18, pp. 8045-8055, 2002.

[113] T. Thundat, X. Zheng, G. Y. Chen, and R. J. Warmack, "Role of humidity in atomic force microscopy imaging," *Surface Science Letters,* vol. 294, pp. 939-943, 1993.

[114] M. Beyaz, B. Hanrahan, J. Feldman, and R. Ghodssi, "An Integrated Micro-Turbo-Generator Supported on Encapsulated Microball Bearings," in *International Conference on MicroElectroMechanical Systems*, Paris, France, 2012, pp. 1209-1212.

[115] R. Ghodssi, B. Hanrahan, and M. Beyaz, "Microball Bearing Technology for MEMS Devices and Integrated Microsystems," in *16th International Conference on Solid-State Sensors, Actuators, and MIcrosystems (Transducers 2011)*, Beijing, China, 2011, pp. 1789-1794.

[116] R. Knizikevicius, "Simulations of Si and SiO(2) Etching in SF(6)+O(2) Plasma," *Acta Physica Polonica A,* vol. 117, pp. 478-483, Mar 2010.

[117] K. P. Larsen, D. H. Petersen, and O. Hansen, "Study of the roughness in a photoresist masked, isotropic, SF6-based ICP silicon etch," *Journal of the Electrochemical Society,* vol. 153, pp. G1051-G1058, 2006.

[118]   H. Chen, "Inductively Coupled Plasma Etching of InP," Masters of Science, Metallurgy and Materials Science, University of Toronto, Toronto, 2000.

[119]   T. Hill, "Analysis of DRIE Uniformity for Microelectromechanical Systems," Masters of Science, Electrical and Computer Science, Massachusetts Institute of Technology, Cambridge, 2004.

[120]   T. Murakoshi, Y. Endo, K. Fukatsu, S. Nakamura, and M. Esashi, "Electrostatically Levitated Ring-Shaped Rotational-Gyro/Accelerometer," *Japanese Journal of Applied Physics,* vol. 42, pp. 2468-2472 2003.

[121]   R. Hergert, B. Hanrahan, H. A., and R. Ghodssi, "Silicon Retainer Ring Integration in Micro-turbine with Thrust Ball Bearing Support Mechanism," in *Transducers 2011*, 2011.